DYNAMICS AND MELTING OF A HETEROGENEOUS MANTLE: IMPORTANCE TO GEOGRAPHIC VARIATIONS IN HOTSPOT LAVA COMPOSITION

A DISSERTATION SUBMITTED TO THE GRADUATE DIVISION OF THE UNIVERSITY OF HAWAI‘I IN PARTIAL FULFILLMENT OF THE REQUIREMENTS FOR THE DEGREE OF

DOCTOR OF PHILOSOPHY

IN

GEOLOGY AND GEOPHYSICS

AUGUST 2009

By
Todd Anthony Bianco

Dissertation Committee:

Garrett T. Apuzen-Ito, Chairperson
Janet M. Becker
Michael O. Garcia
John J. Mahoney
Carlos Coimbra

We certify that we have read this dissertation and that, in our opinion, it is satisfactory in scope and quality as a dissertation for the degree of Doctor of Philosophy in Geology and Geophysics.

DISSERTATION COMMITTEE

_____
Chairperson

_____

_____

_____

_____

Acknowledgments

I would like to thank my advisor Prof. Garrett Ito for his support and guidance throughout my PhD and MS. I also would like to thank my committee members, Prof. Janet Becker, Prof. Michael Garcia, Prof. John Mahoney, and Prof. Carlos Coimbra for their effort. This work is also supported by collaboration with two other coauthors, Dr. Jeroen van Hunen and Maxim Ballmer. Financial support was provided by NSF-CSEDI grant # 0440365, and the Maui High Performance Computing Center's Student Engagement Grant. Special thanks to the Toby Lee Family, the Pullman Family and the ARCS Foundation, Manoa Chapter for their tremendous support. Thanks are rightfully due to the University of Hawaii, SOEST, and the Department of Geology and Geophysics. And, to my friends, who have always been there for me.

This work is dedicated to my family; it is a rather humble tribute compared to the dedication, love, and support, they have given me.

Abstract

Geochemical variations in hotspot lava compositions commonly reveal geographical and temporal trends over hundreds of kilometers and millions of years. These trends provide clues regarding the character of mantle heterogeneity and the dynamics feeding hotspot magmatism. This work examines an alternative end-member scenario of mantle structure in the plume hypothesis, in which heterogeneity exists in the form of small veins uniformly distributed throughout the mantle matrix. A numerical model couples equations of 3D mantle convection and melting in order to simulate realistic mantle processes. Mantle components with relatively enriched incompatible-element compositions are assumed to be more fusible than relatively depleted components. Melting is assumed to be fractional, and magma pools at the surface assuming it mixes perfectly. Resulting geographic trends at the surface are described. The overall conclusion of the study is that large-scale (10^2 km) geographic variations arise from the dynamics of plume-lithosphere interaction. The pattern of compositional trends at the surface is controlled by the thickness of the lithosphere, the reference viscosity of the mantle, and the difference between the depths at which components begin melting. These physical parameters control the compositional pattern because they influence the size, position, extent of melting, and melting rate of the different mantle components. In simulations of intraplate hotspots, the average composition of magma erupted at a volcano changes as it grows such that the influence of less refractory components is greatest in the early stages of volcanism, and the influence of more refractory components increases with time. These predictions are compared to observed variations

in Nd and Pb isotope ratios at Hawaii, and observations of Pb isotope ratios at Samoa, and Réunion. In simulations of plumes rising beneath a mid-ocean ridge, the contribution from a less refractory component tends to increase near the center of the hotspot. In this case, model predictions are compared to observations of Sr isotopes and La/Sm ratios at Iceland and the surrounding Mid-Atlantic Ridge. It is concluded that strong compositional variation between the source of plumes and the shallower mantle is not needed to explain some of the compositional trends observed at intraplate and ridge-centered hotspots.

Table of Contents

List of Tables

List of Figures

Chapter 2

Chapter 3

Chapter 4

List of Symbols

Symbol	Meaning (Defining Eq.)	Units
B	Thermal buoyancy flux	Mg/s
c_p	Specific heat capacity	J/(mol K)
C_I	Concentration of incompatible element in liquid (3.12)	-
C_0	Concentration of incompatible element in initial solid	-
D	Bulk distribution coefficient	-
DC	Depleted peridotite component	
Di	Dissipation number	-
E	Enrichment factor of incompatible element (3.11)	-
E_a	Activation energy	J/mol
EC	Enriched peridotite component	
F	Total melt fraction	%
F_e	Equilibrium melt fraction (3.7)	%
f_m	Fractional contribution of component m (3.15)	-
h_c	Thickness of crust at ridge (4.10)	km
$HSDP$	Hawaii Scientific Drilling Project	
I	Isotope ratio of pooled magma; EC Fraction (3.13)	-
I^i	Isotope ratio of component i	-
I_R	Isotope ratio of magma at ridge (4.9)	-
ΔI_R	Magnitude of anomaly at ridge-centered hotspot	-
I_V	Isotope ratio of pooled magma in a volcano (3.14)	-
$\hat{\mathbf{k}}$	Vertical unit vector	-
$\dot{M}$	Melting rate (3.10)	%/Ma
MAR	Mid-Atlantic Ridge	
$MORB$	Mid-ocean ridge basalt	
OIB	Ocean island basalt	
P	Pressure	Pa
PC	Pyroxenite component	
Q	Heat (3.4)	J
R	Gas constant	J/(mol K)
Ra	Rayleigh number	-
r	Exponent of water-dependent term in rheology (4.3)	-
r_{plume}	Radial measure of thermal anomaly	km
$r_{volcano}$	Radius of volcano source cylinder	km
ΔS	Liquid-solid entropy change	J/(K)
T	Absolute temperature	K
T'	Temperature above solidus (3.8)	K
T_{liq}	Liquidus temperature	K
t_{plate}	Half-space cooling age at x = 0	Ma
T_{plume}	Maximum thermal anomaly	K
T_r	Reference temperature	K

T_{sol}	Solidus temperature	K
u	Velocity	km/Ma
u_{plate}	Plate velocity	km/Ma
w	Vertical velocity	km/Ma
x	Model length; "Position along volcanic chain axis"	km
X_w	Weight fraction of water in peridotite	ppm
y	Model width; "Position perpendicular to chain"	km
Δy_{min}	Short-wavelength, high-EC-fraction anomaly at ridge-centered hotspot	km
Δy_{norm}	Long-wavelength, low-EC-fraction anomaly at ridge-centered hotpot	km
z	Model depth	km
z_{max}	Maximum model depth	km
α	Proportionality constant for dehydration (4.3)	Pa s
γ	Adiabatic gradient (3.6)	K/Pa
η	Dynamic viscosity	Pa s
η_o	Reference viscosity	Pa s
θ	Azimuth	radians
μ	Water-dependent viscosity (4.3)	Pa s
μ_{eff}	Effective two-component viscosity (4.4)	Pa s
$\mu'_{\mathbf{eff}}$	Dimensionless, effective viscosity (4.7a)	-
μ_{lim}	Maximum increase factor by dehydration (4.7b)	-
φ	Mass fraction of component	-

Chapter 1

Introduction

"Volcanic hotspots", or "hotspots", are locations on the surface of the earth where an anomalously high volume of magma erupts. Hotspots are not explained by the simplest form of the theory of plate tectonics. The theory of plate tectonics predicts that volcanism should occur at plate boundaries, with the oceanic crust being formed at divergent plate boundaries known as mid-ocean ridges. Plate tectonic theory asserts that new seafloor crust forms as plates spread; the mantle beneath wells-up so that mantle material rises below its melting pressure, creating magma that percolates to the surface [e.g., *Hess*, 1962; *Vine and Matthews*, 1963; *Vine and Wilson*, 1965]. On a worldwide scale, the thickness of the oceanic crust is relatively constant (~6-7 km on average) [e.g., *White et al.*, 1992; *Dick et al.*, 2003] owing to the relatively uniform motion of plates along large sections of the mid-ocean ridge system. At hotspots, however, the thickness of the crust increases by many kilometers over distances of tens of kilometers.

For example, on the Mid-Atlantic Ridge, the thickness of crust at Iceland and the adjacent Kolbeinsey and Reykjanes ridges ranges between 10 km and 40 km [*Hooft et al.*, 2006]. Also, the island and seamount chains of Hawaii-Emperor, Samoa, Louisville, Canaries, and Réunion, among others, form on seafloor far from any plate boundary. Given the success of plate tectonic theory and its wide-reaching implications, strong motivation exists for geoscientists to reconcile the existence of hotspots within the framework of plate tectonics.

By far and away the most popular explanation for the cause of hotspots is the mantle plume hypothesis [*Wilson*, 1963; *Morgan*, 1971; 1972]. The hypothesis proposes that thermal instabilities form at a boundary layer in the earth's mantle, typically assumed to be near the core-mantle boundary. These instabilities rise buoyantly through the mantle until reaching the lithosphere. The excess temperature in the plume causes material to intersect its solidus at a greater depth in the mantle than ambient mantle does. Beneath mid-ocean ridges, the deeper melting and actively rising plume material results in anomalously thick crust, such as that observed at Iceland (up to 40 km thick). If the excess temperature in the plume is hot enough, material may begin melting at depths much greater than the base of thick (>100 km), old (>100 Ma) lithosphere, such as that beneath Hawaii, Samoa and other ocean islands.

The compositions of lavas erupted at hotspots provide clues regarding the dynamics and composition of the source of hotspot magmatism [e.g., *Allègre*, 1982; *Zindler and Hart*, 1986; *Hofmann*, 1997]. Researchers have noted that with increasing proximity to the center of hotspot volcanism, incompatible-element composition indicates greater contribution from a source with long-term enrichment of the most incompatible elements. In the context of the plume hypothesis, geoscientists have explained that these observations result from melting a heterogeneous mantle in which the source of the most active center of hotspot volcanism samples the most enriched mantle. For example, at Iceland, $^{87}Sr/^{86}Sr$, La/Sm, and $^{206}Pb/^{204}Pb$ values increase along the Reykjanes and Kolbeinsey ridges toward Iceland [e.g., *Hart et al.*, 1973; *Schilling*, 1973, *Sun et al.*, 1975]. Based on these observations, scientists have further hypothesized that enriched mantle plume material feeds Icelandic volcanism, and is diluted along the ridge by

mixing with melts from the relatively depleted source of mid-ocean ridge volcanism. At Hawaii, the most voluminous stage of volcanism, the shield-stage, is associated with lower $^{143}Nd/^{144}Nd$ and higher $^{87}Sr/^{86}Sr$, $^{206}Pb/^{204}Pb$, and $^{206}Pb/^{204}Pb$ relative to the post-shield stage [e.g., *Kurz et al.*, 1987; 1996; *Lassiter et al.*, 1996; *DePaolo et al.*, 2001; *Bryce et al.*, 2005]. A common explanation for this observation is that the shield stage occurs over an enriched plume center, and the post-shield stage occurs over the edge of the plume where depleted upper mantle has been entrained during upwelling. The inferred difference between the deep mantle source of plumes and the ambient upper mantle implies large-scale compositional layering in the mantle. However, both geophysical and geochemical evidence exists that imply the entire mantle mixes. For example, tomographic studies have concluded that some slabs subduct into the lower mantle [*e.g.*, *van der Hilst et al.*, 1997; *Fukao et al.*, 2001] resulting in mass transfer between the upper an lower mantle. In addition, geodynamic simulations have predicted that layered convection is unstable [e.g., *van Keken and Ballentine*, 1998], and geochemical studies provide evidence for a component with depleted isotope compositions that is common to hotspots and ridges worldwide [*Hart et al.*, 1992; *Hanan and Graham*, 1996].

The goal of this dissertation is to test an end-member of the form of heterogeneity in a mantle with plumes: it is assumed that mantle heterogeneity exists in uniform and ubiquitous veins, rather than in large, layered reservoirs. The veins of mantle components have different incompatible element compositions and begin melting at different depths and temperatures. Extending the work of *Ito and Mahoney* [2005a, b; 2006] that showed how mantle dynamics affect magma composition, the present study proposes that because

mantle dynamics vary with position, the relative contribution of mantle source components to pooled magma at the surface will vary. Thus, large-scale geographic trends in lava composition may be the consequence of variable upper mantle dynamics, rather than large-scale compositional layering. 3D geodynamic models of thermally buoyant plumes interacting with and melting beneath the lithosphere are used to predict the length scale and magnitude of geographic variations in magma composition erupting at the surface. Chapter 2 introduces some fundamental aspects of the method, presents a reference model of a plume with two solid components rising beneath lithosphere far from a ridge, and compares predictions of the reference model to observations at Hawaii. Chapter 3 details the method used in this research more extensively, and examines a range of simulated conditions to illustrate how the composition of intraplate hotspots may depend on physical conditions in the mantle, such as plate thickness, viscosity, and water content. Comparisons of predictions to observations at Hawaii, Samoa and Réunion, as well as introducing simulations with three compositional components in the mantle are made in Chapter 3. Chapter 4 discusses a study of plumes rising beneath a mid-ocean ridge, and tests of a wide range of simulations to illustrate the dependence of along-ridge composition on physical conditions in the mantle. Predictions are compared to observations of composition and crustal thickness along the Mid-Atlantic Ridge near Iceland in Chapter 4. Chapter 5 summarizes the conclusions of this dissertation.

Chapter 2

Geochemical variation at the Hawaiian hotspot caused by upper mantle dynamics and melting of a heterogeneous plume

Abstract

Geochemical variations within the young Hawaiian Islands occur in two particularly prominent forms: differences between volcanic stages and differences between the "Loa" and "Kea" sub-chains. These observations have been interpreted to reveal spatial patterns of compositional variation in the mantle, such as concentric zoning about the hotspot or elongate streaks along the hotspot track. Numerical models of a hot plume of upwelling mantle that is interacting with, and melting beneath, a moving lithospheric plate suggest that some of the above interpretations should be re-evaluated. The mantle plume is assumed to be uniformly isotopically heterogeneous, thus without any compositional zoning. Nonetheless, the present models predict geographic zoning in lava isotope composition, an outcome that is caused by differences in melting depths of distinct source components and plume-lithosphere interaction. Isotope compositions of model volcanoes that grow as they pass over the melting zone can explain some of the gross aspects of isotope variation at Hawaii. The results illustrate that chemical zoning at the surface is not necessarily a map of zoning in the mantle, and this affects further inferences about the chemical structure of the mantle.

2.1 Introduction: Geochemical Variations at Hotspots

Temporal and geographic variations in lava geochemistry are observed at prominent hotspots in a variety of tectonic settings, such as Hawaii [e.g., Tatsumoto, 1978; *Frey and*

Rhodes, 1993; *Lassiter et al.*, 1996; *DePaolo et al.*, 2001; *Regelous et al.*, 2003; *Bryce et al.*, 2005], the Galápagos, [*Geist et al.*, 1988; *Graham et al.*, 1993; *White et al.*, 1993; *Harpp and White*, 2001], and Iceland [*Schilling*, 1973; *Schilling et al.*, 1999; *Breddam et al.*, 2000; *Kokfelt et al.*, 2006]. Previous authors have attributed such geographic trends directly to geographic variations in composition of the solid mantle, which are often thought to be associated with mantle plumes rising through various forms of a chemical layered mantle [e.g., *Hofmann*, 1997].

At Hawaii, for example, isotope data collected from the most voluminous, shield stage of volcanism indicate that this phase is fed by a source characterized by long-term enrichment in highly incompatible elements, whereas later stages of volcanism show evidence for less enrichment in the source [e.g., *Kurz et al.*, 1987; 1996; *Lassiter et al.*, 1996; *DePaolo et al.*, 2001; *Bryce et al.*, 2005]. One hypothesis to explain the compositional difference between the two stages is with a concentrically zoned mantle plume, with an enriched, shield source in the center, and a depleted, post-shield source at the periphery [*Frey and Rhodes*, 1993; *Lassiter et al.*, 1996; *Bryce et al.*, 2005]. Concentric zoning may be caused by a rising mantle plume with a center that is composed of material from the deepest mantle, and a surrounding sheath that is largely entrained material from the shallower mantle [e.g., *Kurz and Kammer*, 1991; *Frey and Rhodes*, 1993; *Hauri et al.*, 1994; *Lassiter et al.*, 1996].

Isotope data sets also reveal prominent geographical variations within the Hawaiian Islands, the most prominent of which is seen as isotopic distinctions between the sub-parallel (Mauna) “Loa” volcanic chain (southern line) and (Mauna) “Kea” chain

(northern line). Isotope compositions indicate that the line of volcanoes that make up the Loa chain sample a source that has greater long-term enrichment of incompatible elements compared to the source sampled by volcanoes that make up the Kea chain [e.g., *Frey and Rhodes*, 1993; *Kurz et al.*, 1996; *Abouchami et al.*, 2005; *Bryce et al.*, 2005]. The concentrically zoned plume concept may explain these observations if the two sub-chains pass over the plume at different distances from the center [*Lassiter et al.*, 1996; *Bryce et al.*, 2005]. Another explanation of the Loa-Kea difference is that the plume has a northeast-southwest asymmetry in composition [*Abouchami et al.*, 2005]. Both the concentric zoning and lateral asymmetry models suggest the plume draws material from deeper-mantle chemical heterogeneities of length scales equal to or larger than that of upwelling itself.

The above interpretations are straightforward, but in order to connect magma composition to the source one must understand the process of magma genesis, which can be complex, particularly in the presence of source heterogeneity [e.g., *Sobolev et al.*, 2007; *Phipps Morgan* 2001]. Previous authors have proposed that buoyancy-driven upwelling can contribute to the relatively incompatible-element-enriched geochemical signature of hotspot lavas compared to normal mid-ocean ridge basalts [*Kurz and Geist*, 1999; *Breddam et al.*, 2000, *Schilling et al.*, 1999]**.** Other studies that model melting of small-scale heterogeneities show that erupted magma composition can be influenced strongly by the upwelling pattern in a melting zone [*Bianco et al.*, 2005; *Ito and Mahoney*, 2005a; 2005b; 2006]. We thus anticipate that the complex upper mantle dynamics expected for a mantle plume can lead to surface compositions with geographic patterns that can deviate from any inherent pattern within the mantle source.

This paper examines the 3D flow and melting of a two-component mantle plume interacting with a moving plate. The source material is non-zoned, but is heterogeneous at spatial scales much smaller than the melting zone. This work quantifies the spatial (and temporal) variation of the isotope ratios of magmas that may erupt at the surface, and compares these predictions to observations at Hawaii.

2.2 Method: 3D Dynamics and Non-zoned Mantle

To model the 3D mantle flow, heat transfer, and melting of the upper mantle, we use the finite element code Citcom [*Moresi and Gurnis*, 1996; *Zhong et al.*, 2000]. The model space spans 1600 km by 800 km horizontally with 6.25 km grid resolution, and is 400 km deep with 5 km resolution (Figure 2.1a). The extended Boussinesq approximation includes latent heat due to melting and adiabatic heating, but not viscous dissipation. Viscosity is determined by a temperature-dependent Newtonian rheology exactly as described by *Zhong and Watts* (2002) with the exception that the reference viscosity is 5×10^{19} Pa s at the ambient mantle (potential) temperature of 1300°C. The initial temperature condition is the solution of a half-space that has cooled for 100 Ma plus an adiabatic gradient. The bottom boundary temperature condition matches the initial condition plus a circular Gaussian anomaly with a peak excess temperature of 290°C (and decreases by a factor of *e* at a radius of 50 km) to form the plume [*Zhong and Watts*, 2002]. The top of the model space is fixed at 25°C. Maximum vertical velocity in the model is ~190 cm/yr and the resulting thermal buoyancy flux is 12 Mg/s, which is higher than, but comparable to, other estimates of the Hawaiian anomaly

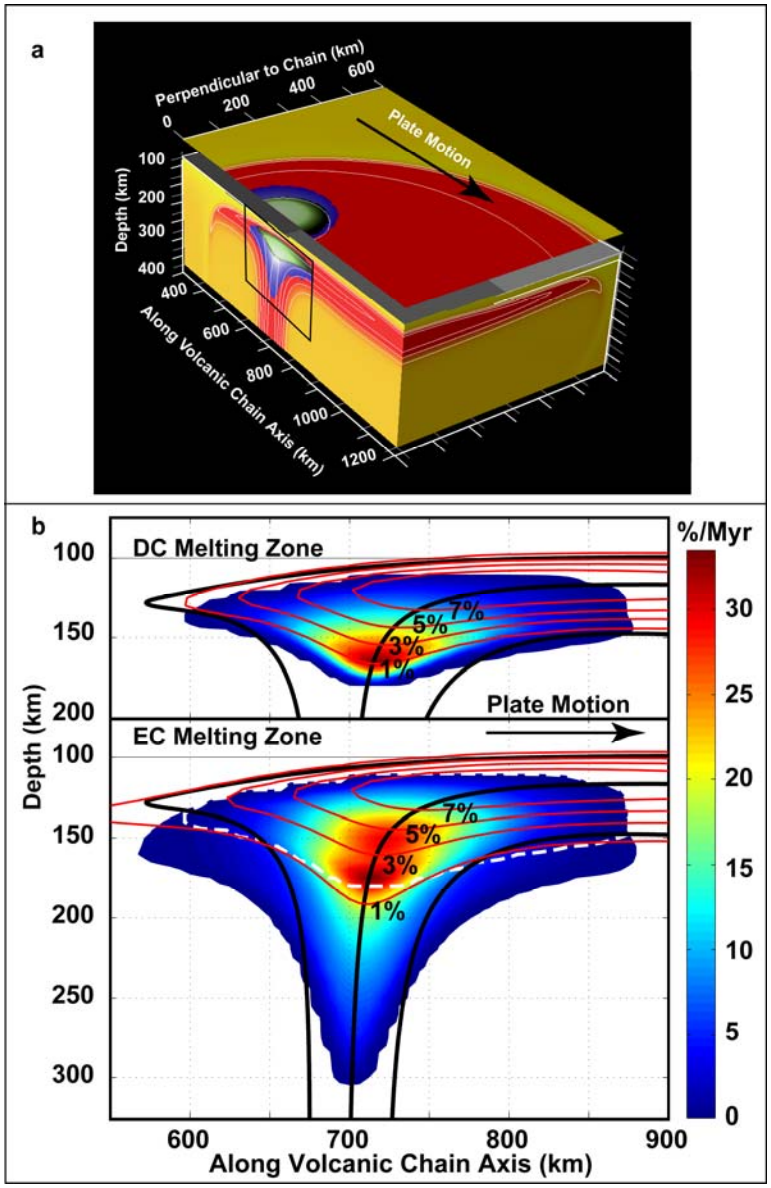

Figure 2.1 Intraplate Model. (a) Slices through the model domain show projections of the 3D potential temperature field in shades of yellow (cool) and red (warm); the full model domain is 1600 km long "along the volcanic chain axis" (*x*-dimension), 800 km wide "perpendicular to chain" (*y*-dimension), and 400 km deep (*z*-dimension), and has resolution of 6.25 km in the horizontal plane, and 3.125 km in depth. White contours mark the 1350°C, 1450°C and 1550°C isotherms. Horizontal plane is at a depth of 150 km but plotted above its actual depth for visibility. Black arrow indicates the direction of plate motion. A matrix of a more refractory, depleted component (DC) is assumed to contain small-scale blobs or veins of a more fusible, enriched component (EC). EC and DC melting zones are filled with blue and green, respectively. The black box outlines area plotted in Figure 2.1b. (b) Melting rate is colored on a vertical slice through the center of the plume. The EC and DC melting zones are shown in separate boxes for visibility, but they overlap as conveyed by the white, dashed outline of the DC melting zone on the bottom panel. Fraction of partial melting for each component is shown as red contours. Thick black lines are streamlines of mantle flow.

[*e.g., Sleep*, 1990; *Ribe and Christensen* 1999]. Finally, a horizontal velocity boundary condition (~9 km/Ma) is imposed on the top of the model space to simulate plate motion, the vertical wall containing the plume center is a reflecting boundary, and all other boundaries are open to flow with zero conductive heat flow [*Ribe and Christensen*, 1999].

To model melting, we calculate the extent of melting on the same Eulerian (fixed) mesh used to calculate temperature and pressure using parameterized solidi [*Katz et al.*, 2003]. A passive tracer advection scheme is used to track the total extent of partial melting (F) of all solid material in the mantle. Melting rate is the difference between F calculated at a node and the F advected to the node during a time step, divided by the time step duration, where refreezing is prohibited ($dF/dt \geq 0$) [*see Ribe and Christensen*, 1999, *Eqs. 2-3*]. The total extent of partial melting also controls the water content (and trace-element composition) of both the solid and melt. We adapt the model of *Katz et al.* [2003] to simulate near fractional melting by assuming equilibrium occurs between the solid and melt generated at each time step, and that the advected solid composition as a function of F is that for fractional melting.

In the case presented here, two components are randomly distributed throughout the mantle: 10% enriched peridotite ("EC") and 90% depleted peridotite ("DC"). EC is enriched in incompatible trace elements, and has lower normalized $^{143}Nd/^{144}Nd$, (ε_{Nd} = -3.3) compared to DC (9.8). Also, DC is anhydrous while EC has a water content of 400 ppm, which (using other parameters identical to that in *Katz et al.* [2003]) lowers the EC solidus by 121°C relative to DC. Thus, the partial melting zones of DC and EC overlap,

but melting of EC begins deeper, is wider, and continues to higher maximum extents (Figure 2.1b). We assume the components equilibrate thermally with each other, but remain chemically separate [e.g., *Phipps Morgan* 2001]. To predict magma composition, we assume magma (from both components) rises vertically to the surface and mixes (or pools) in direct proportion to the rate generated in the mantle. The composition of magma that has risen to the to the seafloor (Figure 2.2) is thus

$$\varepsilon_{Nd}(x,y) = \frac{\sum_{l=1}^{2}\sum_{n=1}^{N} \varepsilon_{Nd}^{l} \varphi^{l} C_{o}^{l} E_{n}^{l} \left(\partial F_{n}^{l} / \partial t\right)}{\sum_{l=1}^{2}\sum_{n=1}^{N} \varphi^{l} C_{o}^{l} E_{n}^{l} \left(\partial F_{n}^{l} / \partial t\right)} \tag{2.1}$$

where the finite element mesh is uniform, l is the component (EC or DC), n is the depth position of a finite element grid point, N is the number of vertical grid points, ε_{Nd}^{l}, ϕ^{l}, C_{o}^{l} are the ε_{Nd} composition, the starting mantle mass fraction, and the initial Nd concentration of a lithology, respectively. The function E_{n}^{l} is the factor enrichment of the Nd in the magma, relative to the starting solid (C_{o}^{l}) as given by the fractional melting equation and $\partial F_{n}^{l} / \partial t$ is the melting rate at a grid point. The assumptions made in Equation 1 are most valid if real mantle melting is fractional [*Johnson et al.*, 1990; *Langmuir et al.*, 1992; *McKenzie*, 2000; *Rubin et al.*, 2005], or if any potential liquid-solid interactions do not affect the relative melt generation rates in the mantle. Indeed there is evidence that mantle melt transport is rapid and/or fractional.

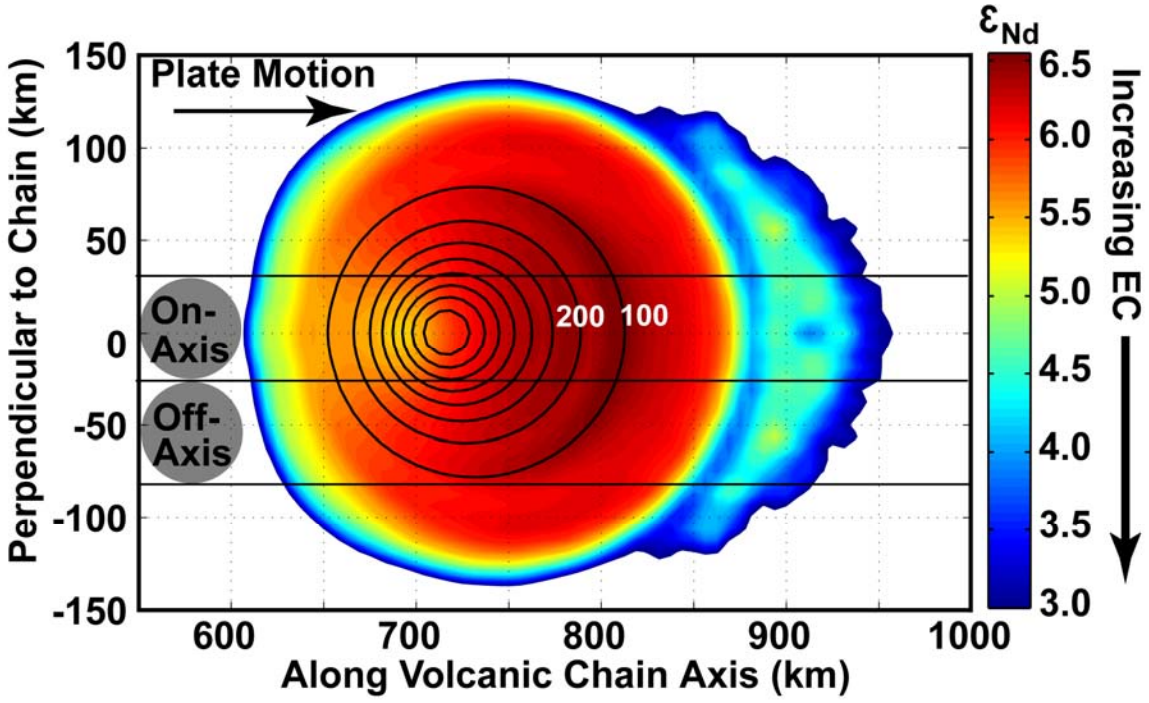

Figure 2.2 Geographic trends in composition. Seafloor Composition and Eruption Rate. Map view of model Nd isotope composition (colored as ε_{Nd}) assuming EC and DC melts rise vertically and mix perfectly at the surface (see Eq. 1). Low ε_{Nd} (blue) is associated with EC and high ε_{Nd} (red) is associated with DC. Black contour lines are eruption rates in km^3/Ma (where 100 and 200 km^3/Ma are labeled) and the center of these contours is the center of the hotspot. Gray circles are the area from which volcanoes will sample magma, and horizontal lines show the paths that two volcanoes take as they move with the plate.

2.3 Results: Predicted Geochemical Trends

The prediction (Figure 2.2) is that melting a uniformly heterogeneous mantle plume can result in compositional zoning at the surface. At the very edges of the melting zone, EC is the only material melting and thus expressed at the surface. Over a broad area within these outer edges, compositions have higher ε_{Nd}, which is where DC melting is productive. Near to where the magma flux is greatest (at an along-chain distance of x = 675-700 km), a local minimum in ε_{Nd} (local maximum in EC) occurs. This minimum reflects efficient EC melting near the center of the plume stem where the EC melting zone extends deepest beneath the DC melt zone, and where active upwelling is fastest

within the EC melting zone. Overall, the magmatic geochemical pattern resembles a form of radial zoning with an EC-like center surrounded by a broad zone with stronger DC-type compositions and a thin EC-rich rim.

In addition, the pattern is considerably asymmetric in the direction of plate motion, with more EC-like compositions upstream of plate motion than downstream. This is caused by shearing of the rising plume by plate motion. Shearing offsets the most productive central portion of the DC melting zone slightly downstream from that of the EC zone. The tilting of the center streamline in Figure 2.1b gives a sense of this effect. Also, shearing causes both melting zones to extend less far upstream of the center streamline than downstream, but this effect is greater for the DC melting zone because it is shallower. The net result is a higher flux of melts from EC than from DC on the upstream side than farther downstream as reflected in the surface pattern in Figure 2.2. Increasing lithospheric thickness and plate speed tends to increase the asymmetry of the pattern, increasing Rayleigh number tends to decrease the asymmetry.

We now predict the composition of volcanoes formed by passage of the plate over the model mantle and compare these predictions to specific datasets collected at Hawaii. Here we assume that the circular area over which a volcano samples magma has a constant radius (25 km) as it moves with the plate over the hotspot (see Figure 2.2). An extensive dataset on the evolution of a single volcano from the mid-shield stage to later stages comes from the Hawaii Scientific Drilling Project (HSDP). Figure 2.3 shows both predicted and observed ε_{Nd} versus the percent of the total volcano thickness. Thickness in models has been computed by assuming that the magma feeding the volcano builds an

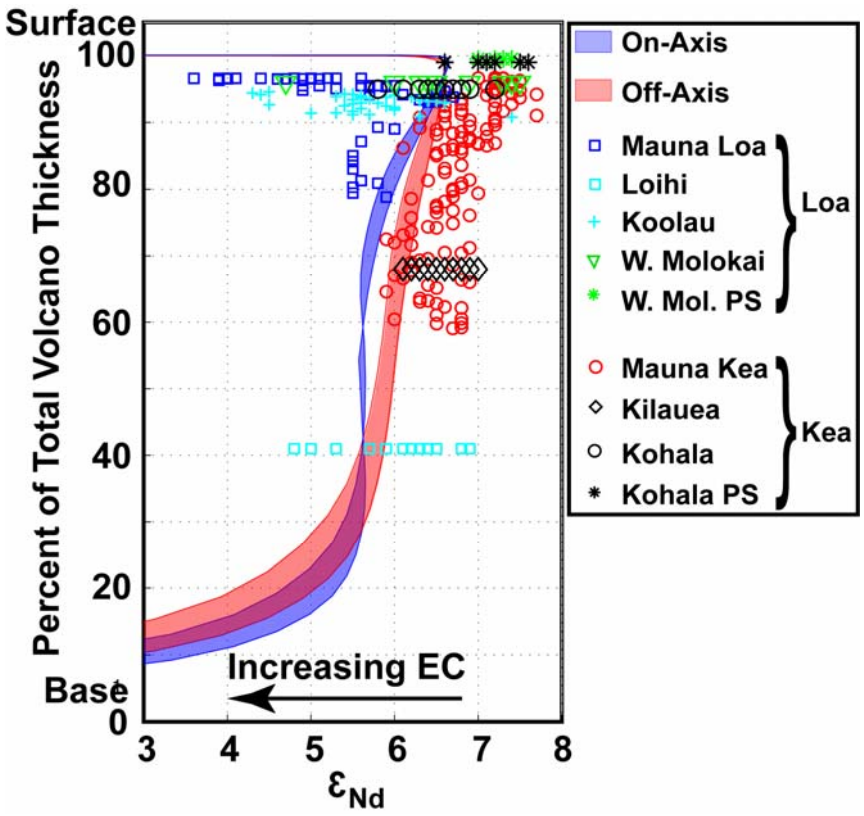

Figure 2.3 Predicted and observed composition of Hawaiian volcanoes. Composition versus Thickness. Shaded regions show the range of predicted average ε_{Nd} composition of an on- (blue) and off-axis (red) volcano (see Figure 2), for cone-shaped volcanoes that encompass a range of slopes near those of Hawaiian shields [*DePaolo and Stolper*, 1996]. The vertical axis is percent of maximum thickness, such that zero is the base of a volcano and 100% is the surface of a fully grown volcano (i.e., for a 10 km thick, extinct volcano, 20% represents surface 2 km above the base). Colored shapes are data for Mauna Loa (blue squares), Loihi (cyan squares), Koolau (cyan crosses), West Molokai (green triangles), West Molokai post-shield (green stars), Mauna Kea (red circles), Kilauea (black diamonds), Kohala (black circles), and Kohala post-shield (black stars) [see GEOROC database http://georoc.mpch-mainz.gwdg.de and references therein; Koolau data from *Salters et al.*, 2006]. To plot Mauna Kea and Mauna Loa data on this vertical axis, we normalized the sample depths (or heights for some cases) to 7.5 km and Koolau data is normalized to 6.5 km, the approximate thickness of the volcanoes at the sample locations [see *Wessel*, 1993; *Kurz et al.*, 1995; *Haskins and Garcia*, 2004; *Garcia et al.*, 2007]. Kilauea and Loihi are plotted on the diagram based on the assumption that they erupted 25% and 5% of their final volumes, respectively, consistent with their estimated ages and volumes compared to the duration of most Hawaiian volcanoes [*Lipman et al.*, 2006; *Robinson and Eakins*, 2006]. Therefore, data collected at the current surface of Kilauea plot at the same thickness as data collected deep in a Mauna Kea drill core. Estimated volumes, ages, or depths are not available for West Molokai or Kohala, so we assumed these samples occurred at volume percentages that typify the end of the corresponding stages: 95% for shield data and 99% for post-shield data.

axisymmetric, cone-shaped volcano [*DePaolo and Stolper*, 1996] so that we can most easily compare it to HSDP data. Using fractional thickness allows us compare predictions and compositions at approximately the same stage of volcanism for different locations with different absolute thicknesses.

Figure 2.3 shows that as the model volcano grows, composition indeed shifts from EC-like to DC-like. The very base of a volcano forms while it is sampling the upstream edge of the melting zone, where virtually only EC is melting and where ε_{Nd} is low. Between the 10-20% range of a volcano's final thickness, ε_{Nd} rapidly rises, which signals the onset of appreciable DC melting. Above ~30% of the total thickness, compositions shift more gradually toward higher ε_{Nd}. This portion of the volcano is being built as the volcano begins to pass into the higher ε_{Nd} (orange-red in Figure 2.2) portion of the melting zone, while still sampling low ε_{Nd} (yellow) magma. The simple volcano growth model [*DePaolo and Stolper*, 1996] predicts volcano thickness to accumulate nonlinearly with volcano volume. This nonlinearity plus the changing eruption rates along the volcano's path cause the transition from moderate (yellow) to intermediate (red) ε_{Nd} over a considerable part of the shallowest portion of the volcano, which is likely sampled by HSDP. The very last lavas to erupt reveal the low ε_{Nd} compositions predicted at the very downstream edge of the melting zone. Finally, Figure 2.3 also illustrates that a volcano passing 50 km off-axis is predicted to have higher ε_{Nd} values than an on-axis volcano throughout most of the volcano's growth. The explanation is that the on-axis volcano passes directly over the local ε_{Nd} minimum near the plume center whereas the off-axis volcano passes largely to the side of this EC-rich melting zone (Figure 2.2).

The predictions capture some important observed trends at Hawaii. The predicted shift from moderate to high ε_{Nd} for as a function of age for both on- and off-axis model volcanoes follows the prominent trends observed in data from the Mauna Kea section of the HSDP and the combined series of Kilauea-, to Kohala shield-, to Kohala post-shield; the same is true for much of the combined series of the Mauna Loa- (except for the shallowest samples) and Koolau, to West Molokai shield-, to West Molokai post-shield. However, while samples from a Koolau drill core [*Salters et al.*, 2006] overlap with Mauna Loa data, some late shield eruptions on Koolau extend to much lower ε_{Nd} [*Roden et al.*, 1994] (not shown in Figure 2.3), which the model does not predict. Also, the compositional distinction between the shield stages of Loa and Kea sub-chain volcanoes is captured by the sustained ε_{Nd} difference between the on- and off-axis model volcanoes, which is a concept proposed by other workers [e.g., *Lassiter et al.*, 1996, *Bryce et al.*, 2005]. Then, after ~95% of the total crust has erupted, this compositional distinction is predicted to end because of the concentric like compositional pattern (see Figure 2.2). This prediction may explain why post-shield data from West Molokai (on the Loa sub-chain) overlaps with post-shield data from Mauna Kea and Kohala (on the Kea sub-chain). However, late-shield and post-shield data from other Loa sub-chain volcanoes (e.g., Hualalai, Kahoolawe and Koolau) do preserve a distinction from Kea-like compositions. Finally, compositions of different volcanoes along the Kea sub-chain overlap each other at the same interpolated thicknesses (e.g. Kilauea erupts the same ε_{Nd} composition as deep Mauna Kea lavas). This overlap indicates that the volcanoes erupted the same ε_{Nd} composition when they occupied the same position over the hotspot, and this is captured in the present (and others', e.g., *Abouchami et al.* [2005]; *Bryce et al.*,

[2005]) steady-state model(s). The present model compositions do overlap with Loihi data, but the high ε_{Nd} lavas are not predicted; nor is the range of ε_{Nd} at Loihi predicted.

2.4 Discussion

The model presented above predicts large-scale, persistent, geographic variations in isotope composition at Hawaii that are similar to observed trends. However, some potentially important aspects are not included in this initial model. One large simplification is the assumption of a mantle with only two components (EC and DC), whereas it is widely recognized that three or more components are required to fully explain Hawaii data [e.g., *Kurz and Kammer*, 1991; *Eisele et al.*, 2003, *Abouchami et al.*, 2005].

Pb-isotope data provide a good constraint on the number of components and style of heterogeneity in the mantle, and successful models should address these data. Recent high-precision Pb-isotope data show that compositions of the Kea and Loa sub-chains form statistically different populations in $^{208}Pb/^{204}Pb$ vs. $^{206}Pb/^{204}Pb$ space [*Abouchami et al.*, 2005]. These authors interpreted the results as indicating that the two sub-chains sample mutually exclusive, bilateral mantle sources, requiring at least four components beneath Hawaii (two for each sub-chain). However, the Pb isotope mixing arrays from individual volcanoes do cross with those from the other sub-chain, which suggests the sources of the sub-chains are, in fact, not mutually exclusive (*Xu et al.*, 2007). It may therefore be possible for non-zoned, heterogeneous mantle to explain these data, but with an added third component. Previous calculations showed that a large range of Pb-isotope data can be explained by melting two source types plus varying amounts of a third type

[*Ito and Mahoney*, 2005a; 2005b]. It is possible that a third component is being under-sampled by one Hawaiian sub-chain and more heavily expressed in the other due to differences in the proximity to the center of the plume track much like the behavior of the current two-component models.

A third component may also help address the discrepancy that the low ε_{Nd} values predicted during the early growth of both on- and off-axis volcanoes fall on the low end of the range measured at Loihi. A suitable component may have, relative to global values, intermediate $^{87}Sr/^{86}Sr$, ε_{Nd} and high $^{3}He/^{4}He$ [*Kurz et al.*, 1996], much like the proposed "C" [*Hanan and Graham*, 1996] or "FOZO" [*Hart et al.*, 1992] components. Because the model predicts the earliest lava composition to be dominated by the deepest-melting component, a small amount of a deep-melting, C-like component (with $\varepsilon_{Nd} \approx 6$) might improve the match to the Loihi ε_{Nd} values. It might also explain the high $^{3}He/^{4}He$ values for Loihi (as high as 32 times atmospheric $^{3}He/^{4}He$), which provide another line of evidence for more than two components.

Regardless of the consideration of additional components, the model predictions are symmetric across the plume axis. Thus to explain differences between the Loa and Kea sub-chains, we, like others before [e.g., *Lassiter et al.*, 1996; *Bryce et al.*, 2005] must assume the axis between the sub-chains are shifted to the north of the center of the plume.

Another weakness of the present dynamic models deals with the well-known evolution of major element composition from the tholeiitic lavas erupted during the shield phase to the more alkalic lavas erupted during the post-shield phase. This

tholeiitic-alkalic transition probably represents a change from higher to lower extents of partial melting [e.g., *MacDonald*; 1964, *Frey et al.*, 1990]. We predict the pooled mean extent of partial melting sampled by a volcano as

$$\overline{F} = \frac{\sum_{l=1}^{2}\sum_{n=1}^{N} F_n^l \varphi^l \left(\partial F_n^l / dt\right)}{\sum_{l=1}^{2}\sum_{n=1}^{N} \varphi^l \left(\partial F_n^l / dt\right)} \tag{2.2}$$

for a uniform mesh, where F is the extent of partial melting and in this case n is the position of a grid point and is summed over N nodes inside a cylindrical capture volume beneath the volcano (see Figure 2.2). Figure 2.4 shows that predicted mean extent of partial melting, $\overline{F}$ increases (or remains high) with distance along the plume track until >99% of the total melt volume is produced. This prediction is inconsistent with the observation of alkalic post-shield lavas in the last ~2.5% of the total erupted volume [*Frey et al.*, 1990] as well as with the general association of post-shield alkalic lavas and "depleted" (e.g., high-ε_{Nd}) isotope compositions [e.g., *Chen and Frey*, 1985; *Frey et al.*, 1990; *Kennedy at al.*, 1991; *Feigenson et al.*, 2003].

The model prediction of late-stage high $\overline{F}$ is caused by the solid residue near the center of the hotspot being swept with plate motion and continuing to melt to higher fractions on the downstream end of the melting zone. It is a result that is not predicted in parameterized models of concentric melting zones that do not consider plate shear [e.g., *Lassiter et al., 1996*; *Bryce et al.*, 2005]. This behavior is independent the isotope calculations, or whether two or even a single source component is present, and we have not seen a dynamical model of a plume beneath a moving plate that adequately predicts

such low $\bar{F}$ in the appropriate location on the downstream end of the melting zone. This result presents a new challenge for all dynamical models of plume-plate interaction to explain.

The most robust finding of this study, regardless of its specific application to Hawaii, is that the coupling of upper mantle dynamics and melting of small-scale mantle heterogeneities can lead to larger scale geographic compositional variations at the surface. The broader implication is that if any compositional zoning is present in a plume at spatial scales comparable to the scales of the plume itself —such as that caused by a plume entraining ambient mantle as it rises through a layered mantle—then the zoning could be less substantial or quite different than previously inferred for Hawaii or other hotspots. Consideration of the upper mantle dynamics as done here is therefore essential for inferring the composition of the mantle from which plumes originate and through which they rise. The present model also predicts that if plumes contain streaks or blobs of heterogeneity [e.g., *Farnetani et al.*, 2002; *Eisele et al.*, 2003; *Abouchami et al.*, 2005; *Farnetani and Samuel*, 2005; *Marske et al.*, 2007], the sampling of such heterogeneity will not be constant over the life of a volcano, even if the mass fraction of heterogeneity entering the melting zone is constant. A logical step for future work is to include the dynamic effects illustrated in this study with different forms of zoning in the source, to see if they can better explain the data than the current model.

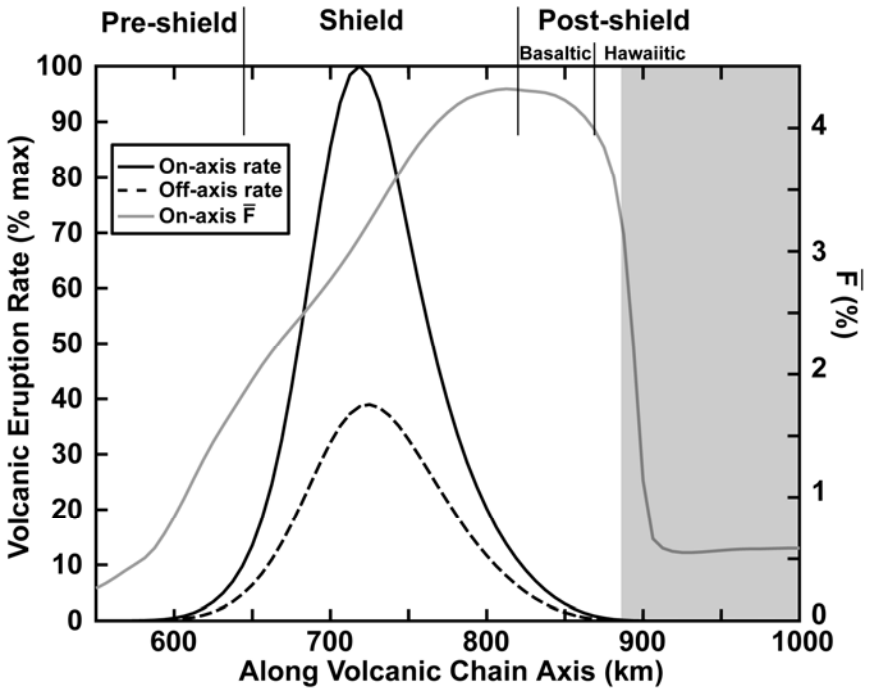

Figure 2.4 Mean *F* and eruption rate. Eruption Rate and $\overline{F}$. Heavy black lines mark eruption rates for an on-plume-axis volcano (solid) and an off-axis volcano (dashed), normalized to the maximum rate of the on-axis volcano, ~36×10^6 m^3/yr. Rates are the sum of melting rates in vertical cylindrical capture areas passing over the hotspot (see Figure 2). The solid gray line is mean extent of melting $\overline{F}$ (see Eq. 2) for an on-axis volcano. Vertical black lines indicate the approximate volume fractions (applicable to both on- and off-axis volcanoes) that delineate the pre- and post-shield stages of Mauna Kea [see *Frey et al.*, 1990 and references therein]. Post-shield, alkalic stages began at Mauna Kea when volume rates fell to 10% of the maximum, and these stages account for ~2.5% of the total erupted magma. In contrast, a (>1%) decrease of $\overline{F}$ in the model (gray box), which we use as a qualitative proxy for the onset of alkalic magma production, occurs when volume fluxes and total volume fall well below 1% of the maxima. This inconsistency occurs regardless of whether we melt a one- (not shown) or two-component (gray curve) mantle; it is a new issue that needs to be addressed by any dynamic model of plume-plate interaction. In this model peak eruption rate is ~36×10^6 m^3/yr on-axis and 14×10^6 m^3/yr off-axis, and total erupted volume is ~4.0×10^4 km^3 on-axis and 1.7×10^4 km^3 off-axis. The prediction that on-axis volcanoes erupt more than double the peak rate and total volume of off-axis volcanoes is consistent with estimates that Mauna Loa is nearly double the volume of Mauna Kea, but inconsistent with small differences in erupted volumes estimated at other Loa and Kea sub-chain volcanoes [*DePaolo and Stolper*, 1996; *Robinson and Eakins*, 2006].

2.5 Conclusions

Upper mantle dynamics and melting of a heterogeneous source can lead to strong geographical variations in the isotope composition of magmas erupted at the surface,

independent of any geographical variation in mantle source. Our model of an intraplate plume predicts Nd-isotope compositions that change from the center to the end of the melting zone in the same sense as that recorded by the shield to post-shield progression of Hawaiian volcanoes. If volcanoes pass at different distances from the hotspot center, the present model also predicts compositions that are consistent with the sustained differences between Loa (on-axis) and Kea (off-axis) sub-chains. These results offer an alternative explanation for these well-established observations at Hawaii. Finally, these results motivate re-evaluations of the amplitude or even presence of compositional zoning in plumes and the mantle through which plumes rise beneath Hawaii and other hotspots.

Chapter 3

Geochemical variations at intraplate hotspots caused by variable melting of a veined mantle plume

Abstract

A 3D geodynamic model of plume-lithosphere interaction is used to explore the causes of spatial patterns of magmatic compositions at intraplate hotspots. This study focuses on the coupling between upper mantle flow, heat transfer, and melting of a heterogeneous (veined) plume in which multiple components have different solidi and isotope composition, and exist with a uniform mass fraction throughout the model space. The Cartesian finite-element code CITCOM is used to simulate mantle convection with the extended Boussinesq approximation in a volume of upper mantle 400 km in thickness. Parameterized melting models are used to simulate melting of peridotite components with different water contents and a pyroxenite component. Predicted volcano composition evolves from having a strong signature from the deepest-melting component in the early stages of volcanism to a strong signature from the shallowest-melting component in the later stages. This compositional trend is caused by shear flow in the asthenosphere associated with plate motion, which tilts the rising plume and horizontally displaces the center of each components' melting zones. The total change in volcano composition increases with increasing plate age, decreasing Rayleigh number, and decreasing vertical distance between the bases of the components' melting zones. Another important result is that when three or more components simultaneously contribute to the pooled magma composition, the predicted composition of a volcano

does not trend between the actual components' compositions, but rather between mixtures of them. Thus, inferring mantle composition from data may be difficult in the presence many small-scale heterogeneities. The evolution of the average composition of Mauna Kea volcano is attributed to melting of a veined mantle and plume-lithosphere dynamics, and scatter about the average is attributed to small-scale variability in the source. The model predicts mixing lines in Pb isotope space that are linear, but shifted in $^{208}Pb/^{204}Pb$ for a given $^{206}Pb/^{204}Pb$, which is a key distinction between the Loa and Kea subchain compositions. This prediction requires that the relative mass of components vary in the mantle, and is an alternative to the hypothesis that the compositions of components vary in the mantle.

3.1 Geochemical Variation at Hotspots

Studies of the temporal and geographic variations in hotspot geochemistry have been used to infer the length scale and distribution of chemical heterogeneity in the mantle. Previous work has commonly focused on explaining variations in hotspot composition by attributing them directly to parallel variations in the solid mantle composition. At Hawaii, for example, lavas of the shield stage erupt with isotope compositions that suggest a source that has long-term incompatible-element enrichment compared to lavas of the post-shield stage [e.g., *Kurz et al.*, 1987; 1995; 1996; *Lassiter et al.*, 1996; *Abouchami et al.*, 2000; Eisele et al., 2003; *Bryce et al.*, 2005]. One explanation involves concentric zoning of an ascending mantle plume, in which the "enriched" source of shield volcanism rises near the center of the rising mantle plume, and the more "depleted" source of post-shield volcanism rises at the periphery of the plume [*Frey and Rhodes*, 1993; *Lassiter et al.*, 1996; *Bryce et al.*, 2005]. Such zoning may be attributed to a

mantle plume being fed by a deep, "enriched" mantle reservoir, and while rising, entraining relatively "depleted" upper mantle rock at its edges [e.g., *Kurz and Kammer*, 1991; *Frey and Rhodes*, 1993; *Hauri et al.*, 1994; *Lassiter et al.*, 1996]. Another explanation is that the plume contains streaks of material with different compositions that are inherent to the source reservoir, and that the relative amount or composition of the streaks change in time, thus causing variations in lava composition [e.g., *Abouchami et al.*, 2005; *Farnetani and Hofmann*, 2009].

Another class of explanations involves no such zoning in composition, but instead proposes that mantle heterogeneity is uniform at moderate length scales (~10^1-10^3 km), but that different components are sampled differently at these scales by partial melting depending on the temperatures, pressures, and rates that they melt [*Phipps-Morgan*, 2001; *Ito and Mahoney*, 2005a,b]. Subsequently, the thermal structure of the plume, rather than the chemical structure, controls lava composition, in that more refractory components, though existing throughout the plume, are only melted near the hot center [e.g., *Ren et al.*, 2005]. However, in addition, the rate of melting also is proportional to the rate that the mantle is upwelling and decompressing, which is another aspect likely to vary strongly within mantle plumes [*Ito and Mahoney*, 2005a]. Thus fully 3D dynamical models are needed to assess the importance of such aspects of mantle plumes, especially how they are influenced by plume-plate interaction.

Work in Chapter 2 examined the composition of volcanoes sampling melts from a (two-component) veined mantle plume rising beneath a thick lithosphere (100 Ma) with a large Rayleigh number (2.6 x 10^6). Model volcano composition was predicted to evolve

from that of the deepest-melting component to a composition more influenced by the shallower-melting component. Models also predicted that volcanoespassing over the plume center are more influenced from the deepest-melting component than volcanoes passing off-axis from the center (i.e., offset perpendicular to plate motion). The first prediction was shown to explain the observation at Hawaii that the isotopic composition of shield stage volcanism is consistent with a source with greater long-term enrichment in incompatible elements than that of the post-shield stage [e.g., *Kurz et al.*, 1987; 1995; 1996; *Lassiter et al.*, 1996; *Abouchami et al.*, 2000; Eisele et al., 2003; *Bryce et al.*, 2005]. The second prediction addressed some of the differences between (Mauna) Kea and (Mauna) Loa subchains [e.g., *Abouchami et al.*, 2005] with the assumption that Kea volcanoes are off-axis from the plume center. Chapter 2 only examined a limited set of fluid dynamic conditions, and therefore did not characterize the relationship between the dynamics and composition; nor did it examine situations that would apply to settings other than Hawaii. Also, the earlier model did not address Pb isotope systematics at Hawaii, as the observed compositions can only be explained with three or more components [e.g., *Abouchami et al.*, 2005].

In this work, we systematically examine how the dynamics of plume-plate interaction under a range of conditions controls the lateral variations in magma composition at intraplate hotspots. We simulate upper mantle flow, heat transfer, and melting in 3D, and predict the composition of pooled magma erupting at volcanoes that grow as they pass over model hotspots. To reveal the essential dynamical influences and simulate a range of geological conditions, we examine models with different plate ages and reference viscosities. We also examine the effects of different water content of the most fusible

component, which affect the difference in depth that this component begins melting relative to more refractory components. Some simulations include a deep-melting component with a high melt productivity to capture the possible effect of pyroxenite melting in the plume. Finally, we apply the model to settings other than Hawaii, and expand the model from a previous two-component reference model [*see Chapter 2*] to a three-component model and compare these predictions to observations at Hawaii. The three-component model addresses the complicated Pb isotope trends observed at Mauna Kea.

3.2 Methods

3.2.1 Mantle Convection

To simulate 3D upper mantle convection, we employ CITCOM, a Cartesian coordinate, finite element code that numerically solves the equations of conservation of mass, momentum and energy for an incompressible, infinite-Prandtl-number fluid [*Moresi and Gurnis*, 1996; *Zhong et al.*, 2000; *van Hunen et al.*, 2005]. Making the extended Boussinesq approximation, the dimensionless continuity and momentum equations reduce to

$$\nabla \cdot \mathbf{u} = 0 \tag{3.1}$$

$$-\nabla P + \nabla \cdot \left[\eta\left(\nabla \mathbf{u} + \nabla^T \mathbf{u}\right)\right] + RaT\hat{\mathbf{k}} = 0 \tag{3.2}$$

where $\boldsymbol{u}$ is the velocity vector, P is pressure, η is dynamic viscosity, Ra is Rayleigh number, T is absolute temperature, $\hat{\boldsymbol{k}}$ is vertical unit vector, and all variables and operators are non-dimensional (see Table 3.1 for a list of constants, variables, and assumed values). The dimensionless energy equation is

$$\frac{DT}{Dt} = \nabla^2 T - \mathrm{Q}\left(\mathbf{u}, \dot{M}\right) \tag{3.3}$$

where D/Dt is the full material time derivative, and $\dot{M}$ is the melting rate. The source term Q accounts for cooling due to the latent heat of melting and adiabatic decompression. For simplicity, viscous dissipation is omitted, which is likely to be of the same order of magnitude as the former terms, but trial tests of the simulation show it does not greatly affect predictions. In non-dimensional form Q is

$$Q = Di \cdot T\left[w - \left(\frac{\Delta S}{Di \cdot c_p} \right) \frac{DF}{Dt} \right] \tag{3.4}$$

where Di is dissipation number, w is vertical velocity, ΔS is the change in entropy associated with the liquid-solid phase change, c_p is specific heat, and F is melt fraction. Viscosity, η, is determined by a temperature-dependent Newtonian rheology described by [*Zhong and Watts,* 2002]

$$\eta = \eta_o \, exp\left[\frac{E_a}{R} \left(\frac{1}{T} - \frac{1}{T_r} \right) \right] \tag{3.5}$$

where η_o is reference viscosity, E_a is activation energy, R is the gas constant, and T_r is reference temperature. In this work, η_o ranges from ~4.1×10^{19} to 1.7×10^{20} Pa s and is controlled by specifying Ra, with the other quantities that compose Ra imposed (i.e., considered to be fixed).

Model geometry and an example calculation of the temperature field after 6000 time steps is shown in Figure 2.1a. The initial temperature condition is set using the half-

space cooling model [*Davis and Lister*, 1974] with top of the model space (i.e. zero depth) fixed at 0°C plus an adiabatic gradient, γ, defined as

$$\gamma = exp\left(Di \cdot \mathbf{z}\right) - 1 \tag{3.6}$$

where z is non-dimensional depth, increasing downward. The bottom boundary temperature condition (i.e., at z_{max}) matches the initial condition plus, to form a buoyant plume, a circular anomaly with excess temperature that is maximum at the center (T_{plume} = 290 K) and decreases exponentially with radial distance by a factor of e at a given reference radius, r_{plume}. The center of the temperature anomaly is located at x = 700 km from the inflow boundary in the direction of plate motion (i.e., x = 0, where plate age is the youngest). Plate motion is simulated with a horizontal velocity boundary condition (~9 km/Ma) imposed on the top of the model space; the vertical wall slicing through the plume center (y = 0) is a reflecting boundary, and all other boundaries are open to flow with zero conductive heat flow [*Ribe and Christensen*, 1999].

3.2.2 Melting

To simulate partial melting in the mantle, we employ parameterizations of peridotite [*Katz et al.,* 2003] and pyroxenite [*Pertermann and Hirschmann.,* 2003] melting. The parameterizations describe the equilibrium fraction of partial melting, F_e, at a given pressure and temperature such that F_e can be expressed as a function of dimensionless temperature, T', as

$$F_e = F_e\left(T'\right) \tag{3.7}$$

$$T' = \frac{T - T_{sol}}{T_{liq} - T_{sol}} \tag{3.8}$$

where T_{sol} and T_{liq} are the solidus and liquidus temperature functions of a given mantle material, respectively. T_{sol} and T_{liq} capture the essential effects of petrologic differences between different components as discussed below.

We combine the convection and melting equations in a manner similar to that of *Ribe and Christensen* [1999] to obtain

$$\frac{DF}{Dt} = \dot{M}\left(T, P, \mathbf{u}, X_w\right) \tag{3.9}$$

$$\dot{M} = \max\left(0, \frac{DF_e}{Dt}\right). \tag{3.10}$$

Here F is the total melt fraction of the material, which can differ from F_e because F_e is calculated using the local conditions to solve (3.8), whereas F is the advected melt fraction. If, in contrast, the model simulated batch melting and allowed for freezing of liquid, then F would equal F_e and the distinction between the two variables would be unnecessary. The variable $\dot{M}$ is the local melting rate and X_w is the water content of peridotite components only. A passive tracer advection scheme solves (3.9) and (3.10). In a given time step, tracers first advect F to new positions. Next, (3.7) and (3.8) are solved at the finite element nodes, and the nodal F_e are interpolated to the tracers in their new positions. Finally, DF_e/Dt is calculated as the difference between F of the tracers from the last time step and the new, interpolated F_e, divided by the elapsed model time. $\dot{M}$ is non-zero inside the melting zone, and because freezing is not allowed, it is zero outside of the melting zone.

In the most complete description of (3.8), T_{sol} and T_{liq} are functions of pressure, P, and the complete mineralogical composition of the mantle material. In this work, water

content, X_w, is the only compositional variable considered for peridotite. The effect of water is known to lower the solidus of peridotite, thus tending to increase F_e relative to anhydrous peridotite at the same T and P. The effect of water is greatest at the base of the melting zone where F is low [e.g., *Hirth and Kohlstedt*, 1996 *Hirschmann et al.*, 1999; *Asimow et al., 2004*]. For hydrous peridotite (i.e., $X_w > 0$), F_e is calculated assuming equilibrium between the solid and infinitesimal liquid produced in (3.7) [see Eq. (19) in *Katz et al.,* 2003]. At the end of a time step, we assume fractional melting to calculate X_w of the residue. Also, the parameterization of peridotite includes the effects of exhausting clinopyroxene to reduce the rate at which F_e changes with pressure. Finally, in some of the models below, we include a pyroxenite component using the parameterization of (3.7) of *Pertermann and Hirschmann* [2003].

Figure 2.1b shows the melting rates in melting zones for an anhydrous ("DC") and hydrous ("EC", X_w = 400 ppm in this case) peridotite for the same model as in Figure 2.1a. Note that the EC melting zone extends deeper, is wider, and as a whole produces more liquid than the DC melting zone. Contours indicating greater than ~2% of partial melting are nearly the same in shape between EC and DC because at these fractions of melting, EC solid residue is largely dehydrated. The lowest extent of partial melting (~0-2%) of EC occurs below the entire DC melting zone, and is where incompatible elements are extracted into the melt. This simulated difference between the melting zones of components is the essential reason that these models predict variations in how components are expressed in magma composition.

3.2.3 Geochemistry

This work examines the geochemistry of magma that erupts at a hotspot due to the melting of a heterogeneous mantle plume. The heterogeneity in the model mantle is uniformly distributed, and can be envisioned as a mixture of blobs or veins spanning length scales orders of magnitude smaller than that of the plume or the melting zone. To model this type of heterogeneity, we assume that the components compose a specified mass fraction of the mantle uniformly throughout the model space. The components are in thermal equilibrium, but do not chemically react. As discussed in *Chapter 2*, the latter assumption is valid if melting is fractional [e.g., *Johnson et al.*, 1990; *Langmuir et al.*, 1992; *McKenzie*, 2000; *Rubin et al.*, 2005], or if any potential liquid-solid interactions between different components do not substantially alter the rates at which the different components melt, in a relative sense, compared to the rates at which they would melt by decompression in chemical isolation.

The geochemical model assumes that the content of incompatible trace-elements in the infinitesimal melts that are generated at a given point in the model is governed by modal fractional melting. The enrichment E of the incompatible element in the melt relative to the source is

$$E = \frac{C_l}{C_0} = \frac{1}{D}\left(1 - F\right)^{1/D-1}. \tag{3.11}$$

Here C_l is the concentration of the element in the liquid, C_0 is the initial concentration in the solid, and D is the bulk partition coefficient. Melting rate controls the amount of

magma formed with enrichment factor calculated by (3.11). We assume magma rises vertically and predict the composition of pooled melts from all components with

$$C_l = \frac{\sum_{l=1}^{N} \varphi^l C_0^l \int_z E^l \left(\partial F^l / \partial t\right) dz}{\sum_{l=1}^{N} \varphi^l \int_z E^l \left(\partial F^l / \partial t\right) dz}. \tag{3.12}$$

Here l is the component (e.g. DC, EC), N is the number of components (≥ 2), and φ^l is the solid mass fraction of the component l in the mantle source. The isotope ratio of pooled, vertically erupted magma is therefore

$$I = \frac{\sum_{l=1}^{N} I^l \varphi^l C_0^l \int_z E^l \left(\partial F^l / \partial t\right) dz}{\sum_{l=1}^{N} \varphi^l C_0^l \int_z E^l \left(\partial F^l / \partial t\right) dz} \tag{3.13}$$

where I is the isotope ratio of the pooled magma and I^l is the isotope ratio of component l. Also, with $I^{EC} = 1$ and $I^{DC} = 0$ in the numerator, I becomes the fraction of the total incompatible element content contributed by EC. We also predict the isotope composition of an individual volcano as it grows. This composition, I_V, is assumed to be the average composition of magma that is pooled from a cylindrical source volume:

$$I_V = \frac{\sum_{l=1}^{N} I^l \varphi^l C_0^l \int_\theta \int_{r_{volcano}} \int_z E^l \left(\partial F^l / \partial t\right) \sin\theta \, dr dz d\theta}{\sum_{l=1}^{N} \varphi^l C_0^l \int_\theta \int_{r_{volcano}} \int_z E^l \left(\partial F^l / \partial t\right) \sin\theta \, dr dz d\theta} \tag{3.14}$$

where theta is azimuth and $r_{volcano}$ is the radius of the volcano's capture area.

In order to understand what is controlling I_V in the discussion below, it is useful to introduce a quantity describing the "fractional contribution of each component" to the total mass of an incompatible element in the pooled volcano magma:

$$f_m = \frac{\varphi^m C_0^m \iint_{r_{volcano}} \int_z E^{\mathbf{m}} \left(\partial F^{\mathbf{m}} / \partial t\right) \sin\theta \, dr dz d\theta}{max\left(\sum_{l=1}^{N} \varphi^l C_0^m \iint_{r_{volcano}} \int_z E^l \left(\partial F^l / \partial t\right) \sin\theta \, dr dz d\theta\right)}. \qquad (3.15)$$

Here m represents an individual component, such as DC. The maximum in the denominator refers to the maximum concentration of an incompatible element that erupts at a given position in the volcano's path. Throughout the manuscript, we will show f_m versus position along the volcano path, and we will refer to this plot as the "contribution" of the m-component. We will now examine how mantle dynamics affects the surface pattern of compositions about the hotspot (3.13), the relative contribution of components to magma (3.15), and the isotopic composition of volcanoes passing over the hotspot (3.14).

3.3 Simulations of a Two-Component Mantle

In each of the following two-component simulations, a depleted peridotite component, "DC," is 90% of the starting solid (φ^{DC} = 0.9) and the remaining 10% is either an enriched peridotite component (EC; φ^{EC} = 0.1) or a pyroxenite component (PC; φ^{PC} = 0.1). Also, the starting concentrations of an incompatible element (C_0) and its bulk partition coefficients (D) in (3.11)-(3.15) are the same for all components, which eliminates extra variables to consider between components.

3.3.1 Spatial variations in the relative contributions of enriched (EC) and depleted (DC) components

Two reference models illustrate some of the important predictions and concepts. In one simulation, t_{plate} = 100 Ma, which produces a cool thermal boundary layer in which the 1000°C isotherm is shallower than ~85 km. In the other simulation, t_{plate} = 25 Ma and the lithosphere is thinner, with 1000°C isotherm being shallower than ~50 km. All other model parameters are the same (φ^{EC} = 0.1, X_w^{EC} = 400 ppm, Ra = 6.5 x 10^5, r_{plume} = 71.4 km).

Figures 3.1a and 3.1b show the predicted pattern of magma geochemistry for eruption on the old and young plate, respectively. In each case, a broad ring of magma with EC fraction (I_V) > 0.3 erupts at the distal edges of the hotspot (in fact, most of this magma is purely EC ($I_V = 1$)). This ring is wider for magma erupting over the older plate than over the younger and thinner plate. The purely EC rim surrounds a region of lower I_V (colored from yellow to blue) that encompasses most of the zone in which melt production is large. Also, in each case the magma pattern is asymmetric in the direction of plate motion. Compared to a circle, the geochemical pattern is compressed upstream and stretched downstream. Finally, above the younger plate, there is a small zone near the upstream side of the zone of high melt production (~650 km ≤ x ≤ 725 km) in which the EC fraction is locally elevated nearer the y-axis.

To help illustrate the causes of the geochemical patterns, we show the relative contributions of the two components (f_m as defined in Eq. 3.15) as a function of along-

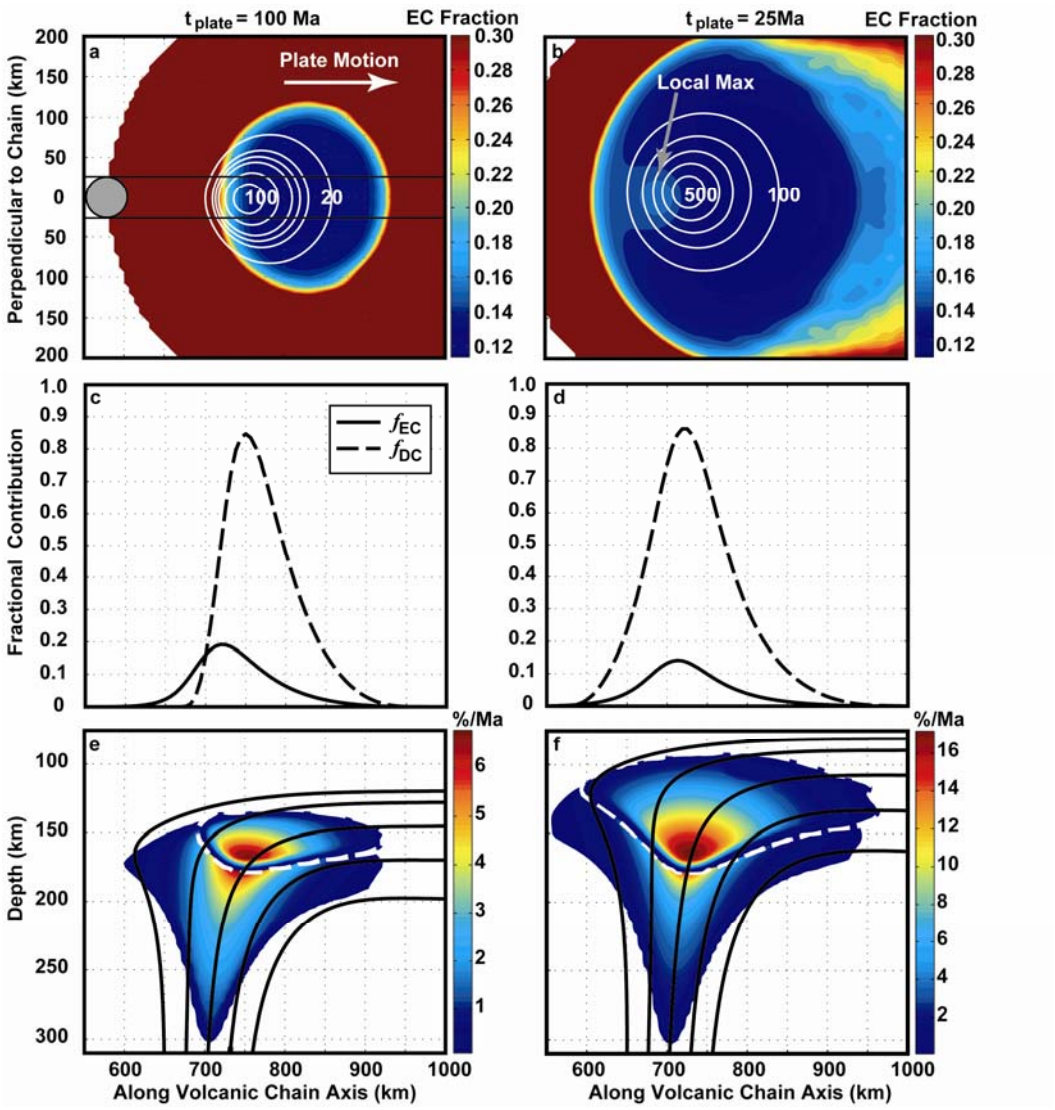

Figure 3.1 General model predictions. Predictions for two cases in which the age (t_{plate}) and thickness of the lithospheric plate entering the model domain differs: (left column) thickness of material cooler than 1000°C is ~85 km for t_{plate} = 100 Ma and (right column) thickness of material cooler than 1000°C is ~50 km for t_{plate} = 25 Ma. (a)-(b) Colors show the fraction of the total content of an incompatible trace element that was derived from EC in magma (referred to as "EC fraction" in text) erupted on to the seafloor (depth is into the page) (Eq. 13). White lines are eruption rate in km^3/Ma. The white arrow indicates direction of plate motion, the gray arrow highlights the location of a local maximum in EC fraction, the gray circular area indicates horizontal cross-section of a cylinder from which magma is pooled in a model volcano, and thin black lines indicate the path of an "on-axis" model volcano (i.e., passing directly over the hotspot center). (c)-(d) Fractional contribution of each component (EC and DC) to the total mass of an incompatible element in the pooled volcano magma (f_m; Eq. 15) for the volcano path depicted in (a). (e)-(f) Melting rate contours in %/Ma for the EC and DC melting zones. The DC melting zone is contained by the dashed white line and overlaps the EC melting. In this case, the water content of EC is X_w^{EC} =400 ppm and DC is anhydrous.

chain distance (x-axis) in Figure 3.1c and 3.1d. A component's contribution is positive at positions along the chain below which the component is melting, and the maximum contribution occurs (approximately) over the center of the component's melting zone. The width of EC contribution is greater than that of DC in both simulations because the EC melting zone is wider than the DC melting zone (Figures 3.1e - 3.1f). The general shape of each component's contribution and the fact that the distance between peak contributions is small compared to the horizontal length scale of the melting zones causes the generally radial composition patterns seen in Figures 3.1a and 3.1b.

A component's contribution is asymmetric about its peak in the direction of plate motion (Figure 3.1c and 3.1d); a particularly clear example is the contribution from DC as predicted by the case that simulates the thicker lithosphere. Contribution fractions remain larger farther downstream from the peak than upstream because the melting zones also extend farther downstream than upstream. Figures 3.1e and 3.1f show that plate motion diverts plume material downstream, where it continues to rise and melt while also inhibiting plume material from spreading upstream.

The local high in EC fraction between ~650 km $\leq x \leq$ 725 km along the chain (as apparent in the case with thinner lithosphere) is caused by enhanced EC melting in the plume stem. The EC fraction increases in this zone because f_{EC}/f_{DC} is greater relative to the composition at surrounding positions. Figures 2.1b and 3.1f show that the thickness of the EC melting zone increases more rapidly near the plume center relative to the thickness of the DC melting zone. Figure 2.1b also shows that the thickened portion of the EC melting zone produces magma of low melt fractions, which have high

concentrations of incompatible elements. These two effects increase f_{EC}/f_{DC} and thus the EC fraction near the plume stem. With that said, f_{EC}/f_{DC} does not increase in this location for all simulations. For example, beneath the thicker plate in Figure 3.1e, melting of EC is enhanced in the plume stem and thus f_{EC} increases; however, the positions where this is occurring coincide with the leading edge of the DC melting zone, and in this case f_{EC}/f_{DC} decreases. This zone in which the EC fraction locally increases is the reason prior models predicted on- and off-axis volcanoes to evolve with different compositions [*seeChapter 2*]. The model presented in that work had the same plate age as the older plate in Figure 3.1, but the Rayleigh number was doubled, and such a set of parameters predicts the zone of increasing EC near the plume stem. These competing effects are discussed below in greater detail.

3.3.2 Compositional evolution of a growing volcano

The remainder of the chapter will focus on predictions of the compositional evolution of a growing volcano, I_V (3.14). This compositional parameter is more straightforward to contrast between different models than the contour plots in Figure 3.1, and the quantity is easily compared to data.

Figure 3.2a shows I_V versus position for a volcano passing over the hotspot on the younger plate in Figure 3.1 (left column; t_{plate} = 25 Ma). Also shown is the volcano's cumulative volume normalized by the volcano's final volume (i.e., the cumulative fraction of total volume) versus position. For reference, the small local peak in EC fraction discussed above is evident at distances x = 650 to 680 km. Also, note that I_V = 0.5 at the same position where the contribution curves in Figure 3.1d intersect (i.e., where

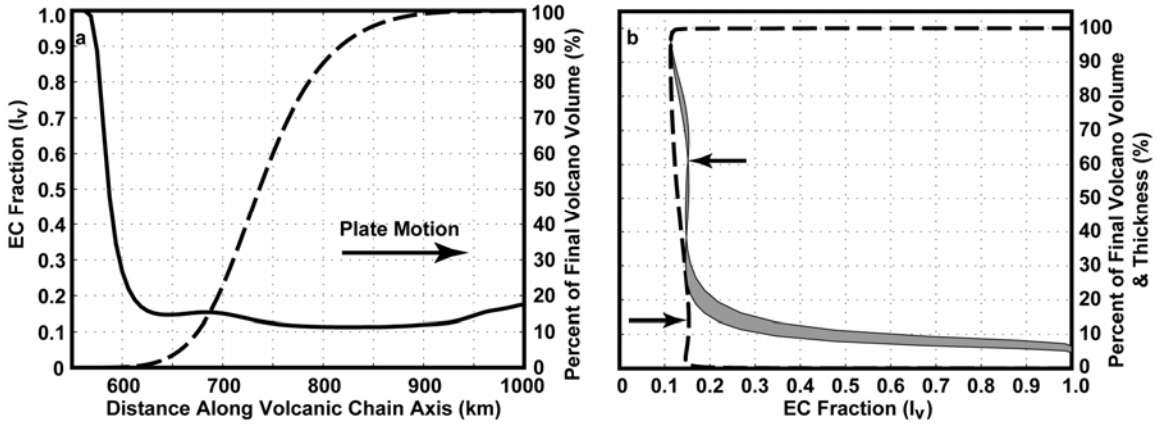

Figure 3.2 Volcano growth and composition. (a) Solid line is EC fraction (I_v, Eq. 14) versus position of a volcano (see Figure 3.1b, 3.1d, and 3.1f) that passes over a hotspot with a plate that is relatively thin, having cooled for a time of t_{plate} = 25 Ma. Note that EC fraction is 0.5 at ~580 km, and this is where the relative contribution curves intersect in Figure 3.1d. Dashed line is cumulative volume, shown as a percent of the maximum volcano volume. (b). Dashed line here plots the dashed vs. solid lines in (a). Gray band depicts the percent volcano thickness vs. composition. Thickness in a model volcano is converted from volume by the model of *DePaolo and Stolper* [1996], and the band shows the range of results from a range of volcano shapes used in their published models. Here, 0% thickness is the deepest and oldest part and 100% is the surface of a fully grown volcano. Only ~14% of the volume fills ~60% of the total thickness (marked by arrows).

contribution, f_m, is the same for both EC and DC). The largest change in I_V occurs during the first 10% of the cumulative volume.

Figure 3.2b shows how I_V changes with cumulative volume fraction as well as thickness fraction. Thickness fraction is the instantaneous thickness of a growing volcano normalized by the final thickness. We describe evolution in terms of thickness fraction mainly because it is more straightforward to compare to data collected for different stratigraphic depths [e.g. *Kurz et al,* 1995; 1996; *Lassiter et al., 1996*; *Bryce et al.*, 2005; *Salters et al.*, 2006]. We use the volcano growth model of *DePaolo and Stolper* [1996] to convert cumulative volcano volume to thickness. In this growth model, thickness accumulates by spreading incremental volumes of magma over the entire surface area of an approximately cone-shaped volcano. Thus thickness fraction accumulates faster with

volume in the early in the growth of a volcano compared to later. For example, in the models the first ~15% of the volume erupted accounts for the deepest ~60% of the total thickness.

3.3.3 Effects of lithosphere cooling age/thickness on volcano composition

Building from the two example cases shown in Figure 3.1, Figures 3.3a-c show the relative component contributions (f_m) of the two components versus distance along the chain, again for t_{plate} = 25 and 100 Ma, as well as for an intermediate age of 50 Ma. Figure 3.3d shows the corresponding thickness fraction versus volcano composition (I_V) for the same simulations. For all cases, the model predicts the volcano composition to first be purely EC (I_V = 1) and then to evolve to lower I_V with increasing thickness fraction. In all cases, the minimum I_V occurs at a thickness fraction of ~0.98. This decreases of I_V with increasing thickness fraction is in part due to the fact that plate motion moves the center of the DC melting zone downstream from that of EC, and thus DC contribution is higher (and I_V is lower) in the last 80% of volume accumulations (Fig 3.2a).

The maximum thickness fraction with purely EC composition at the very base of the volcano is ~0.20 for t_{plate} = 100 Ma and decreases to ~0.08 and to ~0.05 for t_{plate}= 50 and t_{plate} = 25 Ma, respectively. The dynamical cause is that older plates restrict the width of f_{DC} much more than younger plates, whereas the width of f_{EC} is approximately the same between these simulations. Therefore, volcanoes on thicker lithosphere spend relatively more time sampling purely EC magma at the beginning of their growth. The width of the

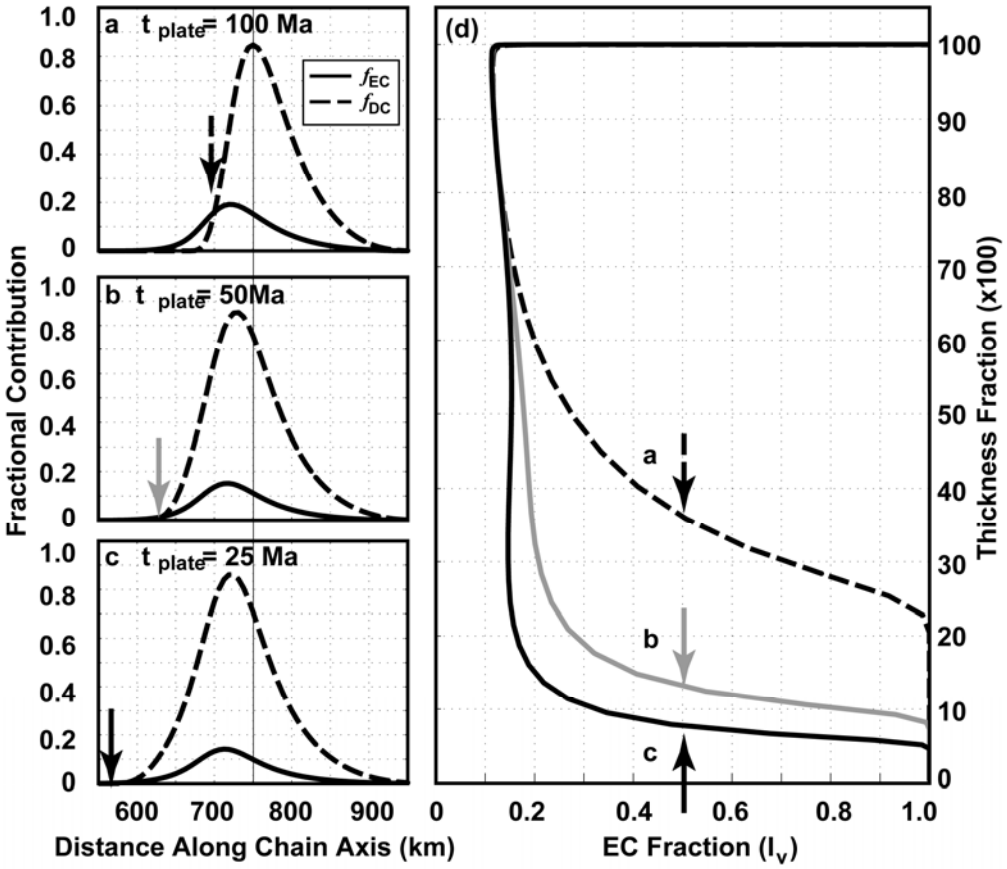

Figure 3.3 Simulations with different lithospheric thickness. Left column shows fractional contribution of each component to the total mass of an incompatible element in the pooled volcano magma (f_m Eq. 15) versus volcano position for cases with different cooling ages t_{plate} = (a) 100 Ma, (b) 50 Ma, and (c) 25 Ma. In all cases Rayleigh number (Ra) is 6.5 x 10^5, the plume maximum thermal anomaly (T_{plume}) is 290 K and drops by a factor of e at a radius (r_{plume}) of 71.4 km. The cylindrical volume from which volcano magma is pooled has a radius ($r_{volcano}$) of 25 km. The mass fractions of components are $\varphi^{DC} = 0.9$, $\varphi^{EC} = 0.1$, and finally, the water content of EC (X_w^{EC}) is 400 ppm. Arrows mark the volcano position at which f_{DC} (dashed lines) = f_{EC} (solid lines). Vertical line marks the position of peak DC contribution in (a) and extends through (b) and (c) for reference. (d) Predicted volcano thickness fraction versus composition for the cases shown in (a)-(c) as labeled. Arrows indicate the thickness at which $I_V = 0.5$, and correspond to the arrows in (a)-(c).

DC melting zone is more sensitive to plate age (i.e., thickness) because the DC melting zone is shallower than the EC melting zone.

Increasing plate cooling age also increases the fractional thickness above the layer of pure EC magmas over which the compositions transition from high to low I_V. To

understand the cause of this behavior, compare the heights of f_{EC} at the positions where f_{DC} first becomes non-zero in each simulation (Figures 3.3a-c). The magnitude of f_{EC} at these positions increases with t_{plate}, therefore lowering I_V to the same extent (e.g., from I_V = 1.0 to I_V = 0.5) requires a greater contribution of DC magma, which results in a greater thickness of magma over which the transition to low I_V occurs.

Figure 3.3d shows that between ~0.30 and 0.55 thickness fraction, I_V slightly increases in the case where t_{plate} = 25 Ma. The increase is another manifestation of the small increase in EC fraction between ~650 km ≤ x ≤ 725 km (Figure 3.1b) caused by an increase of f_{EC}/f_{DC} . This feature diminishes with increasing cooling age. In the model with t_{plate} = 50 Ma, I_V merely decreases at a lower rate between ~0.30 and 0.55 than for >0.55 thickness fraction, and in the model with t_{plate} = 50 Ma, no evidence of the plume stem melting is discernable. Plate motion offsets the upstream boundary and the peak of f_{DC} downstream from that of f_{EC}, and this offset increases with plate age. In the two cases with older plates, the offset is great enough that the increase in f_{EC} coincides with a rapid increase of f_{DC} over the plume stem and consequently f_{EC}/f_{DC} continues to decrease with volcano growth (Figure 3.3a-c).

3.3.4 Effects of Rayleigh number on volcano composition

We now examine how magma composition is influenced by Rayleigh number, or in particular, the reference viscosity η_o, which is arguably the least well-constrained property of the upper mantle beneath hotspots. Decreasing Ra (i.e., increasing η_o) decreases the upwelling rate of the buoyant plume material, and therefore the horizontal component of velocity due to plate shear is relatively larger compared to the vertical

component. Thus decreasing *Ra* increases the deflection of streamlines in the plume and enhances the associated compositional consequences.

Figures 3.4a-3.4c show component contribution curves for model simulations with t_{plate} = 100 Ma and Ra = 26 x 10^5, 13 x 10^5, and 6.5 x 10^5. We attempt to maintain an approximately constant thermal buoyancy flux of the plume, *B* [*Ribe and Christensen*, 1999], between the simulations by increasing the radius of the plume with decreasing *Ra* (r_{plume} = 50.5, 60.0, and 71.4 km; *B* = 4.96, 4.76, 3.43 Mg/s, respectively). Constant buoyancy flux eliminates a variable to consider when interpreting results. As in the prior cases, the surface boundary speed (u_{plate}~ 9.0 cm/a) is the same in the simulations.

Increasing *Ra* has the same qualitative effect on composition as decreasing plate thickness (i.e., t_{plate}). For high *Ra* (as for thinner plates), the EC and DC component contribution curves mostly overlap each other. Decreasing *Ra* (like increasing plate thickness) causes plate motion to more greatly shift DC melting downstream relative to EC melting, and to more greatly restrict DC melting upstream of its peak compared to downstream. Consequently, curves showing the corresponding thickness fraction versus composition (Figure 3.4d) differ with decreasing Ra in a similar manner to the predictions of the cases with increasing t_{plate} (Figure 3.3). The thickness of purely EC crust erupted at the beginning of volcano growth increases from ~0.03 to 0.20 thickness fraction with decreasing *Ra* (similar to model results with increasing t_{plate}). Also, the overlying transition in I_v from purely EC to low EC fraction occurs over an increasing thickness fraction with decreasing *Ra*. The similarities between Figures 3.3d and 3.4d thus reveal how changes in two different physical parameters (plate thickness and mantle

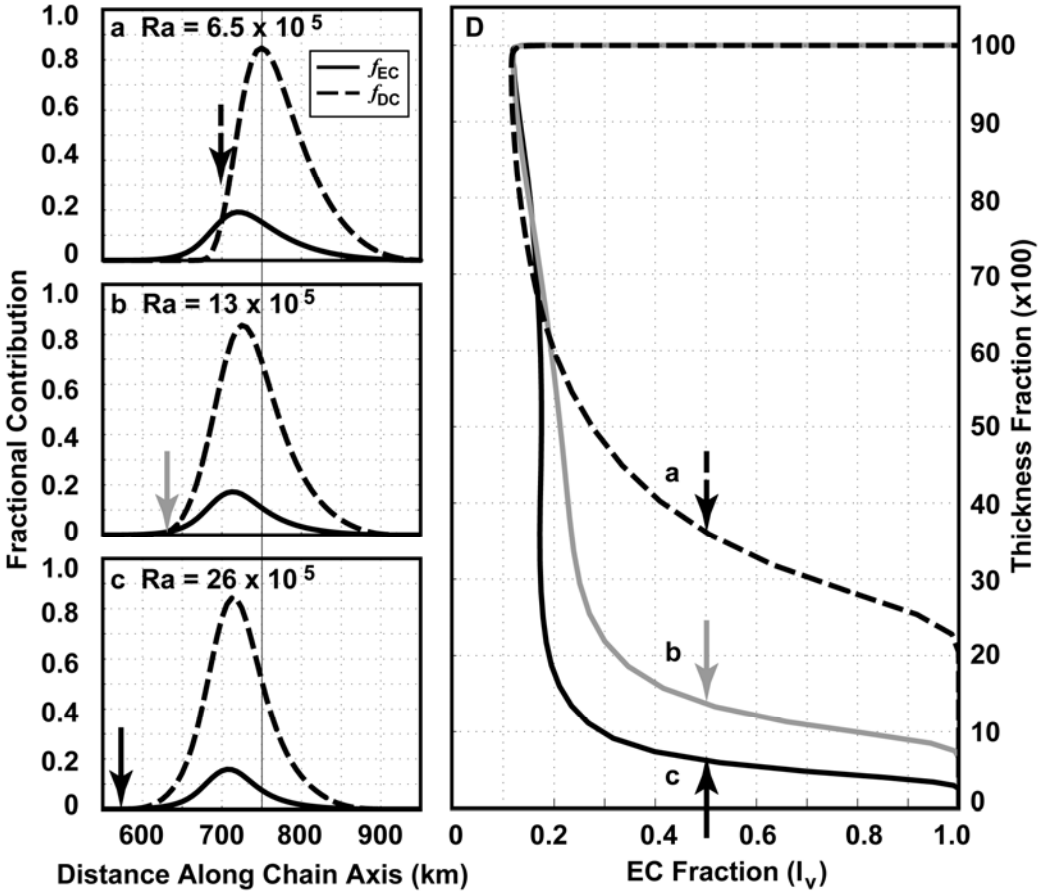

Figure 3.4 Simulations with different Rayleigh numbers. Left column shows fractional contribution of each component to the total mass of an incompatible element in the pooled volcano magma (f_m; Eq. 15) versus volcano position for cases with different Rayleigh number, *Ra* = (a) 6.5 x 10^5, (b) 13 x 10^5, and (c) 26 x 10^5; plume radii were adjusted to approximately preserve buoyancy flux as follows r_{plume} = (a) 71.4 km, (b) 60.0 km, and (c) 50.5 km. In all cases t_{plate} = 100 Ma, $r_{volcano}$ = 25 km, φ^{DC} = 0.9, φ^{EC} = 0.9, and X_w^{EC} = 400 ppm. Arrows mark the volcano position at which f_{DC} (dashed lines) = f_{EC} (solid lines). Vertical line marks the position of peak DC contribution in (a) and extends to (b) and (c) for reference. (d) Predicted fraction of volcano thickness versus composition for the cases shown in (a)-(c) as labeled. Arrows indicate the thickness at which I_V = 0.5, and correspond to the arrows in (a)-(c).

viscosity) similarly influence the geochemical evolution of a volcano through their effects on the degree to which mantle streamlines are tilted near the base of the melting zones.

3.3.5 Effects of solidus depth of EC on volcano composition

The final variable examined here is the difference between the depths at which the most fusible component begins melting. As mentioned above, if EC and DC had identical solidi and melting functions, the present models would predict all magmas to have the same composition everywhere. It therefore seems logical that the magnitude (and shape) of the geochemical variability should be sensitive to differences between the depths of melting of EC and DC.

The difference between the depths at which EC and DC begin melting is controlled by water content in EC, X_w^{EC} (since DC is dry, i.e. X_w^{DC} = 0). Figures 3.5a and 3.5b show model cases where X_w^{EC} = 400 ppm and X_w^{EC} = 200 ppm, respectively. In the two cases, the DC contributions are approximately the same. In the case in which EC is more hydrous (Figure 3.5a), the EC contribution curve is wider and has a greater peak than in the case in which EC is less hydrous (Figure 3.5b). These two differences result from a wider and thicker EC melting zone with increased water content.

The predicted effects of EC water content on volcano compositions are shown in Figure 3.5d. Compared to the case with less water, the case with more water has a thicker layer of purely EC magma at the base of the volcano, a higher EC fraction at most heights above this layer, and a slightly higher local maximum in I_V during the mid-thickness fraction of the volcano. Also, both cases predict approximately the same minimum I_V, which occurs at a thickness fraction of ~0.98; therefore, the range in I_V is approximately the same in both cases. However, the range in I_V in the second half of thickness accumulation (>0.50) is greater in the case with more water.

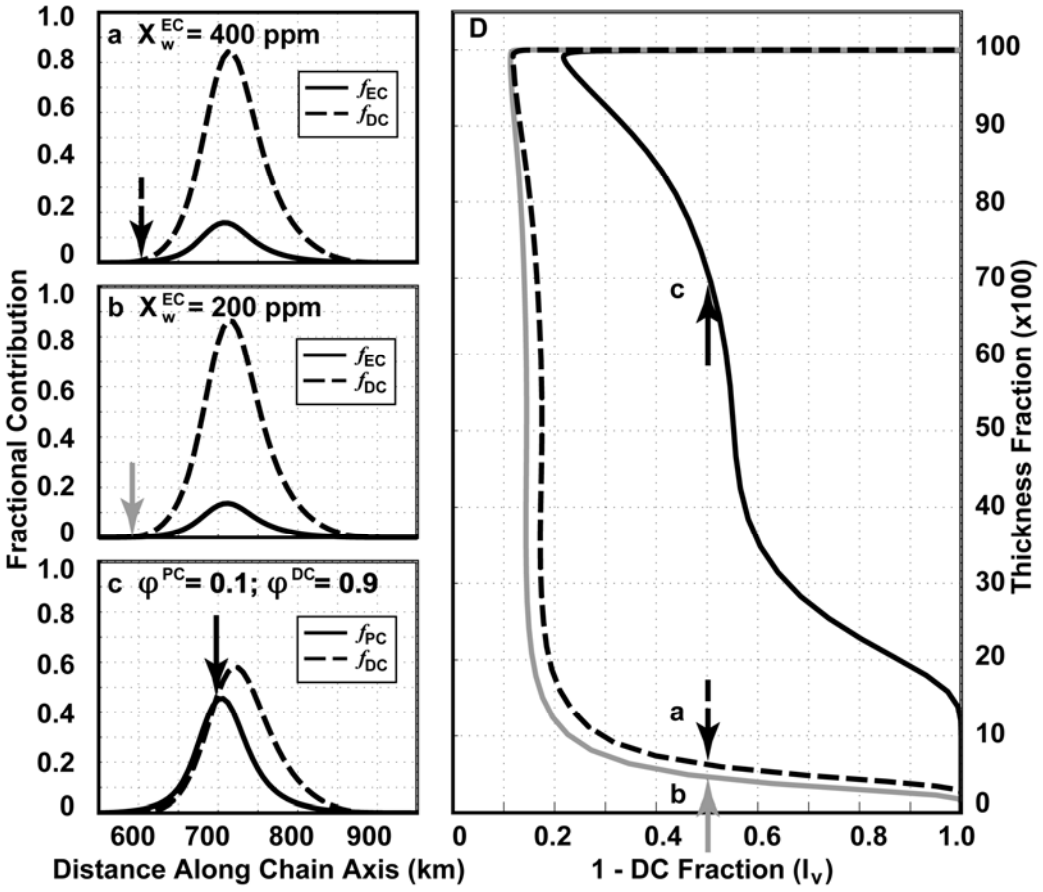

Figure 3.5 Simulations with different components. Left column shows fractional contribution of each component to the total mass of an incompatible element in the pooled volcano magma (f_m; Eq. 15) versus volcano position. (a)-(b) Cases in which the less refractory component is EC, and depth to the base of the EC melting zone is different between the two simulations, as controlled by the water content, (a) X_w^{EC} = 400 ppm (b) X_w^{EC} = 200 ppm with φ^{DC} = 0.9, and φ^{EC} = 0.1 in these cases. Arrows mark the volcano position at which f_{DC} (dashed lines) = f_{EC} (solid lines). In (c), pyroxenite (PC), rather than EC is the more fusible component, φ^{DC} = 0.9, φ^{PC} = 0.1. In all cases t_{plate} = 100 Ma, Ra = 13 x 10^5, r_{plume} = 60 km, and $r_{volcano}$ = 25 km. (d) Predicted volcano thickness fraction versus composition for cases shown in (a)-(c) as labeled. Arrows indicate the thickness at which I_V = 0.5, and correspond to the arrows in (a)-(c).

The differences in the above predictions follow simply from the differences in the thickness and width of EC melting zones between the two models. The larger thickness fraction of the purely EC lavas for the case with the more hydrous EC is caused by the greater water content widening the EC melting zone. Consequently, a longer time is spent erupting EC as the volcano moves over the melting zone. I_V is greater in

simulations with greater water content (over most of the thickness fraction) because greater water content increases the magnitude of f_{EC} everywhere. The EC contribution increases with water content because the EC melting zone is thicker. Also, most of the increase in thickness occurs at very low melt fractions, which control incompatible element composition in (11) - (15). The local high in I_V during the middle part of growth is greater with more EC water because the mantle depth over which plume stem melting occurs is greater. In the simulation with more hydrous EC, f_{EC} increases more rapidly over the plume stem because of a more rapid increase in the thickness of the EC melting zone. Meantime, f_{DC} is approximately the same in both models; therefore f_{EC}/f_{DC} and the associated increase in I_V is greater in the model with more hydrous EC. The minimum in I_V occurs downstream of the plume center, where a thick layer of melt depleted (EC and DC) material is diverted downstream and still is melting (Figure 2.1b). EC material in this region is largely dehydrated (by prior melting), and so initial EC water content does not significantly the minimum I_V.

3.3.6 A two-component mixture of PC and DC

Another case considers a pyroxentite component (PC) as the deep melting component, rather than enriched peridotite (EC). We model PC so that it begins melting at approximately the same depth as the prior case with EC in which X_w^{EC} = 400 ppm; therefore the new case does not differ from the previous cases in terms of the depth that melting begins. Rather, the major difference is that at low F, the rate and total extent of melting by PC productivity is many times greater than that of EC.

Figure 3.5c shows the relative contribution curves for the same physical model parameters as Figures 3.5a-3.5b, but with $\varphi^{PC} = 0.1$ and $\varphi^{DC} = 0.9$. In this case, although PC is only 10% of the solid mantle, its peak magma contribution is ~80% of the peak DC contribution, or roughly four times as high as the models with EC. Such high magma contributions sustain a high proportion of PC isotope composition throughout most of the growth of model volcanoes (Figure 3.5d). Here the $I_V > 0.2$ for all thickness, and nearly half of the overall change in I_V occurs after >50% of the volcano thickness has erupted. Therefore, if the mantle is a matrix of DC veined with PC, a small fraction of PC in the starting mixture can have a large effect on magma composition.

3.3.7 Discussion of two-component models and evidence at oceanic hotspots

Most samples and observations of hotspot volcano compositions are taken in the later stages of volcano growth, well above the thickness fraction at which the present models predict an extremely high EC fraction. Some important conclusions come follow from examining model predictions for thickness fraction >0.15 (Figures 3.3d, 3.4d, and 3.5d). The main findings are that the change in a volcano's composition (I_v) increases with the thickness of the lithosphere, decreases with *Ra*, and increases with the difference between the depths at which each component melts. Each of these variables influences the tilting (from vertical) of streamlines in the deeper portions of the melting zones where incompatible elements are most heavily extracted. To summarize the main results: the change in a volcano's average composition (I_v) above a thickness fraction of 0.15 increases with the tilt of streamlines near the base of the melting zones. The tilt of streamlines increases with the ratio of horizontal to vertical velocity in the melting zone. Observables such as plate velocity and plume buoyancy flux are likely to relate simply to

the horizontal and vertical velocities near the base of the melting zones, respectively. In addition, increasing seafloor age may increase the tilt of streamlines near the base of the melting zone because the viscous lithosphere is thicker. Thus, observations of plate velocity, plate age, and plume buoyancy flux may be used to apply predictions to the character of compositional evolution of volcanoes at a variety of hotspots.

An example hotspot at which observations have been made of composition as a function of time and the aforementioned physical conditions is Réunion. Previous authors have documented that the average $^{208}Pb/^{204}Pb$ in samples over a given interval of the stratigraphic section spanning >500 ka of eruptions of Piton de la Fournaise on the Réunion hotspot decreases from the oldest samples to the youngest [*Bosch et al.*, 2008], which is consistent with a steady increase in the contribution of a more depleted component (i.e., lower $^{208}Pb/^{204}Pb$) as a volcano passes over the melting zone as predicted by the present models. Assuming the final elevation of Piton de la Fournaise is 2.5 km, we estimate the total thickness at the sample sites of 7.5 km [*Gallart et al.*, 1999] and calculate that the observed decrease in $^{208}Pb/^{204}Pb$ occurs over the upper ~23% of the volcano thickness. At Mauna Kea volcano in the Hawaiian hotspot, the average $^{208}Pb/^{204}Pb$ also decreases over the final 25% of thickness as evident in the Hawaiian Scientific Drilling Project (HSDP) data [*Abouchami et al.*, 2000; *Eisele et al.*, 2003; *Blichert-Toft et al.*, 2003]. To directly compare the change in average $^{206}Pb/^{204}Pb$ with time at Mauna Kea and Piton de la Fournaise and relate any differences to model predictions, we normalize the observed change in average composition at Mauna Kea and Piton de la Fournaise by the total range observed at each hotspot [*Abouchami et al.*, 2005; *Luais* 2004; *Bosch et al.*, 2008]. The average $^{206}Pb/^{204}Pb$ observed at Piton de la

Fournaise changes by ~20% of the range, and at Mauna Kea by ~35% of the range, both over the final 25% of the volcanoes' thicknesses. Note that the average composition measurements are influenced by the thickness of stratigraphic segments used to compute the average with thickness fraction, and also that the range observed at Hawaii may be influence by the fact that sampling at Hawaii is more extensive than at Réunion.

The Hawaiian hotspot is beneath an older plate part of a plate than Réunion (~90 Ma versus ~65 Ma) [e.g., *Müller et al.*, 1997], and current plate velocity is faster at Hawaii (~70 km/Ma versus ~25 km/Ma) [e.g., *Gripp and Gordon*, 2002]. The model predicts these differences cause a greater ratio of horizontal to vertical velocity (thus greater plume tilt) beneath Hawaii, and consequently that the fractional change in average $^{208}Pb/^{204}Pb$ with age should be greater at Mauna Kea than at Piton de la Fournaise. This prediction is consistent with the estimation differences between the observed compositions at the two volcanoes described above. However, a higher buoyancy flux beneath Hawaii (8.7 Mg/s versus 1.9 Mg/s [*Sleep*, 1990]) likely indicates a larger upwelling velocity, which lowers the ratio of horizontal to vertical velocity, and thus counteracts the effects of the older, faster-moving plate at Hawaii. Considering the competing differences between the hotspots, the larger fractional change in average $^{208}Pb/^{204}Pb$ with age observed at Mauna Kea may reflect that the difference in plate velocity and age is relatively more influential on composition than buoyancy flux when comparing these two hotspots.

In another example, the Samoan hotspot occurs over a part of the lithosphere that is approximately the same thickness as that beneath Hawaii (~110 Ma, versus ~90 Ma)

[e.g., *Müller et al.*, 1997] and current plate velocity is similar (~70 km/Ma in both locations) [e.g., *Gripp and Gordon*, 2002]. However, *Sleep* [1990] estimates that buoyancy flux at Hawaii is more than five times greater than that at Samoa. The present models would therefore predict that the average composition of Samoan volcanoes should show more change over their lifetime compared to Hawaiian volcanoes. While the compositional evolution of a single volcano at Samoa is not well sampled, the composition of volcanoes with increasing distance from the hotspot shows a steady decrease in $^{206}Pb/^{204}Pb$ [*Workman et al.*, 2004]. Thus, younger volcanoes (in earlier stages of growth) have higher $^{206}Pb/^{204}Pb$, which is consistent with model predictions if the shallower melting component has a lower $^{206}Pb/^{204}Pb$ composition. This change with distance spans ~85% of the range in $^{206}Pb/^{204}Pb$ seen at Samoa, At Hawaii, the change is comparable or slightly lower, which we estimate to be ~75%, from Loihi to Koolau volcano [*Abouchami et al*., 2005 and references therein], consistent with the model predictions.

3.4 Simulations of a Three-Component Mantle and Comparisons with Geochemical Data from Hawaii

3.4.1 Three-component models and observations at Mauna Kea, Hawaii

We now examine the geochemical manifestations of a three-component mantle and compare the predictions to data from the HDSP. In order from deepest solidus to shallowest (i.e., least to most refractory), the components in the model mantle are EC, PC, then DC (in the reference model φ^{EC} = 4%, φ^{PC} = 8%. Φ^{DC} = 88%). In terms of $^{208}Pb/^{204}Pb$ and $^{206}Pb/^{204}Pb$ ratios, EC has relatively moderate values, PC has the highest

values, and DC has the lowest values (see Table 3.2 for the assumed compositional parameters). The model plate age is 100 Ma and $Ra = 13 \times 10^5$.

There are four phases to the compositional evolution of the model volcano (Figure 3.6a). Phase 1 comprises the deepest 3% of the volcano thickness, and is characterized by a shift in composition from EC toward PC. Phase 2 encompasses the next interval from ~0.03 to 0.25 thickness fraction, in which the composition remains mostly constant and is dominated by PC (high Pb isotope ratios). Phase 3 occurs from 25% to 99% thickness fraction, and in this phase composition evolves from high to low Pb isotope ratios, indicating an increasing contribution from DC. Finally, Phase 4 occurs for thickness fraction >99% and approximately erupts compositions following the changes in Phase 1-3 in reverse order.

The volcano composition of a reference model is plotted in $^{208}Pb/^{204}Pb$ versus $^{206}Pb/^{204}Pb$ space (Figure 3.6b). Phase 1 falls on a line between the EC and PC end member compositions because only these two components are yet contributing magma (i.e., binary mixing). Phase 2 is the single point with constant, and the greatest, $^{208}Pb/^{204}Pb$ and $^{206}Pb/^{204}Pb$ ratios. Phase 3 follows a line that is shifted to slightly lower $^{206}Pb/^{204}Pb$ values for a given $^{208}Pb/^{204}Pb$ than a binary mixing line between PC and DC. The shift of this mixing trend away from the PC-DC line toward the EC composition is caused by the EC magma contribution throughout the growth of the model volcano.

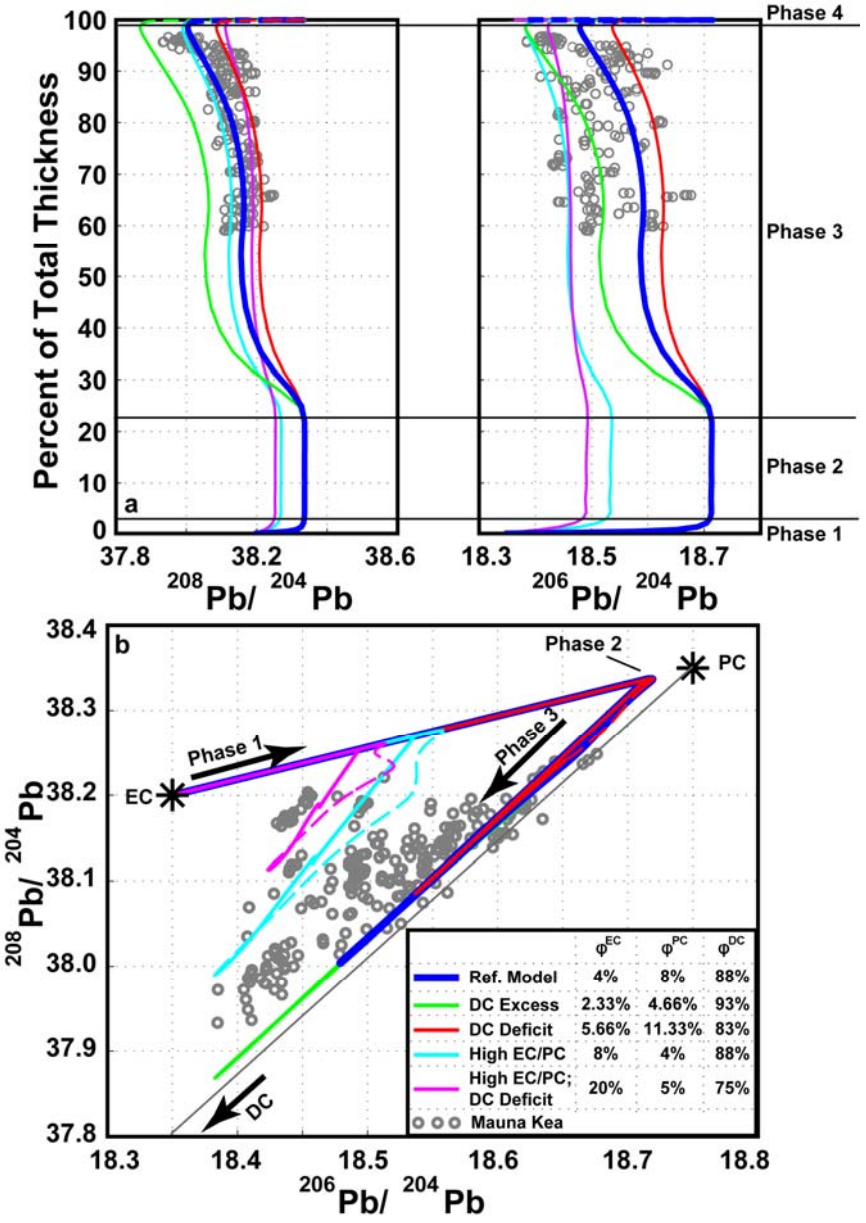

Figure 3.6 Three-component simulations and observations at Mauna Kea. (a) Volcano thickness fraction versus composition. Drill depths of the Mauna Kea samples (gray circles) [*Abouchami et al.*, 2000; *Eisele et al.*, 2003; *Blichert-Toft et al.*, 2003] are normalized to 7.5 km, the approximate thickness of the volcanoes at the sample locations [see *Wessel*, 1993; *Kurz et al.*, 1996]. Horizontal black lines separate four phases of the compositional evolution (see text). Colored lines are volcano composition (I_V; Eq. 14) for simulations in which the mass fractions of components are different. See Tables 3.2 and 3.3 for the values of all model parameters related to composition. The compositional trend during final and fourth phase of the evolution is dashed. (b) Model and observed Mauna Kea compositions in $^{208}Pb/^{204}Pb$ versus $^{206}Pb/^{204}Pb$ space. Symbols, colors, and line styles are as in (a). Stars mark the EC and PC composition; the short arrow points toward the DC composition ($^{208}Pb/^{204}Pb = 37.4$, $^{206}Pb/^{204}Pb = 18.05$). Thin gray line shows the predicted compositions that would occur by binary mixing between PC and DC. The long arrows indicate the trends of Phases 1 and 3 of the compositional evolution.

Phase 3 produces a wide range of compositions and also is the interval during which the majority the volcano volume erupts. Compositions in Phase 3 exhibit behavior similar to pseudo-binary mixing [*Hanan et al.*, 1986; *Schilling et al.*, 1992; *Douglass and Schilling*, 2000]. The mixing trend is nearly linear because, although three components are mixing in varying proportions, the relative contributions of EC and PC are not changing, (nor does f_{EC}/f_{PC} change during Phase 2; see Figure 3.6a) and the relative contribution of DC is increasing rapidly. The result is that the compositional trend in Phase 3 does not extend toward any of the component compositions, but rather from the composition of Phase 2 (a mixture between EC and PC) and the mean composition of the three-component source mixture. Thus three-component melting and mixing complicates any inferences about the compositions of the actual materials in the mantle from geochemical data.

To compare model predictions with observations at Hawaii, Figure 3.6a shows $^{208}Pb/^{204}Pb$ and $^{206}Pb/^{204}Pb$ values collected in the Mauna Kea section of the HSDP drill core [*Abouchami et al.*, 2000; *Eisele et al.*, 2003; *Blichert-Toft et al.*, 2003], where the sample depths have been normalized to 7.5 km, the approximate total thickness of Mauna Kea at the drilling site [see *Wessel*, 1993; *Kurz et al.*, 1996]. At each depth of the drill core the Pb isotope ratios span a range of values. For most of the deeper section drilled, the average $^{206}Pb/^{204}Pb$ does not change systematically with depth and the average $^{208}Pb/^{204}Pb$ ratio shows only a weak upward trend of decreasing value. However, in the very shallowest (>90% thickness fraction) portion of the core, the averages of $^{208}Pb/^{204}Pb$ and $^{206}Pb/^{204}Pb$ both decrease. In comparison, the reference model predicts Pb isotope

ratios to remain approximately constant between ~0.40 and -0.80 thickness fractions and then to decrease substantially in the shallowest 20% of the volcano height. This prediction captures the general trends in the average compositions along the HSDP core.

The same data are plotted in $^{208}Pb/^{204}Pb$ versus $^{206}Pb/^{204}Pb$ in Figure 3.6b. The large scatter in the data about a rough trend cannot be well described with a single, straight mixing line. Correspondingly, pseudo-binary mixing like that predicted in Phase 3 also cannot explain the scatter in the $^{208}Pb/^{204}Pb$ versus $^{206}Pb/^{204}Pb$ data. Thus, even with three components melting in the mantle, the present model of heterogeneity is too simple to explain Hawaii data. One possibility is that the mass fractions (φ^m) of the components in the mantle source beneath Mauna Kea vary in space.

Figure 3.6 includes the results of calculations with different φ^m (see Table 3.3 for φ^m in each simulation). For all calculations, the magma production rate of the reference model is used to calculate volcano thickness. These calculations predict that increasing φ^{DC} decreases the minimum $^{208}Pb/^{204}Pb$ and $^{206}Pb/^{204}Pb$ ratios during Phase 3, but does not affect the first and second phase because DC does not yet contribute to the magma during these phases. Other simulations show that increasing the amount of EC relative to PC (i.e., $\varphi^{EC}/\varphi^{PC}$) lowers $^{206}Pb/^{204}Pb$ for a given $^{208}Pb/^{204}Pb$. Together, the predicted compositions with the different starting source compositions span most of the data.

The above predictions imply that the range necessary to explain HSDP Pb data is $\varphi^{m}_{ref} \pm 15\%$. Others have forwarded similar explanations for compositional variations at Kilauea at short timescales (10^{-4} Ma) [e.g., *Marske et al.*, 2007] and moderate length

scales (102 km) [e.g., *Farnetani and Hofmann*, 2009]. The different three-component simulations discussed above cannot be used to infer over what length scale (or timescale) φ^m must vary; however, the length scale must be smaller than the dimensions of melting zones (10^2 km) in order to preserve the predictions (and predictions) discussed in section 3.3. In this way, the model attributes compositional scatter to random spatial and temporal variations in φ^m while attributing compositional trends with stratigraphic depth (particularly $^{208}Pb/^{204}Pb$, $^{206}Pb/^{204}Pb$, and ε_{Nd}) to systematic variations in the contribution of components (f_m). In other words, we interpret the scatter of the data about the average trends to reveal variability in source composition within the plume beneath Mauna Kea, whereas the average trends show the process by which these materials are extracted by melting.

3.4.2 Three-component models and Kea and Loa subchains, Hawaii

Previous work attributed differences in composition between the (Mauna) Loa and (Mauna) Kea subchains at Hawaii to differences between the compositions of on- and off-axis volcanoes [*see Chapter 2*]. Off-axis volcanoes pass at some distance from the center of the hotspot, and they have a distinctly different shield stage composition from on-axis volcanoes in simulations that predict a local high in the contribution of the less refractory components on the axis, such as that illustrated in Figure 3.1b. The previous work, however, did not address the Pb isotope data for Hawaii, which show that, compared to Loa-trend volcanoes, Kea-trend volcanoes tend to have higher values of $^{208}Pb/^{204}Pb$ and $^{206}Pb/^{204}Pb$, as well as a higher $^{206}Pb/^{204}Pb$ for a given $^{208}Pb/^{204}Pb$ [e.g., *Abouchami et al.*, 2005].

A model with a locally high contribution from EC would predict higher $^{206}Pb/^{204}Pb$ for a given $^{208}Pb/^{204}Pb$ for off-axis volcanoes, but such a model would require a strong local high not seen in any of the current simulations. Similarly, a model with a local high in PC would predict higher $^{206}Pb/^{204}Pb$ and $^{208}Pb/^{204}Pb$ for on-axis volcanoes than for off-axis. The latter model would explain the differences between Loa and Kea shields versus depth, as demonstrated for ε_{Nd} in previous work [*see Chapter 2*]. However, neither simulation would fully explain differences between Loa and Kea subchains in $^{208}Pb/^{204}Pb$ versus $^{206}Pb/^{204}Pb$ space.

Both differences in Pb isotope data between Kea and Loa volcanoes can be explained if the mantle beneath the Loa chain has lower φ^{PC} and greater φ^{DC}. This conclusion may be deduced from Figure 3.6b, and the argument is similar to those of other authors [e.g., *Abouchami et al.*, 2005; *Farnetani and Hofmann*, 2009]. Thus, Kea and Loa compositions may arise from the same components melting in the mantle if there is some zoning of φ^{m}. The nature of melting a moderately zoned, veined mantle will be addressed in future work.

3.5 Conclusions

Upper mantle dynamics influence the pattern of magma composition erupted at a hotspot in the presence of uniform, small-scale mantle heterogeneities if the heterogeneities have different melting behavior as a function of depth. Plate motion tilts rising plumes resulting in the center of the melting zones of more refractory component(s) to manifest downstream from those of less refractory component(s). One important prediction is that incompatible elements from the least refractory components

rise first on the leading or upstream side of the melting zone and that the contribution from more refractory components increases with distance downstream. Consequently, simulations predict volcano composition evolves during growth starting from that of a deep-melting, enriched component(s) to one with increasing influence from the shallow-melting, depleted component(s). What is most important to this prediction is the tilting of the mantle streamlines at depths near the base of the melting zones of the components, where incompatible elements are being preferentially extracted. Factors that increase the tilt at these depths include increasing lithosphere thickness (or seafloor age), increasing plume viscosity (or decreasing Rayleigh number), and decreasing water content of the enriched component. Larger plume tilt causes a larger thickness fraction near the base of the volcano to be composed of the enriched component(s) and a greater thickness fraction over which the compositions transition toward the compositions of the depleted component. These predictions can explain some aspects of compositional evolution at Hawaii, Réunion, Samoa, and likely other localities, if the shallowest-melting component is associated with isotope compositions that indicate long-term depletion of incompatible trace elements relative to deeper-melting components. Further, differences in the evolution and geochemical pattern at these and other hotspots may arise simply from differences in plume tilt near the base of the melting zone, as it is influenced by observable conditions such as plate velocity, plate age, and plume buoyancy flux.

Models that simulate a mantle source with three components also predict volcano composition to evolve with increasing influence from the least to most refractory component. In the reference model, a volcano first erupts purely EC magma and quickly begins to erupt a mixture of EC and PC magma. The composition of the magma remains

nearly constant, until a mixture of EC, PC, and DC magma begins to erupt. The latter phase produces most of the magma and produces compositions that trend between an extreme composition involving a mixture of EC and PC and a second end-member composition being the mean composition of the underlying mantle. Therefore, when a volcano samples three components, the pooled composition does not evolve toward any of the mantle end-member compositions, but rather to mixtures of mantle end members. This possible behavior should be considered in future interpretations of multi-dimensional isotope diagrams.

A reference model with three components explains the average trend of the compositional evolution of Mauna Kea exhibited in HSDP data. However, explaining the scatter in the same data requires either non-uniform heterogeneity, spatially and temporally variable sampling of different components, incomplete magma mixing, or a combination of all three. Thus, the model attributes average compositional trends to melting of a veined mantle under the influence of plume-lithosphere interaction, and attributes scatter about the average compositional trends to variability in the source. Finally, models successfully predict sub-parallel mixing lines in Pb isotope space, as is observed in differences between Loa and Kea compositions. In this case, the veined mantle has the same end-member compositions, but the mantle beneath the Loa subchain must have relatively less PC.

Table 3.1 General Constants and Variables in Chapter 3

Symbol	Meaning (Defining Eq.)	Value	Units
c_p	Specific heat capacity	1000	J/(mol K)
C_l	Concentration of incompatible element in liquid (12)		‡
C_0	Concentration of incompatible element in initial solid		‡
D	Bulk distribution coefficient		†
Di	Dissipation number	0.1568	†
E	Enrichment factor of incompatible element (11)		†
E_a	Activation energy	1.20×10^5	J/mol
F	Total melt fraction		%
F_e	Equilibrium melt fraction (7)		%
f_m	Fractional contribution of component m (15)		†
I	Isotope ratio of pooled magma; EC Fraction (13)		†
I^i	Isotope ratio of component *i*		†
I_V	Isotope ratio of pooled magma in a volcano (14)		†
$\hat{\mathbf{k}}$	Vertical unit vector		‡
$\dot{M}$	Melting rate (10)		%/Ma
P	Pressure		‡
Q	Heat (4)		J
R	Gas constant	8.314	J/(mol K)
Ra	Rayleigh number	6.5×10^5, 13×10^5, 26×10^5	†
r_{plume}	Radial measure of thermal anomaly	50.5, 60.0, 71.4	km
$r_{volcano}$	Radius of volcano source cylinder	25	km
ΔS	Liquid-Solid entropy change	300	J/(K)
T	Absolute temperature		K
T'	Temperature above solidus (8)		‡

Table 3.1 (Continued) General Constants and Variables in Chapter 3

Symbol	Meaning (Defining Eq.)	Value	Units
T_{liq}	Liquidus temperature		‡
t_{plate}	Half-space cooling age at x = 0	25, 50, 100	Ma
T_{plume}	Maximum thermal anomaly	290	K
T_r	Reference temperature	1573	K
T_{sol}	Solidus temperature		‡
u	Velocity		‡
u_{plate}	Plate velocity	90	km/Ma
w	Vertical velocity		‡
x	Model length; "Position along volcanic chain axis"	0-1600	km
X_w	Peridotite water content	0 - 400	ppm
y	Model width; "Position perpendicular to chain"	0-800	km
z	Model depth	0-400	km
z_{max}	Maximum model depth	400	km
γ	Adiabatic gradient (6)		‡
η	Dynamic viscosity		‡
η_o	Reference viscosity	5.0×10^{19}, 1.0×10^{20}, 2.0×10^{20}	Pa s
θ	Azimuth		radians
φ	Mass fraction of component		†

† denotes naturally dimensionless parameter
‡ denotes non-dimensionalized parameter

Table 3.2 Constants in Three-component Simulations

	Depleted Peridotite (DC)	Enriched Peridotite (EC)	Pyroxenite (PC)
$^{208}Pb/^{204}Pb$	37.4	38.2	38.35
$^{206}Pb/^{204}Pb$	18.05	18.35	18.75
C_0 §	0.40	1.0	4.0
D	0.0075	0.0075	0.0642

§ Normalized to C_0^{EC}

Table 3.3 Mass Fractions (x 100) in Three-component Simulations

	Depleted Peridotite (DC)	Enriched Peridotite (EC)	Pyroxenite (PC)
Reference Model	88	4	8
DC excess	93	2.33	4.67
DC deficit	83	5.67	11.33
High EC/PC	88	8	4
High EC/PC; DC deficit	75	20	5

Chapter 4

Geochemical variations at ridge-centered hotspots caused by variable melting of a veined mantle plume

Abstract

Geochemical observations at ridge-centered hotspots offer clues into the nature of mantle composition and melting feeding volcanism. For example, observations at Iceland show that lava composition varies with distance along the ridge axis, gradually shifting from relatively incompatible-element enriched compositions near the hotspot to relatively depleted compositions far from the hotspot. These observations indicate that the mantle is compositionally heterogeneous below the Mid-Atlantic Ridge, with the expression of at least one "enriched" component being strongest on Iceland and waning with distance away from Iceland. The progressive decrease in this hotspot influence on the ridge has been interpreted with two classes of hypotheses: (1) the plume is compositionally distinct from the ambient asthenosphere and the gradients reflect progressive dilution of the plume with ambient mantle along the ridge axis and (2) gradients reflect variation in melting of the same heterogeneous source. This work tests the second class of hypotheses. We model the dynamics of flow and melting of a ridge-centered, veined mantle plume and predict the geochemical composition of magma at the surface. It is assumed that the heterogeneous mantle comprises two types of peridotites: one is relatively enriched in incompatible elements ("EC"), begins melting deeper owing to a higher water content, comprises 10% of the mantle and exists as uniformly sized veins or blobs (of order $\leq 10^0$ km), the other is a relatively depleted component ("DC") that begins

melting shallower due to a lower water content, and constitutes the remaining 90% of the mantle. Spatial variations in mantle flow and melting are found to cause EC to be more heavily sampled toward the hotspot center. The main qualification for this result is that the extraction of water by melting increases mantle viscosity. The along-axis width of the high EC contributions increases with the Rayleigh number, plume radius, and thermal buoyancy flux of the plume. The magnitude of the maximum EC anomaly at the hotspot increases with Rayleigh number. A subset of model calculations designed to simulate the Iceland hotspot and Mid-Atlantic Ridge predicts an appreciable fraction of the total range and widths of observed variations in crustal thickness, $^{87}Sr/^{86}Sr$, and La/Sm. To more closely match the observations requires the plume material to have a lower mass fraction of DC (3% less), or higher $^{87}Sr/^{86}Sr$ (0.0002 higher in DC). While the present models require that the Icelandic mantle plume be compositionally distinct from the ambient upper mantle, if the same Iceland plume mantle were melted under normal ridge conditions the resulting composition would fall within the observed range of mid-ocean ridge basalts world wide. The broader implication is that strongly distinct compositional reservoirs are not required in the deep mantle to explain observations along the Mid-Atlantic Ridge near Iceland.

4.1 Introduction

Variations in the composition and the thickness of crust along mid-ocean ridges are often attributed to influence of a buoyant mantle plume [e.g., *Wilson*, 1963; *Vogt*, 1971; *Morgan*, 1972; *Schilling*, 1973, *Hart et al.*, 1973; *Sun et al.*, 1975]. For example, at Iceland, crust thickness is up to ~40 km [*Darbyshire et al.*, 1998] and decreases to normal, average global thickness (~6 km [*White et al.* 1992; *Dick et al.* 2003]) with

distance to the north along the Kolbeinsey Ridge, and to the south along the Reykjanes Ridge [e.g., *Weir et al*., 2001; *Menke*, 1999; *Hooft et al*., 2006]. The thickening of crust with proximity to Iceland has been well explained by a thermally buoyant plume centered beneath the Mid-Atlantic Ridge (MAR) [e.g., *Ito et al.*, 1999]. Further, seismic studies conclude that a thermal anomaly is present in the upper 400 km of the mantle with a radius between 75 km and 200 km (over which the anomaly decreases by a factor of 1/*e* of the maximum) [e.g., *Wolfe et al.*, 1997; *Foulger et al.*, 2000; *Hung et al.*, 2004]

Accompanying the anomaly in crustal thickness are anomalously high $^{206}Pb/^{204}Pb$, $^{87}Sr/^{86}Sr$, $^{3}He/^{4}He$, and La/Sm and low $^{143}Nd/^{144}Nd$, as well as additional compositional anomalies, which change gradually with distance from Iceland [e.g., *Hart et al.*, 1973; *Schilling*, 1973; *Sun et al.*, 1975; *O'Nions and Gronvöld*, 1973; *O'Nions and Parkhurst*, 1973; *O'Nions et al.*, 1973; *Wood et al.*, 1979; *Zindler et al.*, 1979; *Cohen and O'Nions*, 1982; *Hemond et al.*, 1988; *Mertz et al.*, 1991; *Hanan and Schilling*, 1997; *Schilling et al.*, 1999]. These geochemical observations imply that the source of volcanism beneath Iceland has a long-term enrichment of incompatible elements relative to the surrounding "normal" mid-ocean ridge source (e.g., that the Icelandic source, through time, has been processed less at melting zones). Two end-member classes of hypotheses exist to explain the geochemical observations: (1) the first class considers most of the hot mantle upwelling, or "mantle plume" beneath Iceland to be compositionally distinct from the ambient asthenosphere and attributes gradients in magma geochemistry along the MAR to progressive dilution of the plume with ambient upper mantle [*Schilling*, 1973; *Hart et al.*, 1973] or (2) the second class of explanations emphasizes small-scale heterogeneity in

both materials and attributes gradients in composition to reflect plume-related variations in melting of this heterogeneous source [*Ito and Mahoney*, 2005a, b].

The traditional and most common interpretations for the Iceland hotspot tend to be nearer the first class of hypotheses above, which requires distinction between the upper mantle and the plume source. Most workers certainly agree that the hot upwelling mantle beneath Iceland is heterogeneous, but disagree regarding the nature of this heterogeneity. For example, a "depleted" component with relatively low $^{87}Sr/^{86}Sr$ and an "enriched" component with relatively high $^{87}Sr/^{86}Sr$ are necessary to explain the range of $^{87}Sr/^{86}Sr$ observed at Iceland and the decreasing ratios away from Iceland. Some authors have suggested that the upwelling plume beneath Iceland contains depleted material that is distinct from the depleted material sampled at normal ridges to explain some of the observations [e.g., *Thirlwall*, 1994; *Hards et al.*, 1995; *Fitton et al.*, 1997; *Breddam*, 2002]. Other authors argue that the depleted plume component is not distinct from the depleted component in normal mid-ocean ridge basalts (NMORB) [*Mertz and Haase*, 1997; *Hanan et al.*, 2000; *Stracke et al.*, 2003]. Further, some workers conclude that long and short wavelength as well as temporal variations in composition at Iceland can be explained by three-component mixing in which much of the material upwelling in the plume is relatively homogeneous, and is compositionally distinct from a heterogeneous, ambient upper mantle [*Hanan and Schilling*, 1997; *Hanan et al.*, 2000]. The main difficulty with this class of hypotheses is that previous geodynamic models of a mantle plume rising beneath a mid-ocean ridge fail to predict significant mixing between material native to the plume and material native to the ambient upper mantle [*Hauri et*

al., 1994; *Ito et al*., 1999; *Farnetani et al.*, 2002], nor do they predict significant melting of entrained material [*Farnetani and Richards*, 1995].

Alternatively, the second class of hypotheses, in which variations in melting a single heterogeneous source cause along-axis changes in magma composition, has not been explored with 3D geodynamic models of a ridge-centered mantle plume. Recent work shows that differences in the mantle flow and lithospheric thickness associated with mid-ocean ridges and hotspots cause different magma compositions between these settings, and that local geographic variations in hotspot magma composition arise from local variations in dynamics and melting, even when considering a uniformly heterogeneous (i.e., veined) mantle [*Ito and Mahoney*, 2005a, b, 2006; *Bianco et al.*, 2005; *see also Chapters 2 and 3*]. This work assumed that the different compositional components in the mantle begin melting at different depths and have different melt productivities. If so, the dynamics of buoyant, rising plumes tend to enhance the contribution of deeper-melting components in the incompatible-element composition of pooled magma, which were assumed to have relative long-term enrichment of incompatible elements.

This study systematically examines the composition and thickness of crust formed above and near a ridge-centered plume by melting of a two-component, veined mantle. As in previous work [*see Chapters 2 and 3*], we simulate upper mantle flow, heat transfer and melting in 3D, and predict the composition and volume of pooled magma along the ridge. We test the effects of a rheology that is dependent on the temperature as well as the water content of the mantle, the latter of which can control the effective thickness of the lithosphere beneath young seafloor. Further, we vary the radius of the thermal anomaly

that forms the plume, and the reference viscosity of the mantle, which are not well constrained at hotspots worldwide. These parameters control the height and width of the crust and geochemical anomaly associated with the hotspot, and these simulations are used to illustrate and quantify how these key characteristics of along-axis geochemical anomalies depend on mantle conditions. Finally, to test which aspects of geochemical anomalies might arise from variable melting of a veined mantle, we compare predictions to observations of $^{87}Sr/^{86}Sr$, La/Sm, (which capture robust features of the geochemical anomaly at Iceland, [e.g., *Hanan et al.*, 2000]) and crustal thickness at Iceland and the adjacent MAR to the north and south.

4.2 Methods

Many aspects of the methods used in this work are summarized in *Chapter 3*. We simulate upper mantle convection of an incompressible, infinite-Prandtl-number fluid with CITCOM, a Cartesian coordinate, finite element code. We invoke the extended Boussinesq approximation and account for cooling due to latent heat of melting and adiabatic decompression in the energy equation (see Eqs. 3.1-3.4). Melting is calculated with the use of passive tracer advection and parameterizations of hydrous peridotite melting. Finally, the mantle in these models is uniformly heterogeneous (veined), and the heterogeneities are assumed to be in thermal equilibrium, but in chemical disequilibrium. In this section, we discuss the changes to the model from that outlined in Chapter 3.

4.2.1 Model Setup, Boundary, and Initial Conditions

The general model setup is shown in Figure 4.1. All models include the upper 400 km of mantle (z-dimension), and ≥1600 km of ridge axis (y-dimension) and ≥800 km in the

direction of plate motion (x-axis). In all models, vertical resolution above the deepest solidus is 5 km (and ≤ 9 km below the deepest solidus) and horizontal resolution is 6.25 km. To achieve a steady state and to insure that simulation results are comparable, calculations were run for ~100 Ma of model time.

As in the previous chapters, the initial temperature condition is set using a half-space cooling model [*Davis and Lister*, 1974], and in all cases the age at the ridge ($x = 0$) is set to 0.01 ka to allow for a lithosphere of finite thickness. We impose the same form of thermal anomaly to initiate a plume as in Chapters 2 and 3, however in this chapter the center of the anomaly is at (x, y) = (0, 0) km, where the temperature is 200 K above the ambient potential temperature of 1573 K. Plate motion is simulated with a horizontal velocity boundary condition of 10 km/Ma imposed on the top of the model space. The vertical walls beneath the ridge ($x = 0$) and slicing through the center of the hotspot ($y = 0$) are reflecting boundaries. All other boundaries are open to material flow with zero conductive heat flow [*Ribe and Christensen*, 1999]. Thus, the symmetry of the problem allows us to simulate one quarter of the full volume of a ridge-centered plume system.

4.2.2 Rheology

Viscosity will be controlled by temperature-dependent Newtonian rheology, and we add an additional term to consider the effect of dehydration of the solid mantle on its viscosity. Water is empirically known to reduce

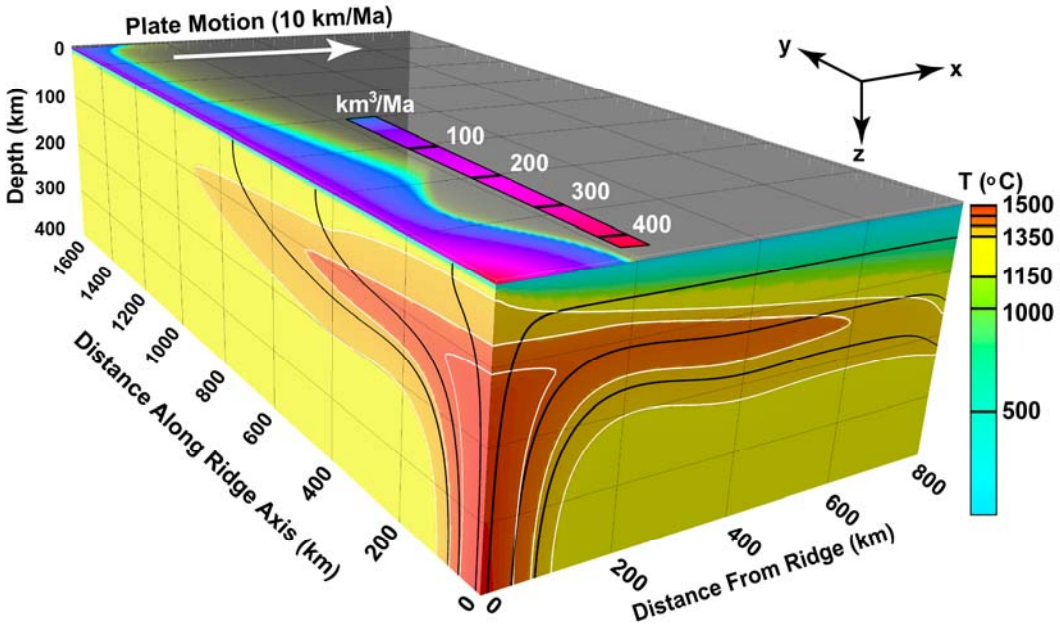

Figure 4.1 Ridge-centered model. Vertical slices through the model domain show projections of the 3D potential temperature in shades of blue (cool) to red (warm). Total depth (*z*-axis) of simulation is 400 km and horizontal dimensions are ≥1600 km along the ridge axis (*y*-axis), and ≥800 km in the direction of plate motion ("distance from ridge"; *x*-axis). Horizontal resolution is 6.25 km, and vertical resolution is 5 km at depths shallower than the deepest melting in the model (~220 km in most simulations) and is 9 km resolution below the melting zone. Black lines are streamlines and white lines mark potential temperatures of 1350 °C, 1400 °C, and 1450 °C. The combined eruption rate from components is contoured on the horizontal surface and is ~5 times greater over the center of the thermal plume. We model a veined mantle that is 90% anhydrous peridotite ("DC") and 10% hydrous peridotite ("EC").

the viscosity of olivine by multiple orders of magnitude in plausible mantle concentrations [*Hirth and Kohlstedt*, 1996; *Hirth and Kohlstedt*, 2003]. The extraction of water due to partial melting therefore may strongly affect the mantle flow and melting associated with plume-ridge interaction [*Ito et al.*, 1999]. Laboratory experiments [*Hirth and Kohlstedt*, 2003] show that, when assuming modal melting, the water and temperature dependence on viscosity η may be expressed as,

$$\eta = \eta_o \left(\frac{X_s^w}{X_o^w} \right)^{-r} exp\left[\frac{E_a}{R} \left(\frac{1}{T} - \frac{1}{T_r} \right) \right] \tag{4.1}$$

where η_o is the reference viscosity, E_a is the activation energy, R is the gas constant, T is absolute temperature, and T_R is absolute reference temperature. Also, X_0^w is the concentration of water in the starting mantle prior to melting, X_s^w is the concentration in the solid residue, and r defines the exponential dependence of viscosity on water content.

The present formulation has the same form as (4.1) but with adaptations needed to simulate melting as well as two mantle components with different water contents. We assume water fractionation between solid and liquid phases is controlled by modal fractional melting, such that

$$X_s^{\mathbf{w}} = X_0^{\mathbf{w}} \left(1 - F\right)^{1/D-1} = X_0^{\mathbf{w}} E \tag{4.2}$$

Here $X_0^{\mathbf{w}}$ is the weight fraction of water (ppm), F is the extent of partial melting and D is the bulk distribution coefficient, for which we assume $D = 0.01$ [*Michael*, 1995]. E is the solid's depletion of water content relative to its original concentration. The part of the viscosity function that depends on water content, μ, is therefore

$$\mu = \alpha\left(X_0^{\mathbf{w}} E\right)^{-\mathbf{r}} \tag{4.3}$$

where α is a proportionality constant that is assumed to be the same in all components, and will divide out when viscosity is normalized. Equations (4.1)-(4.3) therefore show that viscosity will increase as water is extracted from the solid via partial melting.

The system we simulate is a mixture of two components with different starting water contents. To calculate the effective viscosity of such a veined mantle, we start by examining a case of plane shear (Couette) flow involving two layers with different

viscosities. By the description of shear stress in one- and two-layer plane Couette flow [e.g., *Lai et al.*, 1993], we take

$$\frac{\mu_{eff}}{b_1 + b_2} = \frac{\mu_1 \mu_2}{\mu_2 b_1 + \mu_1 b_2} \tag{4.4}$$

where μ_{eff} is the effective viscosity of the two layers, b_1 and b_2 are the thicknesses of the top and bottom layers, and μ_1 and μ_1 are their respective viscosities. Solving (4.4), we find that the effective viscosity is described by the harmonic mean of the layers' viscosities, which we assume relates to the mass fraction of the mantle components, such that

$$\frac{1}{\mu_{eff}} = \frac{\varphi_1}{\mu_1} + \frac{\varphi_2}{\mu_2} \tag{4.5}$$

where φ_l is the thickness (mass) fraction layer of l. We therefore assume that the effective viscosity in a mantle containing a mixture of two components with different viscosities is described by (4.4).

Rearranging (4.4) and combining it with (4.3) yields

$$\frac{1}{\mu_{eff}} = \frac{\alpha\left({}^{1}X_0^{w} E_1\right)^{-r} \varphi_2 + \alpha\left({}^{2}X_0^{w} E_2\right)^{-r} \varphi_1}{\mu_1 \mu_2}, \tag{4.6}$$

where ${}^{l}X_0^{w}$ is the initial water content and E_l is the relative depletion in component l. Normalizing (4.5) by the effective viscosity prior to melting (i.e., E_l = 1), the dimensionless viscosity is

$$\mu'_{\mathbf{eff}} = \left(E_1 E_2\right)^{-r}\left[\frac{\left({}^{1}X_0^{\mathbf{w}}\right)^{-\mathbf{r}}\varphi_2 + \left({}^{2}X_0^{\mathbf{w}}\right)^{-\mathbf{r}}\varphi_1}{\left({}^{1}X_0^{\mathbf{w}}E_1\right)^{-\mathbf{r}}\varphi_2 + \left({}^{2}X_0^{\mathbf{w}}E_2\right)^{-\mathbf{r}}\varphi_1}\right], \tag{4.7a}$$

Note that (4.7a) can be rewritten to show that the limit in the case ${}^{1}X_0^{\mathbf{w}} = 0$ is $\mu'_{eff} = E_1\,\varphi_1/\varphi_2$. In the instance when $F = 0$, we find $E_1 = 1$, and therefore $\mu'_{eff} = 1$, but as $F \to 1$, $\mu'_{\mathbf{eff}} \to \infty$. We limit dehydration so that

$$1 \le \mu'_{\mathbf{eff}} \le \mu_{lim} \tag{4.7b}$$

to remain within realistic estimates (μ_{lim} = 100 unless noted) [*Hirth and Kohlstedt*, 1996; *Hirth and Kohlstedt*, 2003]. Finally, we assume constant activation energy in the upper mantle. Thus non-dimensional dynamic viscosity is given by

$$\eta = \mu'_{\mathbf{eff}}\, exp\left(\frac{1}{T}\right) \tag{4.8}$$

where in this case T is the non-dimensional absolute temperature. Therefore, (4.7)-(4.8) state that unmelted mantle (i.e., F = 0 for all components) at the ambient absolute temperature has a viscosity of η = 1. In model simulations, we input define Rayleigh number, *Ra*, which in turn defines dimensional reference viscosity η_0 as in the previous chapters. Because μ'_{eff} is normalized by μ_{eff} prior to melting, *Ra* does not depend on starting water content: water content does not influence the initial dimensional reference viscosity but only how much and how quickly viscosity increases with melting and dehydration. This formulation is advantageous in allowing us to easily examine the effects of varying *Ra* ($\sim 1/\eta_0$) and X_w separately.

4.2.3 Geochemistry and crust thickness

This work predicts the composition of magma that erupts above a ridge-centered hotspot and along the adjacent mid-ocean ridge due to melting of a veined mantle. We emphasize that there is no compositional difference between the initial composition of the plume source and beneath the ridge. The methods of this study are outlined in Chapter 3. Equation (3.11) defines incompatible element partitioning between the solids and liquids with modal fractional melting, (3.12) defines the concentration of an incompatible element in magma that rises vertically and pools at the surface (from all components), and (3.13) defines the and the isotope ratio of the pooled magma at the surface.

To quantify how magmatic isotopic composition varies along the ridge, we pool magma in the direction of plate motion by integrating horizontally and vertically,

$$I_R = \frac{\sum_{l=1}^{2} I^l \varphi^l C_0^l \int_x \int_z E^l \dot{M}^l \, dz dx}{\sum_{l=1}^{2} \varphi^l C_0^l \int_x \int_z E^l \dot{M}^l \, dz dx}. \tag{4.9}$$

Here I_R is the isotope ratio of pooled magma at some position along the ridge, I^l is the isotope ratio of component l, C_0^l is the initial concentration of an incompatible element in component l, and $\dot{M}^l$ is the local melting rate of component l, which is positive inside melting zones and zero outside of them (see Eq. 2.10, Ch. 2). In simulations with $I^{EC} = 1$ and $I^{DC} = 0$, I_R is equal to the "EC fraction", or the fractional contribution of EC to the incompatible-element composition of the pooled magma.

In addition to the composition, we estimate the crustal thickness of pooled magma at the ridge according to

$$h_c = \frac{\rho_m}{\rho_c} \frac{1}{u_{plate}} \sum_{l}^{2} \varphi^l \int_x \int_z \dot{M}^l dz dx, \quad (4.10)$$

where ρ_m and ρ_c are mantle and crust density (3300 and 2800 kg/m^3, respectively) and u_{plate} is plate velocity. With a reference mantle temperature of T = 1325 °C, the present model predicts a crustal thickness of 4-5 km for a normal ridge that is spreading at the rate representative of Iceland, 10 km/Ma. This thickness range is consistent with observed global averages at this spreading rate [*White et al.* 1992; *Dick et al.* 2003].

4.3 Simulations of Ridge-Centered Plumes

This section discusses how key characteristics of an along-axis geochemical anomaly, such as the amplitude and wavelength, depend on mantle dynamics. We simulate plumes rising beneath a mid-ocean ridge for a range of mantle conditions. In each simulation, there are two peridotite components with different water contents. One component, "DC", is 90% of the starting solid (φ^{DC} = 0.9) and the other, "EC", is 10% of the starting mantle (φ^{DC} = 0.1). Unless otherwise noted, the initial water content of DC and EC is 1 ppm and 400 ppm, respectively. As in Chapter 3, the starting concentration of an incompatible element, C_0, in (4.9) and the related bulk partition coefficient, D, is the same for both components. Also, the bulk partition coefficient of water is the same for both components. Finally, in equation (4.9), I^{DC} = 0 and I^{EC} = 1.

4.3.1 Effects of water-dependence of viscosity on ridge composition

Figure 4.2a shows the fraction of EC in the incompatible element composition along the ridge (I_R; (4.9)) for simulations in which viscosity depends on both temperature and water (the exponent in equations (4.6) and (4.7) is r = 1, and μ_{lim}= 100) and in which

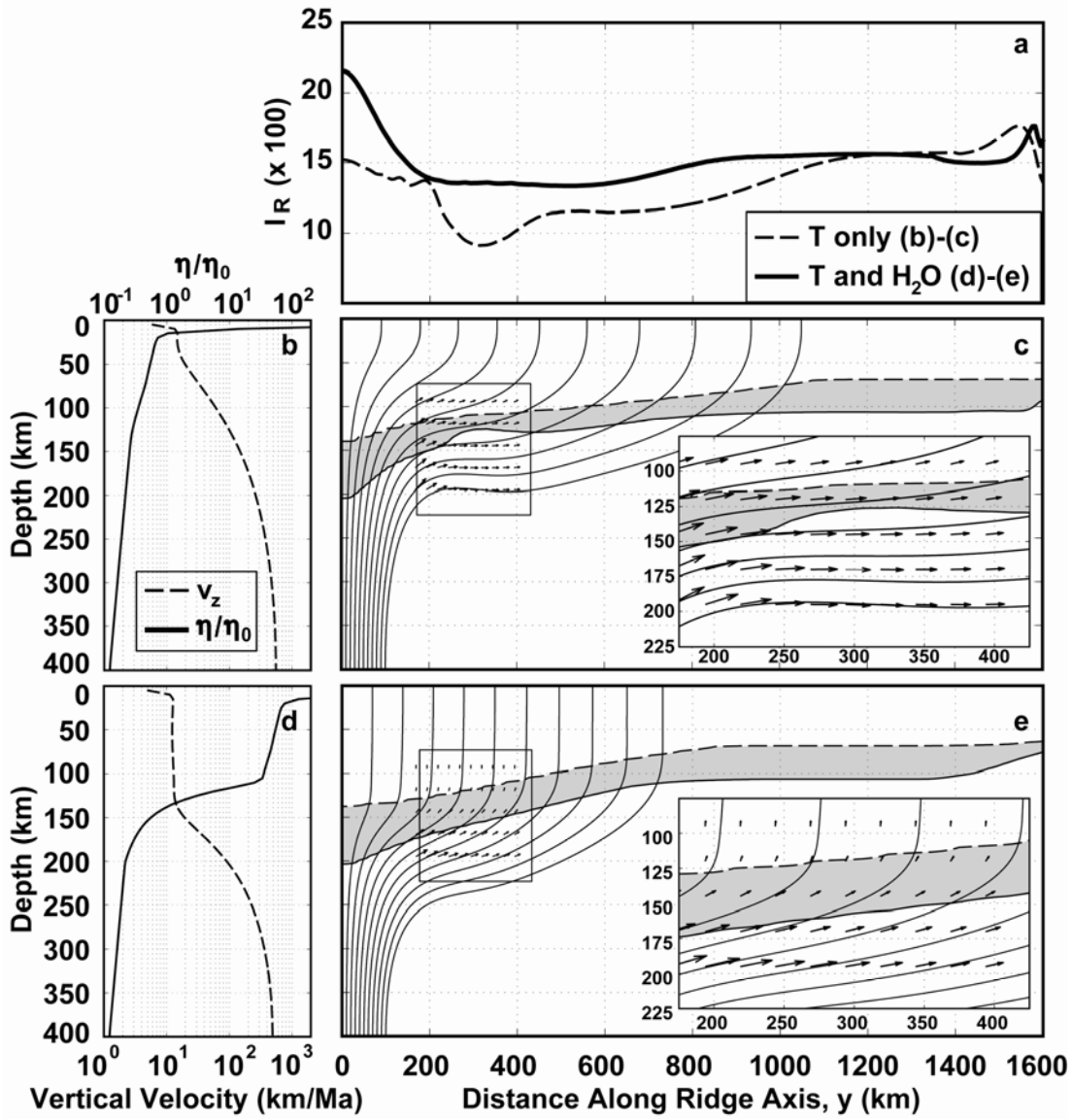

Figure 4.2 The effects of water-dependent viscosity. (a) Composition in pooled magma (I_R; EC fraction; Eq. 4.9) along the ridge (y-axis in Fig 1) where distance is measured from the center of the plume (y = 0) as in Figure 4.1. We present predictions for cases in which viscosity depends only on temperature, such that exponent r = 0 in (Eq. 1) (dashed line) and in which viscosity also depends on the bulk water content of mantle peridotite with r = 1.0 (solid line). (b) Non-dimensional mantle viscosity (solid line, top horizontal axis) and vertical velocity (dashed line, bottom horizontal axis) versus depth, at the plume center (i.e., x = 0, y = 0) for the simulation in (a) that has r = 0. (c) Thin black lines are streamlines. Gray region is the area in which EC melting rate is >0.05%/Ma (0.05%/Ma is contoured with a solid black line) and DC is not melting; both components melt above the dashed line. Inset shows a magnification of the boxed area. Arrows are velocity vectors with length proportional to speed. (d) Same as (b), but for the simulation in which r = 1. (e) Same as (c), but for the simulation in which r = 1.

viscosity depends on temperature only and not water (r = 0). In both simulations, the EC fraction is relatively high over the center of the plume, decreases along the ridge to the sides of the plume, then begins a gradual increase at an along-axis distance from the plume of y ~350 km in the temperature-only case and y ~600 km in the water-dependent case. I_R eventually levels-off to the "normal" ridge value of ~0.15 farther away from the plume. The distance to this normal-ridge composition, Δy_{norm} (see Figure 4.3b), is one key measurement made to characterize the plume influence on the ridge; it is a shorter distance in the water-dependent case (~900 km) versus the temperature-only case (~1200 km). At y ~1400-1600 km along the ridge axis, both simulations are influenced by boundary effects that are artifacts of the model design and therefore will be ignored in the discussion below. In the case with water-dependent viscosity (r = 1), I_R is greater at the hotspot center than in the temperature-dependent only case (r = 0). The magnitude of I_R relative to normal ridge is ΔI_R (see Figure 4.3b), and is another key measurement that characterizes the geochemical anomaly caused by the plume; it is positive only in the case with water-dependent viscosity. Also, I_R is low and remains approximately constant between y ~200 km and y ~600 km in the water-dependent case, whereas a local dip in I_R occurs between these positions in the temperature-only case. The distance to the minimum I_R, Δy_{min} (see Figure 4.3b), is the final key measurement made to characterize the geochemical anomaly over the plume. Thus, we will discuss a long- (Δy_{norm}) and short-wavelength (Δy_{min}) geochemical anomaly caused by the plume.

The width (Δy_{min}) and magnitude (ΔI_R) of the short-wavelength anomaly are related to the convective vigor and radius, r_{plume}, of the mantle plume stem. Buoyant upwelling of the plume enhances EC melting relative to DC because upwelling and thus

decompression rate increases with depth, and the base of the EC melting zone is deeper than that of DC. I_R is even greater over the hotspot in the case with water-dependent viscosity because the stiffening of the dehydrating solid reduces vertical velocity and melting rate at the base of the DC melting zone (Fig. 4.2b and 4.2d). Buoyant upwelling is most prominent over the center of the plume and decreases with distance away over the width of rising plume.

The long-wavelength compositional anomaly with low I_R (Δy_{norm}) is related to the along-axis extent of plume spreading. In both cases in Figure 4.2, diminished upwelling near the base of the plume layer partially causes the long-wavelength low I_R. Normally, passive mantle upwelling accommodates plate separation, but in these two simulations, plume material spreading in the direction of plate motion accommodates some of the plate separation, thus diminishing deep upwelling. This effect is enhanced in the case with (only) temperature-dependent viscosity because the base of the lithosphere is shallower. Figures 4.2c and 4.2e show mantle flow streamlines, velocity vectors, and the 0.5%/Ma melting rate contours of the EC and DC melting zones. Although velocity is greater in the temperature-only case than in the water-dependent case, the vertical velocity component is smaller. The lower vertical velocity decreases melting rate more in EC, decreases the difference in depth between EC and DC melting, and thus causes relatively lower I_R. The prominent minimum in EC content at y = ~300 km predicted in the temperature-only case is caused by very low vertical velocity, and the lateral transfer of material previously melted (and depleted in water) in the plume. The difference in depth between the EC and DC 0.5%/Ma contours is smallest below this prominent minimum.

Finally, beyond the long-wavelength plume influence, I_R levels out at the composition of the normal model ridge (I_R ~0.15) where there is no excess plume temperature or buoyant flow. Normal ridge composition occurs closer to the hotspot center in the case with water-dependent viscosity than in the temperature-only case because shallow (<200 km) along-axis flow of plume material is diminished.

4.3.2 Effects of the water-dependence exponent *r* on ridge composition

Figure 4.3 shows crustal thickness (h_c; (4.10)) and composition along the ridge for simulations in which r = 1.0 and for r = 1.5 (with μ_{lim}=100 for both); the range of r determined by in laboratory experiments is within the range tested here [*Hirth and Kohlstedt*, 2003]. We also include a "normal-ridge" simulation without a plume and r = 1.0 (a fourth simulation with X_w^{DC} = 100 ppm is shown and discussed below). In all three cases, X_w^{DC} = 1 ppm and X_w^{EC} = 400 ppm. Far from the ridge, both simulations predict approximately the same thickness (h_c ~4.1 km) and composition (I_R ~0.15), which are also approximately equal to the crustal thickness and composition in the simulation with no plume. However, the case with the greater water-sensitivity (r = 1.5) predicts smaller magnitudes of anomalies in h_c and ΔI_R. Also, increasing the exponent r decreases the long-wavelength distance along the ridge to normal composition (Δy_{norm}) and thickness, but there is no discernable difference in the distance to the minimum I_R (Δy_{min}).

Increasing the exponent r decreases I_R (and EC fraction) near the center of the hotspot because the difference in vertical velocity between the base of the EC and DC melting zones decreases (Fig. 4.4a and 4.4b). Because the EC begins melting at the same depth in both simulations, dehydration begins increasing the viscosity at the same depth,

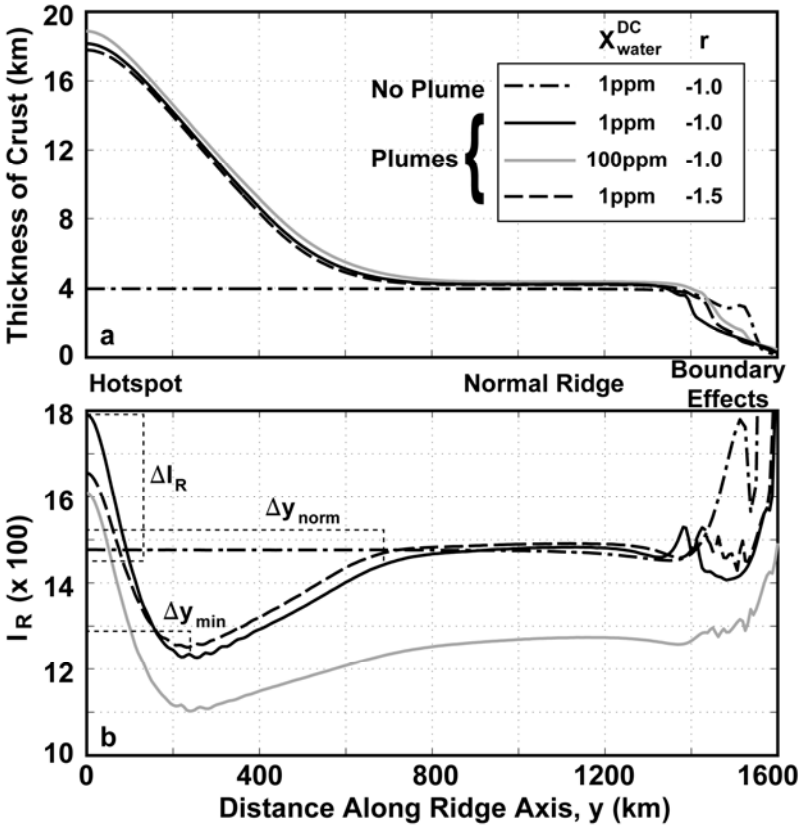

Figure 4.3 Crust and composition in simulations with different water-dependence and water content. (a) Crust thickness (h_c; Eq. 4.10) along the ridge axis for simulations with different dependence of viscosity on water and with different initial DC water contents. Models include a simulation with no plume (dash-dotted line), a simulation in which X_w^{DC} = 1 ppm and r = 1.0 (solid black line), a simulation in which X_w^{DC} = 1 ppm and r = 1.5 (dashed line), and a simulation in which X_w^{DC} = 100 ppm and r = 1.0 (solid gray line). Artifacts of the right-side boundary are apparent within ~200 km of the end of the model box, and should be ignored. (b) EC fraction (I_R; Eq. 4.9) of an incompatible element in pooled magmas along the axis for the same simulations as in (a). The height of the geochemical anomaly is ΔI_R, the distance to the minimum EC fraction (the width of the short-wavelength anomaly) is Δy_{min}, and the distance to normal-ridge composition (the width of the long-wavelength anomaly) as Δy_{norm}.

but viscosity increases much more rapidly with greater r. That is, the "effective" thickness of the lithosphere increases with r, and therefore the rising plume begins to slow and spread at a greater depth in this case. The vertical velocity near the base of the EC melting zone decreases with increasing r but the vertical velocity near the base of the

DC melting zone is not sensitive to this difference in r. This decrease in vertical velocity decreases the relative contribution of EC to I_R.

4.3.3 Effects of DC water content on ridge composition

Figure 4.3 shows crustal thickness and composition for one simulation in which X_w^{DC} = 1 ppm and one in which X_w^{DC} = 100 ppm. In both cases r = 1.0 and X_w^{EC} = 400 ppm. The case with more water in DC predicts lower I_R everywhere along the ridge. Also, increasing the water content of DC increases the along-axis distance, Δy_{norm}, to normal ridge composition. Finally, ΔI_R is larger in the case with more water, but the difference between the peak I_R over the hotspot and the minimum I_R, decreases slightly with increasing water content.

Increasing water content of DC decreases I_R along the entire length of the ridge because the DC melting zone is thicker, and capable of producing more magma, which increases the relative DC contribution to pooled magma. Comparing normal-ridge composition between the two cases illustrates that the difference is mostly independent of dynamic effects. The along-axis distance to normal ridge compositions increases with water content because the plume spreads farther along the ridge axis (Fig. 4.4b). In the case with more water in DC, viscosity is less sensitive to EC melting (and dehydration) than in the case with less water. The effective thickness of the lithosphere is thinner in the case with more water, and shallow spreading of the plume increases. ΔI_R increases with water because the difference in vertical velocity at the bases of the two melting zones increases; this, however, is not a general prediction. A more general prediction is that the

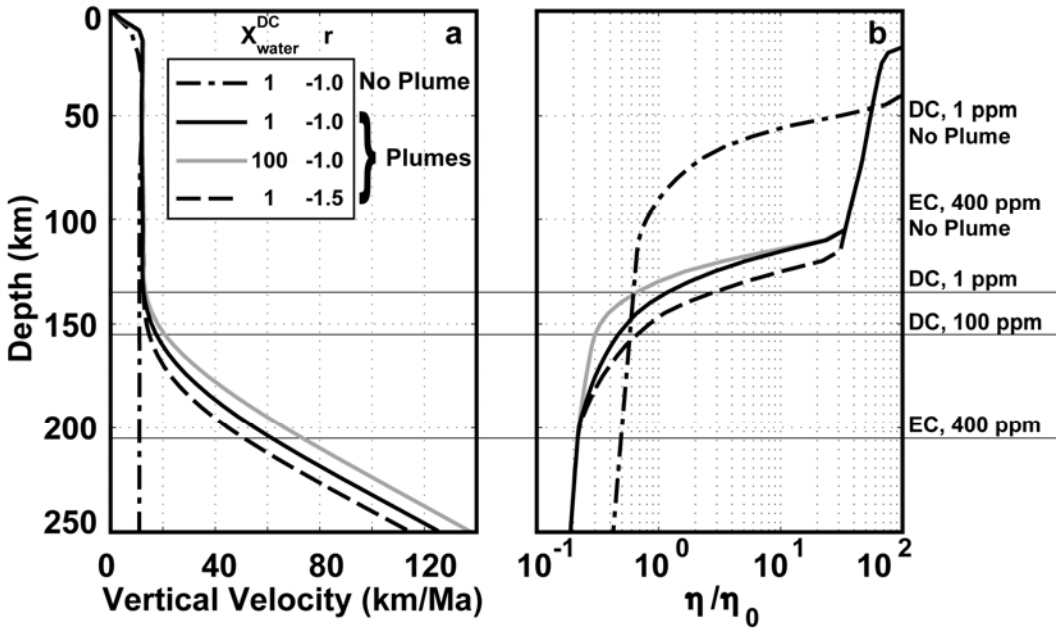

Figure 4.4 Vertical velocity and viscosity in simulations with different water-dependence and water content. (a) Vertical velocity versus depth in the upper 250 km of the model, and at the plume center ((*x*,*y*) = (0,0)) for the same simulations (plotted with the same line styles) as in Figure 4.3. (b) Viscosity normalized by reference viscosity for the simulations in (a) and Figure 4.3. Horizontal lines represent solidi depths, above which extent of partial melting (*F*) is greater than zero. From bottom to top, the solidi are those for EC with 400 ppm water, DC with 100 ppm water, and DC with 1 ppm water in simulations with a 200 K plume thermal anomaly. The solidi of EC with 400 ppm water and the DC with 1 ppm plot at shallower depths for a simulation with no plume.

difference between I_R over the hotspot and the minimum I_R decreases with increasing water content because adding water to DC tends to decrease the range in geochemical variations. The range decreases because as water is added to DC, any difference (i.e., shape, thickness, melting rate, extent of melting) between the melting zones of the two components is decreased, thus decreasing the sensitivity of composition to the mantle dynamics. Clearly if $X_w^{DC} = X_w^{EC}$ in these simulations, the composition of pooled magma would be a constant, and I_R would be equal to the mass fraction of EC in the initial solid mantle.

Note that because reference viscosity is independent of initial water content in the treatment above, the initial mantle has the same viscosity below the EC melting zone in all simulations. In reality, the case with lower X_w^{DC} would likely be more viscous at any depth because the bulk mantle initially has less water. Considering this more realistic behavior would amplify the predictions discussed in this section because decreasing reference viscosity decreases the velocity of the upwelling plume before any additional effects of dehydration occur, as illustrated in the next section.

4.3.4 Effects of Rayleigh number on ridge composition

In the present model, *Ra* defines reference viscosity η_o and controls the relative buoyancy of the thermal anomaly, both of which are poorly constrained. Increasing Rayleigh number decreases the reference viscosity and increases vertical velocity for a given temperature and density anomaly. To minimize differences in the thermal buoyancy flux (which is proportional to volume flux) between experiments of different *Ra*, we also change radius of the plume, r_{plume}. As in Chapter 3, r_{plume} defines the radius at which the thermal anomaly is T_{plume}/e, where T_{plume} is the temperature at the center of the anomaly. In the different simulations $Ra = 6.5 \times 10^5$, 3.3×10^5, 1.7×10^5, and 2.6×10^4; the corresponding viscosities are $\eta_o = 1.7 \times 10^{20}$ Pa·s, 3.3×10^{20} Pa·s, 6.3×10^{20} Pa·s, and 4.1×10^{21} Pa·s, and corresponding plume radii are r_{plume} = 89 km, 106 km, 125 km, and 200 km. We also include a case with $Ra = 6.5 \times 10^5$, but without a plume. Figure 4.5 shows that maximum crust thickness, ΔI_R, and long-wavelength width, Δy_{norm}, all increase with increasing *Ra*. The minimum value of I_R, and its location along the axis (Δy_{min}), is approximately preserved over this range of *Ra*.

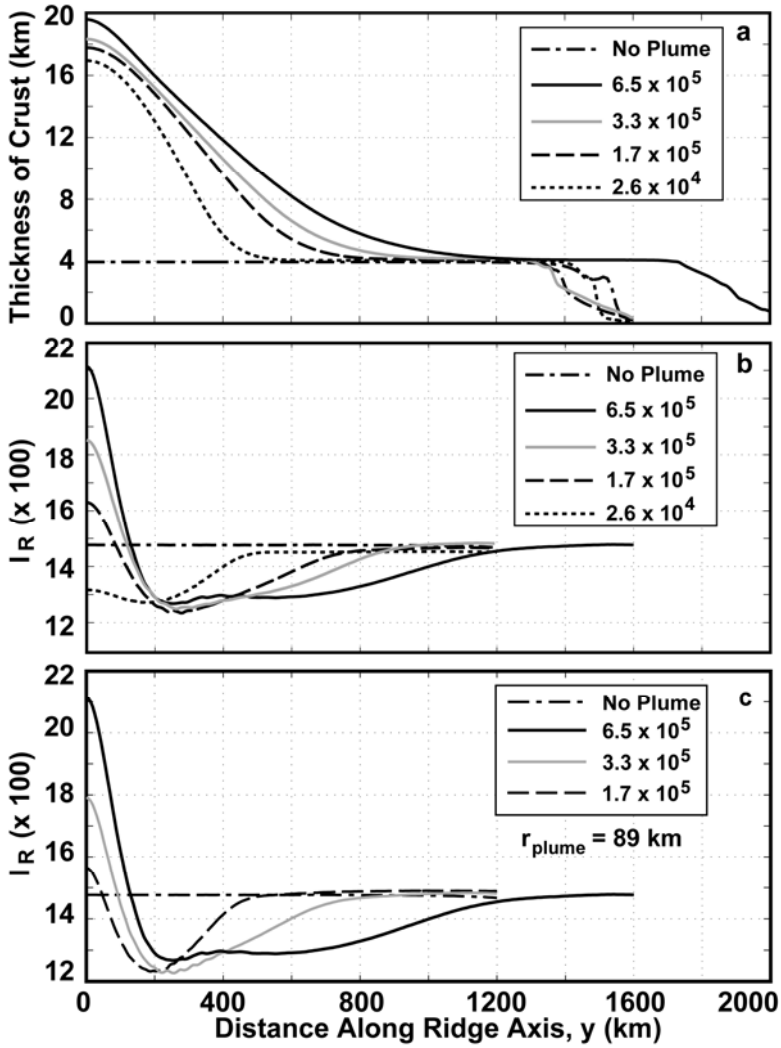

Figure 4.5 Crust and composition in simulations with different Rayleigh number. (a) Crustal thickness for simulations with different Ra and r_{plume}. The models have Ra = 6.5 x 10^5 (η_o = 1.65 x 10^{20} Pa·s, solid black line), 3.3 x 10^5 (η_o = 3.3 x 10^{20} Pa·s, solid gray line), 1.7 x 10^5 (η_o = 6.3 x 10^{20} Pa·s, dashed black line), and 2.6 x 10^4 (η_o = 4.1 x 10^{21} Pa·s, dotted black line); the corresponding r_{plume} = 89 km, 106 km, 125 km, 200 km. We also include a case with Ra = 6.5 x 10^5 (dash dotted black line) but with no plume. The model space of the simulation with a plume in which Ra = 6.5 x 10^5 extends an extra 400 km along the ridge axis. (b) EC fraction (I_R) for the same simulations as in (a). (c) EC fraction (I_R) for simulations with the same r_{plume} = 89 km, and with Ra = 6.5 x 10^5 (solid black line), 3.3 x 10^5 (solid gray line), and 1.7 x 10^5 (dashed black line). The case with no plume (black dash-dotted) is the same as that shown in (a).

Thickness of crust (h_c) over the center of the hotspot increases with Ra because vertical velocity in the plume significantly increases. ΔI_R increases with Ra also because vertical velocity increases much more near the base of the EC melting zone than near the

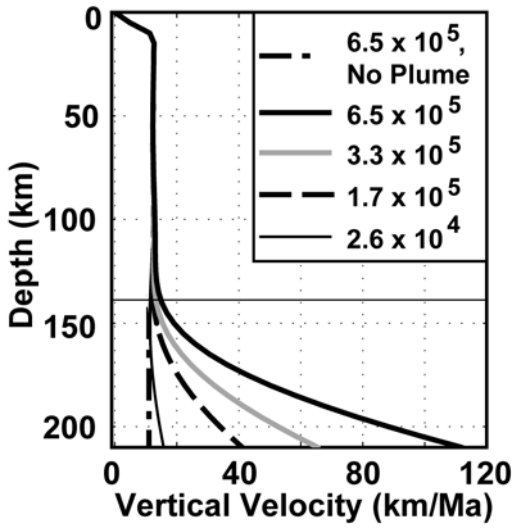

Figure 4.6 Vertical velocity in simulations with different Rayleigh numbers. (a) Vertical velocity versus depth in the upper 210 km of the model, and at the plume center ($(x,y) = (0,0)$) for the same simulations (plotted with the same line styles) as in Figures 4.5a and 4.b. The base of the EC melting zone at this position is 210 km, and the horizontal line shows the base of the DC melting zone, 135 km.

base of the DC melting zone. Dehydration above the base of the EC melting zone stiffens the mantle so that velocity at the base of the DC melting zone is negligibly different with increasing *Ra* compared to the increase at the base of the EC melting zone with increasing *Ra* (Figure 4.6). Thus the melting rate of DC is unaffected, while the melting rate of EC increases greatly, producing more total magma volume with greater EC fraction. Interestingly, in the case with $Ra = 2.6 \times 10^4$, plume material rises nearly passively, and we predict a negative geochemical anomaly above the center of the hotspot relative to the normal ridge and a thicker crust. This case illustrates a scenario in which the crustal thickness anomaly is positive (thicker than normal) but the geochemical anomaly is negative (a lower EC contribution than normal). The increase in Δy_{norm} with *Ra* is caused by the less viscous plume expanding farther along the axis. The distance to normal-ridge magma production and composition is closely related to the total width that the plume spreads along-axis, the plume "waist width" [*Ribe et al.*, 1995; *Feighner and*

Richards, 1995]. Waist width scales with the square root of volume flux, which is sensitive to both *Ra* and r_{plume}.

To remove the possible effects of r_{plume} on the location Δy_{min} and magnitude of minimum I_R along the axis, we also examine model simulations with different *Ra* (6.5 x 10^5, 3.3 x 10^5, and 1.7 x 10^5) but the same r_{plume} (89 km) (Figure 4.5c). Both the minimum EC fraction and its distance Δy_{min} increase slightly with *Ra.*

4.3.5 Effects of plume radius on ridge composition

We next examine how changing r_{plume} with a constant *Ra* (3.3 x 10^5) influences the surface observables. In the different simulations, r_{plume} is 75 km, 89 km, 106 km, 125 km, and 200 km, which spans the range of radii previous authors have reported for Iceland [e.g., *Schilling*, 1991; *Ribe and Christensen*, 1995; *Ito et al.*, 1996; *Wolfe et al.*, 1997; *Foulger et al.*, 2000; *Hung et al.*, 2004]. Figures 4.7a and 4.7b show the thickness of crust and composition along the axis for the simulations with different r_{plume}. Increasing r_{plume} results in greater crustal thickness over the plume, greater ΔI_R, greater distance to normal-ridge crust thickness and composition, Δy_{norm}, higher minimum I_R, and a wider high-EC anomaly, Δy_{min}. .

Crustal thickness (h_c) and I_R are greater over the center of the hotspot because a wider plume creates a wider zone of excess melting, and (4.9) and (4.10) are sensitive to the widths of melting zones. Figure 4.7c shows vertical velocity beneath the ridge (x = 0) at depths near the base of the EC (200 km) and DC (145 km) melting zones for simulations

with r_{plume} = 200 km and 75 km. The maximum vertical velocity at z = 200 km decreases with increasing r_{plume} because greater plume radii result in thicker layers of

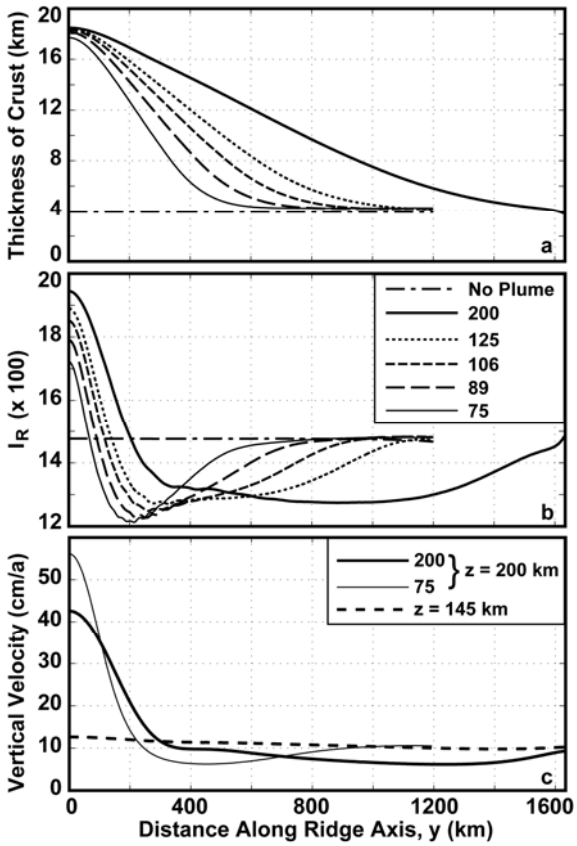

Figure 4.7 Crust and composition in simulations with different plume radii. (a) Crustal thickness for simulations with different r_{plume} and the same Ra. In the simulations Ra = 3.3 x 10^5 and r_{plume} = 75 km (thin solid line), 89 km (long-dashed line), 106 km (short-dashed line), 125 km (dotted line), and 200 km (thick solid line). We also include a case with no plume (dash-dotted line). The model space of the simulation in which r_{plume} = 200 km extends an extra 400 km along the ridge axis. Artifacts of the side boundary conditions exist but are not shown. (b) EC fraction (I_R) for the same simulations as in (a). (c) Vertical velocity below the ridge axis (i.e., x = 0) at a depth of z = 200 km for the simulations in (a) and (b) with r_{plume} = 75 km (thin, solid line) and 200 km (thick, solid line). Vertical velocity at a depth of z =145 km (dashed line) is approximately the same for the two simulations. The depths of z = 200 km and 145 km are near the bases of the EC and DC melting zones at the hot plume center (i.e., x = 0, y = 0), respectively.

ponding plume material, which causes streamlines to tilt towards the horizontal dimensions at this depth. This streamline tilting tends to decrease the EC fraction and thickness of crust in simulations with larger r_{plume}. A competing effect, however, is that

the width of rapid plume upwelling increases with r_{plume}, and this tends to increase EC fraction and thickness of crust in simulations with larger r_{plume} because of the horizontal integral in (4.9) and (4.10). This second effect is clearly the dominant, as EC fraction and crustal thickness generally increase with increasing r_{plume} (Fig. 4.7).

The total, long-wavelength width of plume influence (Δy_{norm}) is controlled by the increase in plume waist width with volume flux as r_{plume} increases. Interestingly, the distance to the minimum EC fraction increases strongly with r_{plume} (Fig. 4.7c); this distance is controlled by the along-axis width of the velocity anomaly associated with plume upwelling, which increases with r_{plume}. Thus, the width of the short-wavelength anomaly (Δy_{min}), which will be important in comparing the present model to observations, is more sensitive to r_{plume} than it is to Ra.

4.3.6 Widths and magnitudes of predicted geochemical anomalies

Figure 4.8 summarizes the dependence of the three key measurements of the predicted geochemical anomalies (Δy_{norm}, Δy_{min}, and ΔI_R) on plume buoyancy flux, B. Buoyancy flux is an important quantity that may be estimated with observations and is widely used to characterize hotspots [e.g., *Sleep*, 1990]. We report results here for models in which r = 1.0, and DC water content is 1 ppm.

Theory predicts that distance to normal-ridge composition, Δy_{norm}, increases with the square root of buoyancy flux ($B^{1/2}$) [*Ribe et al.*, 1995; *Ito et al.*, 1996; *Albers and Christensen*, 2001], and in these simulations we find that a linear fit to this relationship has a correlation coefficient >0.99 (Figure 4.8a). An interesting prediction is that for cases with realistic buoyancy (0.5 to 3.5 Mg/s) the distance to normal-ridge composition

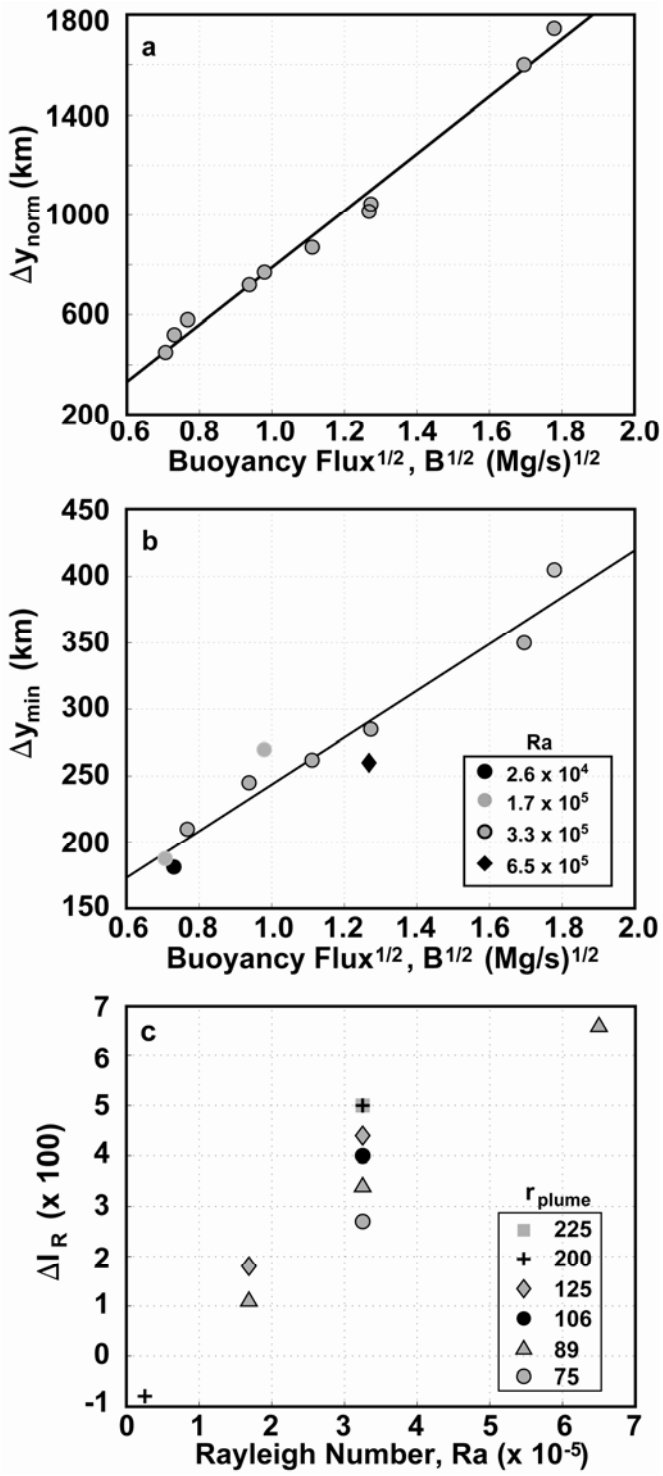

Figure 4.8 Width and magnitude of geochemical anomalies. (a) Distance to normal ridge (Δy_{norm}; see Figure 4.3b) versus the square root of thermal buoyancy flux ($B^{1/2}$). The figure includes simulations with a range of *Ra* from 2.6 x 10^4 to 6.5 x 10^5 and a range of r_{plume} from 75 km to 225 km, and only includes models in which r = 1.0 and DC water content is 1 ppm. This distance is also referred to as the "long-wavelength geochemical anomaly". A linear fit to the data (black line) with correlation coefficient >0.99 also is shown. (b) Distance to the minimum EC fraction (Δy_{min}; see Figure 4.3b) versus $B^{1/2}$ for the same simulations as in (a). We measure Δy_{min} as the distance to the local minimum that is closest to the hotspot center, which in most cases is also the global minimum. This distance is useful to define the width of the "short-wavelength geochemical anomaly". We indicate the *Ra* in the simulation: 6.5 x 10^5 (black diamond), 3.3 x 10^5 (gray circles with black outline), 1.7 x 10^5 (solid gray circles), and 2.6 x 10^4 (solid black circle). A linear fit to the data (black line) with correlation coefficient >0.96 is shown. (c) Magnitude of the geochemical anomaly (relative to normal-ridge composition of 0.15) at the center of the hotspot (ΔI_R; see Figure 4.3b) versus Rayleigh number *Ra*. We also indicate r_{plume} in the simulation: 75 km (gray circle), 89 km (triangles), 106 km (black circle), 125 km (diamonds), 200 km (black crosses), and 225 km (square).

ranges between ~450 km and 1750 km, meaning that plumes may influence ridges over very long distances.

The width of the high-EC fraction, short-wavelength anomaly Δy_{min} also increases linearly with $B^{1/2}$. It is clear in the comparisons of simulations above that Δy_{min} is not very sensitive to Ra. Examining the trend for simulations in which r_{plume} changes with fixed Ra (Ra = 3.25 x 10^5) reveals a dependence on r_{plume} that is independent of Ra. Finally, the magnitude of the geochemical anomaly over the center of the hotspot, ΔI_R, has a strong dependence on Ra and a relatively weak dependence on r_{plume} (Figure 4.8c).

4.4 Comparisons with Iceland

Now that we have shown how predicted geochemical anomalies depend on mantle conditions, we explore which aspects of observed geochemical anomalies the model can explain. Here we compare model prediction of $^{87}Sr/^{86}Sr$, crust thickness, and La/Sm (relative to primitive mantle [*Sun an McDonough*, 1989]) with observations for Iceland and the surrounding Mid-Atlantic Ridge (MAR). We assume the plume is centered on Bárdarbunga Volcano [as in *Ito et al.*, 1999], which is consistent with the mantle seismic structure [*Wolfe et al.*, 1997]. In order to compare the simple geometry in the modeled ridge (straight and perpendicular to plate motion) to the geometry of the MAR near Iceland, we adjust the position of samples before measuring distance from Bárdarbunga. We project data collected south of Bárdarbunga and north of 55 ° N to a line that passes through Bárdarbunga with an azimuth of 61 °; this line is nearly parallel to the Reykjanes Ridge. For the samples north of Bárdarbunga, positions are projected (east or west) to the

nearest ridge segment. We then compute the total distance between Bárdarbunga and projected sample locations.

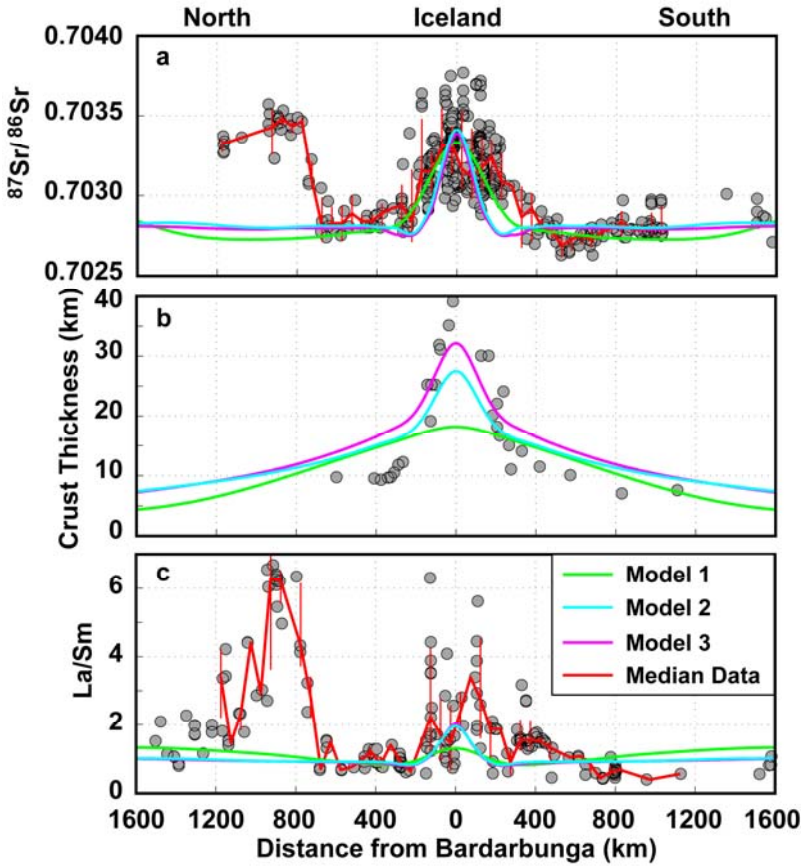

Figure 4.9 Predicted and observed composition and crustal thickness at and near Iceland. (a) Observed $^{87}Sr/^{86}Sr$ (gray circles) at Iceland (data from GEOROC and EarthRef databases; http://georoc.mpch-mainz.gwdg.de and http://earthchem.org). The center of the plume is assumed to be Bárdarbunga Volcano and distances are computed as explained in the text. The median of data grouped in 50 km intervals is also shown (red line) with the standard deviation about the mean for each interval (red bars). Reference model predictions are also plotted: "Model 1" (green line), "Model 2" (cyan line) and "Model 3" (magenta line) are described in the text and in Tables 4.1-4.3. (b) Estimates of crust thickness at Iceland and predicted thickness for the same simulations as in (a). Data (gray circles) are digitized from *Hooft et al.* [2006]. (c) Observed La/Sm (relative to primitive mantle [*Sun and McDonough*, 1989]) in tholeiites sampled near Iceland (dataset shown in *Ito et al.*, [2003] from the GEOROC database http://georoc.mpch-mainz.gwdg.de). Median values (red line) and standard deviations about the mean (red bars) are computed as described for (a). Model predictions are also shown as in (a).

The results of these projections are shown in Figure 4.9a and are much like what has been shown in prior studies [*e.g.*, *Schilling*, 1973, *Ito et al.*, 1999; *Hanan et al.*, 2000]

($^{87}Sr/^{86}Sr$ data from GEOROC, http://georoc.mpch-mainz.gwdg.de, and EarthRef, http://earthchem.org, databases). Both the running median values and the standard deviations (both based on populations in 50 km bins of distance from Bárdarbunga) of $^{87}Sr/^{86}Sr$ and La/Sm peak in central Iceland. From this peak, $^{87}Sr/^{86}Sr$ and La/Sm decrease along the MAR, reaching low values at distances of ~300 km to the north and ~500 km to the south. Farther north, another peak in $^{87}Sr/^{86}Sr$ and La/Sm is evident near Jan Mayen Island, which may represent a separate hotspot from Iceland [e.g., *Schilling et al.*, 1999]. There also is a long wavelength (~10^3 km) increase in $^{87}Sr/^{86}Sr$ and La/Sm northward that may exist independently of any influence by Iceland and Jan Mayen [*Hanan et al.*, 2000].

Three reference model runs are compared to the data (Fig 4.9). The first model, "Model 1", is most similar to the simulations above: r_{plume} = 225 km, Ra = 3.25 x 10^5, T_{plume} = 200 K, μ_{lim} = 100, X_w^{DC} = 1 ppm, X_w^{EC} = 400 ppm, I^{DC} = 0.7016 and I^{EC} = 0.7105 (see Tables 4.1-4.3 reference model parameters). The other two reference models (Models 2 and 3) are meant to depict parameters closer to previously published estimates related to Iceland, with μ_{lim} = 25, X_w^{DC} = 100 ppm, and X_w^{EC} = 400 ppm [*Hirth and Kohlstedt*, 1996; *Hirth and Kohlstedt*, 2003], r_{plume} = 100 km [*Wolfe et al.*, 1997; *Allen et al.*, 2002; *Hung et al.*, 2004], I^{DC} = 0.7019, and I^{EC} = 0.7097. "Model 2" has Ra = 1.3 x 10^6 and T_{plume} = 200 K, whereas "Model 3" has Ra = 1.0 x 10^6 and T_{plume} = 225 K. We note that in the reference models, the $^{87}Sr/^{86}Sr$ is higher than nearly all oceanic basalts, but is comparable to a few samples found at Samoa [*Jackson et al.*, 2007]; although, there is no evidence for a Samoan-type end-member melting beneath Iceland. In the case of

Model 1, the width of the simulation's short-wavelength, high $^{87}Sr/^{86}Sr$ anomaly is ~800 km, which closely matches that (~800 km) of medians along the MAR. The width of the high $^{87}Sr/^{86}Sr$ anomaly in Model 2 and Model 3 is ~500 km, which is about 60% of that observed. In all three reference models, the long-wavelength geochemical anomaly with relatively low $^{87}Sr/^{86}Sr$ extends to >1700 km, and the steady composition within this anomaly captures the steady, lower composition of the Kolbeinsey and Reykjanes ridges to the north and south of Iceland. The reference models do not predict the Jan Mayen anomaly. We find that it is easy to reproduce the relative magnitude of the high $^{87}Sr/^{86}Sr$ anomaly at Iceland by adjusting the $^{87}Sr/^{86}Sr$ of EC and DC. In the cases we have tested, including the three reference models shown here, the width of the high $^{87}Sr/^{86}Sr$ anomaly near Iceland may only be reproduced with a narrow range of r_{plume}, regardless of other parameters.

Estimates of the thickness of crust near Iceland [from *Hooft et al.*, 2006], along with the predicted thickness of crust are also shown (Figure 4.9b). The measured crustal thickness increases within ~400 km of Bárdarbunga from about 10 km to ~40 km thick. All three reference models predict a smaller maximum thickness at the hotspot center than measurements at Iceland, and also predict the thick-crust anomaly is wider than at Iceland. Model 3 makes the best prediction of maximum Iceland thickness (~32 km); Model 1 (~18 km) and Model 2 (~27) predict considerably thinner crust at Iceland.

La/Sm data in tholeiitic samples (dataset shown in *Ito et al.*, [2003] from the GEOROC database http://georoc.mpch-mainz.gwdg.de) are plotted with model prediction for comparison (Fig 4.9c). Unlike isotope ratios, La/Sm is affected by the extent of partial

melting in pooled magmas; a higher extent of partial melting tends to decrease La/Sm. *Schilling et al.* [1999] employed the method of *Klein and Langmuir* [1987] to infer that the mean extent of partial melting increases toward Iceland, and subsequently interpreted the observed increase in La/Sm toward Iceland as being caused by an increasing contribution from a component with high La/Sm [*Schilling*, 1973; 1991; *Schilling et al.*, 1999]. The reference models have a La/Sm of 3.25 in EC and 0.1 in DC with EC having 30 times more La than DC (see Ch. 3, Eq. 3.12 and Table 4.2). Also, in calculating bulk partition coefficients, we account for a garnet-spinel transition at 90 km depth, and pressure-dependent exhaustion of clinopyroxene as defined by *Katz et al.* [2003] (see Table 4.3; bulk partition coefficients are computed using the mineral modes and partition coefficients of *Ito and Mahoney* [2005a] and references therein).

In Model 1, a local maximum in La/Sm is predicted to occur at the center of the hotspot. Increasing the La/Sm in EC increases high La/Sm near the hotspot rendering it more comparable to observed values; however, this increase causes the predicted La/Sm to be too high to match the observed normal ridge compositions. In Model 2 and Model 3 the maximum at the hotspot center is higher than normal-ridge La/Sm. Models 2 and 3 therefore successfully predict the relatively high La/Sm at Iceland, and the lower La/Sm away from Iceland. In all three reference models, the width of the high La/Sm is ~400 km, which is much narrower than ~800 km observed in running medians along the MAR near Iceland.

Among all the simulations we have tested, including the three reference models shown here, we have not found a single simulation that adequately matches all of the

above observations for Iceland. Of the three, Model 3 is favored for two main reasons. First, the radius of the model plume is more consistent than that of Model 1 in terms of the width of the mantle seismic anomaly beneath Iceland [e.g., *Wolfe et al.*, 1997; *Foulger et al.*, 2000; *Allen et al.,* 2002; *Hung et al.*, 2004]. Second, the predicted crustal thicknesses better match those of Iceland than predictions from Models 1 or 2. The remaining key discrepancy is that the width of the short-wavelength, high $^{87}Sr/^{86}Sr$ and La/Sm anomaly is about 60% of the observed width. We therefore must consider the possibility that the material rising in the mantle plume is compositionally distinct from that of the ambient mantle. The compositional distinction could take three forms: (1) moderate zoning of the mass fraction of mantle components, φ^l, in the upper mantle, such that φ^{DC} decreases in the center of the plume, (2) the initial Sr content of DC decreases in the center of the plume, and/or (3) the $^{87}Sr/^{86}Sr$ of DC increases in the center of the plume.

In the final model for the Iceland-MAR system, we simulate a plume that is compositionally zoned according to possibility (1). We assume that the material that is rising in the center of the plume that is hotter than 1460°C (excess of 160°C) is more "enriched" by having 3% more EC and 3% less DC (i.e., φ^{EC} = 13% and φ^{DC} = 87%) than the references case. We then use the 1460°C isosurface to track this enriched plume material as it flows along axis and melts. All mantle cooler than 1460°C is assumed to have the reference composition of φ^{EC} = 10% and φ^{DC} = 90%. Because of cooling due to melting, decompression, and conduction, the volume of mantle that is enclosed by the 1460°C isosurface and actively melting is less than the actual volume of enriched plume material that is melting. Thus, using temperature to track the distribution of the enriched

plume material is an approximation that tends to under-predict $^{87}Sr/^{86}Sr$, but most significantly only between along-axis distances of y = 200 km and 400 km; therefore the overall shape of the anomaly is sufficiently accurate to illustrate the most prominent

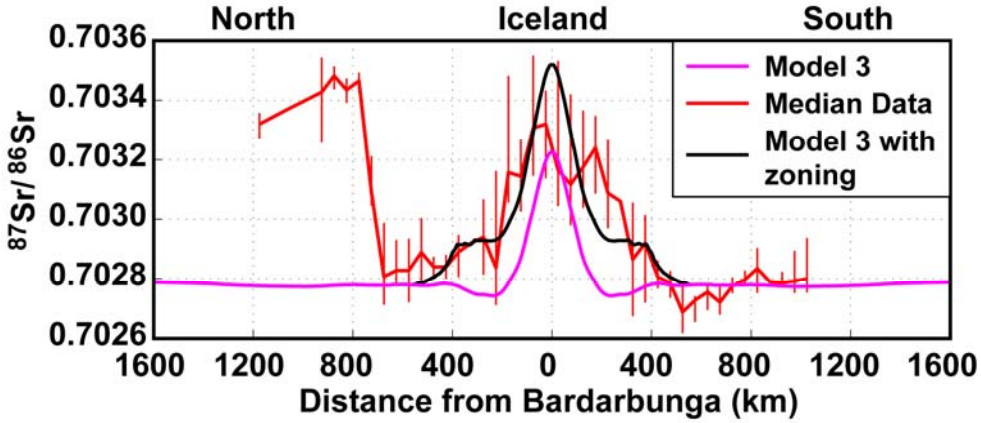

Figure 4.10 Prediction of $^{87}Sr/^{86}Sr$ with moderate compositional zoning in the plume. Median $^{87}Sr/^{86}Sr$ observed at Iceland (red line) and standard deviation about the mean for data grouped in 50 km intervals. Model 3 (cyan line) as in Figure 4.9 is plotted for reference. The black line is the Model 3 prediction, with 3% less DC by mass inside a temperature contour of 1460 ° C (excess temperature of 160 K). Approximately the same prediction as that illustrated by the black line is made if the Sr content of DC decreases by ~30%, or if $^{87}Sr/^{86}Sr$ of DC increases by 0.0002 inside the same temperature contour.

effects of such compositional zoning. The net result of this compositional zoning is to widen the predicted geochemical anomaly over the plume such that it more comparable to that centered on Iceland (Figure 4.10). Approximately the same result occurs if C_0^{DC} decreases ~30% (possibility (2)), or if I^{DC} increases from 0.7019 to 0.7021 (possibility (3)).

A mantle plume that delivers material that is relatively enriched in incompatible elements compared to the ambient Atlantic upper mantle is consistent with the inferences of prior studies. As mentioned earlier, several other studies hypothesize, that in addition to an enriched component in the plume, a depleted component exists that is distinct from

the ambient upper mantle [*Hemond et al., 1993; Kerr 1995; Kerr et al., 1995; Fitton et al., 1997; Chauvel and Hemond, 2000; Kempton et al. 2000; Skovgaard et al., 2001; Breddam, 2002; Fitton et al., 2003; Thirlwall et al., 2004; Kokfelt et al., 2006*]. An important result this work reveals is that the difference between the average composition of the plume and ambient upper mantle need only be subtle. For example, melting the central, more "enriched" plume material with higher $^{87}Sr/^{86}Sr$ under normal ridge conditions produces a composition of 0.70314, compared to the 0.70297 produced by melting the reference material. Both compositions fall close to within one standard deviation about the median seen in "normal" mid-ocean ridge basalts globally (i.e., 0.7020-0.7030) [*Ito and Mahoney*, 2005b; *Ito and van Keken*, 2007]. Thus, we predict that the source of Iceland is not very different from the typical source beneath ridges, other than the northern MAR. This result supports the possibility proposed by *Ito and Mahoney* [2005b, 2006] that the mantle need not be compositionally stratified to explain the compositional differences between the Earth's major hotspots and sections of mid-ocean ridges not influenced by hotspots. Further, this work supports the possibility that compositional heterogeneity exists primarily on a small scale ($\leq \sim 10^0$ km), as can result from vigorous convection and stirring.

4.5 Conclusions

We have tested the compositional consequences of melting a veined, ridge-centered mantle plume. Upper mantle dynamics cause geographic variations in the composition of magma erupted along the ridge. In the veined mantle hypothesis, along-axis variation in composition requires that one component (the more hydrous EC) begin melting deeper, and has different trace-element and isotope ratios. We predict that the dynamics of mantle

flow and melting associated with the plume upwelling causes a short-wavelength anomaly (<~400 km) with a relatively high contribution from EC surrounded by a long-wavelength anomaly (>~800 km) with a relatively low contribution from EC. The major requirement for the short-wavelength anomaly is that the lithosphere beneath the ridge is thicker than one that is solely created by plate cooling. Such an increase in the mechanical thickness is achieved in the present models by considering that viscosity increases with the dehydration of olivine in hydrous peridotite during progressive melting [*Hirth and Kohlstedt*, 1996; *Hirth and Kohlstedt*, 2003]. The long-wavelength anomaly is caused in part by plume spreading, which diminishes upwelling related to plate separation and transfers depleted material along the axis. We show that increasing the radius of the mantle plume, r_{plume}, the Raleigh number *Ra*, or both tends to increase the width of the short-wavelength, high EC anomaly and the width of the long-wavelength, low EC anomaly. Thermal buoyancy flux and volume flux of the plume depend on *Ra* and r_{plume}, and thus the widths of the long- and short-wavelength geochemical anomalies correlate with buoyancy flux. We find that the widths of the anomalies increase linearly with $B^{1/2}$, which is a well-established scale for the along-axis extent of the plume [*Ribe et al.*, 1995]. Finally, the magnitude of the high EC, short-wavelength anomaly also increases with buoyancy flux but is more sensitive to *Ra* than r_{plume}.

Three reference models address the $^{87}Sr/^{86}Sr$, La/Sm, and crustal thickness variation along the MAR near Iceland. All models capture the main observations of high $^{87}Sr/^{86}Sr$, La/Sm, and crustal thickness over Iceland, which gradually decrease over hundreds of kilometers away from Iceland, with low values >400km away from Iceland. One model (Model 1), with a broad plume (225 km), moderate *Ra* (6.5×10^5), moderate T_{plume} (200

K), and high viscosity increase due to dehydration (μ_{lim} = 100 times) predicts the width and height of the $^{87}Sr/^{86}Sr$ anomaly over Iceland, but does not predict the width and height of the crustal thickness anomaly. Another model, (Model 3) with a narrow plume (100 km), high *Ra* (10 x 10^5), high T_{plume} (225 K), and low viscosity increase due to dehydration (μ_{lim} = 25) better predicts the height of the crustal thickness anomaly, but predicts a narrower $^{87}Sr/^{86}Sr$ anomaly than that observed over Iceland. All three models under-predict the magnitude and wavelength of the observed La/Sm anomaly. An alternative presented is a case similar to Model 3, but in which the hottest interior of the rising plume is more "enriched" than the rest of the mantle by having either slightly more EC (13% compared to 10%), lower initial Sr content in DC (30% less), or higher $^{87}Sr/^{86}Sr$ in DC (0.7019 versus 0.7021). It is not surprising that some difference between the average composition of the mantle plume and ambient upper mantle exists, but the necessary difference between the plume and upper mantle in the model is well within normal mid-ocean ridge basalt compositions. Thus, the proposed plume composition is slightly different from northern MAR upper mantle, but not different from typical oceanic mantle sampled at ridges globally. Therefore, a mantle with large-scale stratification in composition is not necessary to explain observations near Iceland, and alternatively, the observations may be explained with upper-mantle dynamics and melting of a veined mantle.

Table 4.1 Parameters used and measured in reference models

Parameter	Model 1	Model 2	Model 3
Ra	6.5×10^5	1.0×10^6	1.3×10^6
η_o (Pa·s)	1.7×10^{20}	1.1×10^{20}	8.3×10^{20}
r_{plume} (km)	225 km	100 km	100 km
B (Mg/s)	3.16	1.4	1.4
r	1.0	1.0	1.0
μ_{lim}	100	25	25
X_w^{EC} (wt ppm)	400	400	400
X_w^{DC} (wt ppm)	1	100	100
I^{DC} ($^{87}Sr/^{86}Sr$)	0.7016	0.7019	0.7019
I^{EC} ($^{87}Sr/^{86}Sr$)	0.7105	0.7097	0.7097

Table 4.2 Compositional parameters of components in reference models

Parameter	DC	EC
La/Sm †	0.1	3.25
$[La]_0$ †	0.1	3.25
$[Sm]_0$ †	1.0	1.0, 1.0
† Normalized by primitive mantle composition [*Sun and McDonough*, 1989]		

Table 4.3 Bulk partition coefficients used in reference models

Conditions	La	Sm
z > 90 km, $F < F_{cpx\text{-}out}$	0.0068	0.7036
z < 90 km $F < F_{cpx\text{-}out}$	0.0092	0.0420
$F \geq F_{cpx\text{-}out}$	0.0029	0.0070
Mineral models and partition coefficients as in *Ito and Mahoney* [2005a]		

Chapter 5

Conclusions

5.1 General Conclusions

This work has tested the hypothesis that dynamics and variable melting of a mantle with small-scale (10^0 km) veins of heterogeneity can result in geographic and temporal trends in magma composition observed at hotspots. Moderate-scale geographic (10^2 km) and temporal (10^2 Ma) trends in composition arise simply from local trends in dynamics such as that associated with plume-lithosphere interaction, and variable melting related to differences in the petrology of mantle components. The second general conclusion is that the predicted trends capture many aspects of observed trends at real hotspots. These conclusions challenge previous notions that moderate-scale (10^2 km) heterogeneity in the mantle is necessary to explain observations at hotspots.

We have tested the hypothesis at two prominent tectonic settings where hotspots are observed: (1) at intraplate hotspots where plumes rise beneath oceanic lithosphere far from a tectonic boundary, and (2) at a ridge-centered hotspot, where a plume rises directly beneath an active mid-ocean ridge. At both tectonic settings, buoyantly driven flow in the mantle plume enhances the relative contribution of less-refractory components to the trace-element composition of pooled (accumulated) magma. Some observations at both intraplate and ridge-centered hotspots (e.g., difference between Kea and Loa subchains at Hawaii) require some inherent, moderate-scale heterogeneity in the bulk composition of the mantle source. However, our estimate of the magnitude of this moderate-scale heterogeneity in bulk composition is much smaller than previously

thought, and are comparable to variations in the source of normal mid-ocean ridge basalts (MORB) worldwide. Thus, large-scale layering in the mantle with strong compositional differences is not necessary to explain geochemical trends observed at hotspots.

5.2 Conclusions on Intraplate Hotspots

Chapters 2 and 3 explore hotspots formed by plumes rising beneath oceanic lithosphere with a model age between 25 Ma and 100 Ma. The work compared model predictions to observations at Hawaii, Samoa, and Réunion hotspots. One prediction is that plate motion tilts rising plumes, shifting the centers of melting zones of more refractory components downstream from those of the less refractory components. Thus, as a volcano passes over an intraplate hotspot, the predicted contribution from a less refractory component to the magma increases with volcano growth. If more refractory components are relatively depleted in incompatible elements, the predicted average composition of volcanoes evolves from enriched to depleted with the age of the volcano. The relative change in average composition increases with greater tilting of streamlines in the plume, which in turn increases with plate age and plate velocity, and decreases with thermal buoyancy flux. This general prediction can explain observations of compositional evolution of volcanoes at Hawaii and Reunion, and general trends in the Hawaiian and Samoan chains.

In some simulations, volcanoes that pass off-axis from the plume center may have relatively depleted shield stages compared to volcanoes that pass on-axis. This is because in these simulations the most buoyant upwelling in the plume center causes a local high in the contribution from the less refractory, enriched component (EC). The effect of the

local high in EC may explain the difference in composition versus stratigraphic depth between (Mauna) Loa and (Mauna) Kea subchains at Hawaii, if they represent on-axis and off-axis chains, respectively. None of simulations tested, however, had a local EC anomaly over the plume stem that could explain differences between the Loa and Kea illustrated in $^{208}Pb/^{204}Pb$ versus $^{206}Pb/^{204}Pb$ space.

One possibility for the discrepancy is that the mass fraction of components is different beneath Loa and Kea subchains. In simulations with three components, we find that the composition of the shield stage plots on a pseudo-binary mixing line, which points between a mixture of the two least refractory components, and the average composition of the source. Thus, simulations with different mass fractions of the two least-refractory components lead to sub-parallel mixing lines in $^{208}Pb/^{204}Pb$ versus $^{206}Pb/^{204}Pb$ space, which capture the difference between Loa and Kea subchains.

Finally, the scatter in data observed over short timescales (10^{-5} Ma) at intraplate hotspots may result from either non-uniform heterogeneity, spatially and temporally variable sampling of different components, incomplete magma mixing, or a combination of all three. The present model attributes trends in average composition to melting a veined mantle under the influence of plume-lithosphere interaction, and attributes scatter about the average to variability in the source.

5.3 Conclusions on Ridge-Centered Hotspots

Chapter 4 analyzed hotspots formed by plumes rising beneath a mid-ocean ridge. Also, reference model predictions were compared to observations of crustal thickness and composition at Iceland. Along the ridge axis, a short-wavelength (<400 km) anomaly

with a relatively high contribution from the enriched component ("EC") occurs over the hotspot in simulations that consider the effects of dehydration of the mantle on viscosity. Dehydration occurs with progressive melting, and increases the effective thickness of the lithosphere, which greatly enhances deep upwelling and melting rate in the EC melting zone relative to that in the depleted component's ("DC"). This enhanced upwelling is localized near the plume stem; consequently the short-wavelength high in EC contribution is localized above the plume stem. Surrounding the short-wavelength anomaly (with high EC contribution) is a long-wavelength anomaly (>800 km) with relatively low EC contribution, caused by diminished, plate-driven upwelling and the transfer of depleted material along the ridge-axis. Increasing the width of the plume radius (r_{plume}), the Rayleigh number (Ra), or both, increases the width of the short and long-wavelength anomalies. Fluid mechanics theory predicts that the along-axis extent of plume material increases with the square root of volume flux. We find that both the short- and long-wavelength anomalies increase linearly with the square root of thermal buoyancy flux ($B^{1/2}$), a measurable parameter in real systems that is proportional to volume flux. Finally, the magnitude of the short-wavelength anomaly increases with buoyancy flux, and with a stronger dependence on Ra than r_{plume}.

Reference models in which EC has high $^{87}Sr/^{86}Sr$ and La/Sm predict the observed high in $^{87}Sr/^{86}Sr$ and La/Sm over Iceland relative to the surrounding Mid-Atlantic Ridge (MAR). One reference model with a wide plume radius (225 km), moderate Ra (6.5 x 10^5) and reference viscosity (1.65 x 10^{20} Pa·s), and moderate plume temperature anomaly (200 K) predicts the width of the $^{87}Sr/^{86}Sr$ anomaly, but under-predicts the crustal thickness at Iceland. Another model with a narrower plume radius (100 km), higher Ra

(6.5 x 10^5), lower reference viscosity (1.0 x 10^{20} Pa·s), and hotter thermal anomaly (225 K) better predicts the thickness of crust at Iceland, but under-predicts the width of the $^{87}Sr/^{86}Sr$ anomaly. Also, all simulations under-predict the width of the high La/Sm anomaly observed over Iceland. We therefore favor a model with some radial zoning of material, such that the average composition of the innermost portion of the plume is different from that of the upper mantle. This form of large-scale heterogeneity is typically hypothesized for the Iceland-MAR source. We included a simulation that approximates this form of large-scale heterogeneity by changing the average mantle composition inside a plume temperature contour. The width of the Iceland $^{87}Sr/^{86}Sr$ anomaly is predicted with a 100 km plume radius if the mass fraction of DC is 3% lower inside the center of the plume. Alternatively, the center of the plume may have 30% lower initial Sr content of DC, or $^{87}Sr/^{86}Sr$ in DC is higher (0.7099 versus 0.7097). These differences between the inner plume and ambient upper mantle are within the standard deviation of MORB data worldwide. Whereas the model requires the inner part of the Iceland plume to differ from ambient MAR upper mantle, it does not require either the inner or outer plume to differ from the typical MORB source. Thus, some observations along the northern MAR may be explained with dynamics and small-scale heterogeneity in the absence of compositional stratification in the mantle.

References

Abouchami, W., J. G. Galer and A. W. Hofmann (2000), High precision lead isotope systematics of lavas from the Hawaiian Scientific Drilling Project, *Chemical Geology 169*, 187-209

Abouchami, W., A. W. Hofmann, J. G. Galer, F. A. Frey, J. Eisele and M. Feigenson (2005), Lead isotopes reveal bilateral asymmetry and vertical continuity in the Hawaiian mantle plume, *Nature 434*

Albers, M. and U. R. Christensen (2001), Channeling of plume flow beneath mid-ocean ridges, *Earth and Planetary Science Letters 187*, 207-220

Allègre, C. J. (1982), Chemical geodynamics, *Tectonophysics 81*, 109-132

Allen, R. M., G. Nolet, W. J. Morgan, K. Vogfjord, B. H. Bergsson, P. Erlendsson, G. R. Foulger, S. Jakobsdottir, B. R. Julian, M. J. Pritchard, S. Ragnarsson and R. Stefansson (2002), Imaging the mantle beneath Iceland using integrated seismological techniques, *Journal of Geophysical Research 107*, 2325 doi:10.1029/2001JB000595

Asimow, P. D., J. E. Dixon and C. H. Langmuir (2004), A hydrous melting and fractionation model for mid-ocean ridge basalts: Application to the Mid-Atlantic Ridge near the Azores, *Geochem. Geophys. Geosys. 5* doi:10.1029/2003GC000568

Ballmer, M. D., J. van Hunen, G. Ito, P. J. Tackley and T. A. Bianco (2007), Non-hotspot volcano chains originating from small-scale sublithospheric convection, *Geophysical Research Letters 34* doi:10.1029/2007GL031636

Bianco, T. A., G. Ito, J. M. Becker and M. O. Garcia (2005), Secondary Hawaiian volcanism formed by flexural arch decompression, *Geochemistry Geophysics Geosystems 6* doi:10.1029/2005GC000945

Blichert-Toft, J., D. Weis, C. Mearschalk, A. Agranier and F. Albarède (2003), Hawaiian hot spot dynamics as inferred from the Hf and Pb isotope evolution of Mauna Kea volcano, *Geochem. Geophys. Geosys. 4* doi:10.1029/2002GC000340

Bosch, D., J. Blichert-Toft, F. Moynier, B. K. Nelson, P. Telouk, P.-Y. Gillot and F. Albarède (2008), Pb, Hf, and Nd isotope compositions of the two Reunion volcanoes (Indian Ocean): A tale of two small-scale mantle "blobs"?, *Earth and Planetary Science Letters 265*, 748-768 doi:10.1016/j.epsl.2007.11.018

Breddam, K. (2002), Kistufell: Primitive melting from Iceland mantle plume, *Journal of Petrology 43*, 345-373

Breddam, K., M. D. Kurz and M. Storey (2000), Mapping out the conduit of the Iceland mantle plume with helium isotopes, *Earth and Planetary Science Letters 176*, 45-55 doi:10.1016/S0012-821X(99)00313-1

Bryce, J. G., D. J. DePaolo and J. C. Lassiter (2005), Geochemical structure of the Hawaiian plume: Sr, Nd, and Os isotopes in the 2.8 km HSDP-2 section of Mauna Kea volcano, *Geochemistry Geophysics Geosystems 6* doi:10.1029/2004GC000809

Chauvel, C. and C. Hemond (2000), Melting of a complete section of recycled oceanic crust: Trace element and Pb evidence from Iceland, *Geochem. Geophys. Geosys. 1* doi:10.1029/1999GC000002

Chen, C.-Y. and F. A. Frey (1985), Trace element and isotopic geochemistry of lavas

from Haleakala volcano, East Maui, Hawaii: Implications for the origin of Hawaiian basalts, *Journal of Geophysical Research 90*, 8743-8768

Cohen, R. S. and R. K. O'Nions (1982), Identification of recycled continental material in the mantle from Sr, Nd, and Pb isotope investigations, *Earth and Planetary Science Letters 61*, 73-84

Darbyshire, R., I. T. Bjarnason, R. S. White and O. Flovenz (1998), Crustal structure above the Iceland mantle plume imaged by the ICEMELT refraction profile, *Geophys. J. Int. 13*, 1131-1149

Davis, E. E. and C. R. B. Lister (1974), Fundamentals of ridge crest topography, *Earth and Planetary Science Letters 21*, 405-413 doi:10.1016/0012-821X(74)90180-0

DePaolo, D. J., J. G. Bryce, A. Dodson, D. L. Shuster and B. M. Kennedy (2001), Isotopic evolution of Mauna Loa and the chemical structure of the Hawaiian plume, *Geochemistry Geophysics Geosystems 2* doi:10.1029/2000GC000139

DePaolo, D. J. and E. M. Stolper (1996), Models of Hawaiian volcano growth and plume structure: Implications of results from the Hawaii Scientific Drilling Project, *Journal of Geophysical Research 101*, 11,1643-11,654

Dick, H., J. Lin and H. Schouten (2003), An ultraslow-spreading class of ocean ridge, *Nature 426*, 405-412 doi:10.1038/nature.02128

Douglass, J. and J.-G. Schilling (2000), Systematics of three-component, pseudo-binary mixing lines in 2D isotope ratio space representations and implications for mantle plume-ridge interaction, *Chemical Geology 163*, 1-23

Eisele, J., W. Abouchami, J. G. Galer and A. W. Hofmann (2003), The 320 kyr Pb isotope evolution of Mauna Kea lavas recorded in the HSDP-2 drill core, *Geochemistry Geophysics Geosystems 4* doi:10.1029/2002GC000339

Farnetani, C. and A. W. Hofmann (2009), Dynamics and internal structure of a lower mantle plume conduit, *Earth and Planetary Science Letters 282*, 314-422

Farnetani, C. G., B. Legras and P. J. Tackley (2002), Mixing deformations in mantle plumes, *Earth and Planetary Science Letters 196*, 1-15

Farnetani, C. G. and M. A. Richards (1995), Thermal entrainment and melting in mantle plumes, *Earth and Planetary Science Letters 136*, 251-267

Farnetani, C. G. and H. Samuel (2005), Beyond the thermal plume paradigm, *Geophysical Research Letters 32*, L07311 doi:10.1029/2005GL022360

Feigenson, M., L. L. Bogle, M. J. Carr and C. T. Herzberg (2003), REE inverse modeling of HSDP2 basalts: Evidence for multiple sources in the Hawaiian plume, *Geochemistry Geophysics Geosystems 4* doi:10.1029/2001GC000271

Feighner, M. A. and M. A. Richards (1995), The fluid dynamics of plume-ridge and plume-plate interactions: An experimental investigation, *Earth and Planetary Science Letters 129*, 171-182

Fitton, J. G., A. Saunders, M. Norry, B. S. Hardarson and R. N. Taylor (1997), Thermal and chemical structure of the Iceland plume, *Earth and Planetary Science Letters 153*, 197-208

Fitton, J. G., A. Saunders, P. D. Kempton and B. S. Hardarson (2003), Does depleted mantle form an intrinsic part of the Iceland plume?, *Geochem. Geophys. Geosys. 4* doi:10.1029/2002GC000424

Foulger, G. R., M. J. Pritchard, B. R. Julian, J. R. Evans, R. M. Allen, G. Nolet, W. J.

Morgan, B. H. Bergsson, P. Erlendsson, S. Jakobsdottir, S. Ragnarsson, R. Stefansson and K. Vogfjord (2000), The seismic anomaly beneath Iceland extends down to the mantle transition zone and no deeper, *Geophys. J. Int. 142*, 1-5

Frey, F. A. and J. M. Rhodes (1993), Intershield geochemical differences among Hawaiian volcanoes: Implications for source compositions, melting process and magma ascent paths, *Philosophical Transactions of the Royal Society of London A 342*, 121-136

Frey, F. A., W. S. Wise, M. O. Garcia, H. West, S.-T. Kwon and A. Kennedy (1990), Evolution of Mauna Kea volcano, Hawaii: Petrologic and geochemical constraints on postshield volcanism, *Journal of Geophysical Research 95*, 1271-1300

Fukao, Y., S. Widiyantoro and M. Obayashi (2001), Stagnant slabs in the upper and lower mantle transition region, *Reviews of Geophysics 39*, 291-323

Gallart, J., L. Driad, P. Charvis, M. Sapin, A. Hirn, J. Diaz, B. de Voogd and M. Sachpazi (1999), Perturbation to the lithosphere along the hotspot track of La Reunion from an offshore-onshore seismic transect, *Journal of Geophysical Research 104*, 2895-2908

Garcia, M. O., E. H. Haskins, E. M. Stolper and M. B. Baker (2007), Stratigraphy of the Hawaii Scientific Drilling Project core (HSDP2): Anatomy of a Hawaiian shield volcano, *Geochem. Geophys. Geosys. 8* doi:10.1029/2006GC001379

Geist, D. J., W. M. White and A. R. McBirney (1988), Plume-asthenosphere mixing beneath the Galapagos archipelago, *Nature 333*, 657-660 doi:10.1038/333657a0

Graham, D. W., D. M. Christi, K. S. Harpp and J. E. Lupton (1993), Mantle plume helium in submarine basalts from the Galapagos platform, *Science 262*, 2023-2026 doi:10.1126/science.262.5142.2023

Gripp, A. E. and R. G. Gordon (2002), Young tracks of hotspots and current plate velocities, *Geophys. J. Int. 150*, 321-361

Hanan, B. B., J. Blichert-Toft, R. H. Kingsley and J.-G. Schilling (2000), Depleted Iceland mantle plume geochemical signature: Artifact of multicomponent mixing?, *Geochem. Geophys. Geosys. 1* doi:10.1029/1999GC000009

Hanan, B. B. and D. W. Graham (1996), Lead and helium isotope evidence from oceanic basalts for a common deep source of mantle plumes, *Science 272*, 991-995

Hanan, B. B., R. Kingsley and J.-G. Schilling (1986), Pb isotope evidence in the South Atlantic for migrating ridge-hotspot interaction, *Nature 322*

Hanan, B. B. and J.-G. Schilling (1997), The dynamic evolution of the Iceland mantle plume: The lead isotope perspective, *Earth and Planetary Science Letters 151*, 43-60

Hards, V. L., P. D. Kempton and R. N. Thompson (1995), The heterogeneous Iceland plume-New insights from the alkaline basalts of the Snaefell volcanic center, *Journal of the Geological Society of London 152*, 1003-1009

Harpp, K. S. and W. M. White (2001), Tracing a mantle plume: Isotopic and trace element variations of Galapagos seamounts, *Geochemistry Geophysics Geosystems 2* doi:10.1029/2000GC000137

Hart, S. R., E. H. Hauri, L. A. Oschmann and J. A. Whitehead (1992), Mantle plumes and entrainment: Isotopic evidence, *Science 256*, 517-520

Hart, S. R., J.-G. Schilling and J. L. Powell (1973), Basalts from Iceland and along the

Reykjanes Ridge: Sr isotope geochemistry, *Nature Physical Sciences 246*, 104-107

Haskins, E. H. and M. O. Garcia (2004), Scientific drilling reveals geochemical heterogeneity within the Koolau shield, Hawaii, *Contributions to Mineralogy and Petrology 147*, 162-188

Hauri, E. H., J. A. Whitehead and S. R. Hart (1994), Fluid dynamic and geochemical aspects of entrainment in mantle plumes, *Journal of Geophysical Research 99*, 24,275-24,300

Hemond, C., N. T. Arndt, U. Lichtenstein, A. W. Hofmann, N. Oskarsson and Steinthorsson (1993), The heterogeneous Iceland plume: Nd-Sr-O isotopes and trace element constraints, *Journal of Geophysical Research 98*, 15,833-15,850

Hemond, C., M. Condomines, S. Fourcade, C. J. Allègre, N. Oskarsson and M. Javoy (1988), Thorium, strontium and oxygen isotope geochemistry in recent tholeiites from Iceland: Crustal influence on mantle-derived magmas, *Earth and Planetary Science Letters 87*, 273-285

Hess, H. H. (1962), History of ocean basins, *Petrologic Studies: A Volume to Honor A. F. Buddington*, A. E. J. Engel, H. L. James and B. F. Leonard, 599-620, Geological Society of America, New York.

Hirschmann, M., P. D. Asimow, M. S. Ghiorso and E. M. Stolper (1999), Calculation of peridotite partial melting from thermodynamic models of minerals and melts III. Controls on the isobaric melt production and the effect of water on melt production, *Journal of Petrology 40*, 831-851

Hirth, G. and D. L. Kohlstedt (1996), Water in the oceanic upper mantle: Implications for rheology, melt extraction and the evolution of the lithosphere, *Earth and Planetary Science Letters 144*, 93-108

Hirth, G. and D. L. Kohlstedt (2003), Rheology of the upper mantle and the mantle wedge: A view from the experimentalists, *Inside the subduction factory*, Geophysical Monograph 138, J. Eiler, 83-105, American Geophysical Union, Washington, D.C.

Hofmann, A. W. (1997), Mantle geochemistry: the message from oceanic volcanism, *Nature 385*, 219-229

Hooft, E. E., B. Brandsdottir, R. Mjelde, H. Shimamura and Y. Murai (2006), Asymmetric plume-ridge interaction around Iceland: The Kolbeinsey Ridge Iceland Seismic Experiment, *Geochem. Geophys. Geosys. 7* doi:10.1029/2005GC001123

Hung, S.-H., Y. Shen and L.-Y. Chiao (2004), Imaging seismic velocity structure beneath the Iceland hot spot: A finite frequency approach, *Journal of Geophysical Research 109*, 8305-8321

Ito, G., J. Lin and C. W. Gable (1996), Dynamics of mantle flow and melting at a ridge-centered hotspot: Iceland and the Mid-Atlantic Ridge, *Earth and Planetary Science Letters 144*, 53-74

Ito, G., J. Lin and D. Graham (2003), Observational and theoretical studies of the dynamics of mantle plume-mid-ocean ridge interaction, *Reviews of Geophysics 41*, 1017-10-41 doi:10.1029/2002RG000117

Ito, G. and J. J. Mahoney (2005a), Flow and melting of a heterogeneous mantle: 1.

Method and importance to the geochemistry of ocean island and mid-ocean ridge basalts *Earth and Planetary Science Letters 230*, 29-46 doi:10.1016/j.epsl.2004.10.035

Ito, G. and J. J. Mahoney (2005b), Flow and melting of a heterogeneous mantle: 2. Implications for a chemically nonlayered mantle, *Earth and Planetary Science Letters 230*, 47-63 doi:10.1016/j.epsl.2004.10.034

Ito, G. and J. J. Mahoney (2006), Melting a high $^{3}He/^{4}He$ source in a heterogeneous mantle, *Geochemistry Geophysics Geosystems 7* doi:10.1029/2005GC001158

Ito, G., Y. Shen, G. Hirth and C. Wolfe (1999), Mantle flow, melting and dehydration of the Iceland mantle plume, *Earth and Planetary Science Letters 165*, 81-96

Ito, G. and P. E. van Keken (2007), Hotspots and melting anomalies, *Treatise on Geophysics*, 7, D. Bercovici and G. Schubert, Elsevier.

Jackson, M., S. R. Hart, A. P. Koppers, H. Staudigel, J. Konter, J. Blutsztajn, M. D. Kurz and J. A. Russell (2007), The return of subducted continental crust in Samoan lavas, *Nature 448*, 684-687 doi:10.1038/nature06048

Johnson, K., H. Dick and N. Shimizu (1990), Melting in the oceanic upper mantle: An ion microprobe study of diopsides in abyssal peridotites, *Journal of Geophysical Research 95*, 2661-2678

Katz, R. F., M. Spiegelman and C. H. Langmuir (2003), A new parameterization of hydrous mantle melting, *Geochemistry Geophysics Geosystems 4* doi:10.1029/2002GC000433

Kempton, P. D., J. G. Fitton, A. Saunders, G. M. Nowell, R. N. Taylor, B. S. Hardarson and G. Pearson (2000), The Icelandic plume in space and time: a Sr-Nd-Pb-Hf study of the North Atlantic rifted margin, *Earth and Planetary Science Letters 177*, 255-271

Kennedy, A., S.-T. Kwon, F. A. Frey and H. West (1991), The isotopic composition of postshield lavas from Mauna Kea volcano, Hawaii, *Earth and Planetary Science Letters 103*, 339-353

Kerr, A. C. (1995), The melting processes and composition of the North Atlantic (Iceland) plume: Geochemical evidence from the early Tertiary basalts, *Journal of the Geological Society of London 152*, 975-978

Kerr, A. C., A. Saunders, J. Tarney, N. H. Berry and V. L. Hards (1995), Depleted mantle-plume geochemical signatures: No paradox for plume theories, *Geology 23*, 843-846

Klein, E. M. and C. H. Langmuir (1987), Global correlations of ocean ridge basalt chemistry with axial depth and crustal thickness, *Journal of Geophysical Research 92*, 8089-8115

Kokfelt, T. F., K. Hoernle, F. Hauff, J. Fiebig, R. Werner and D. Garbe-Schonberg (2006), Combined trace element and Pb-Nd-Sr-O isotope evidence for recycled oceanic crust (upper and lower) in the Iceland mantle plume, *Journal of Petrology 47*, 1705-1749 doi:10.1093/petrology/eg1025

Kurz, M. D., M. O. Garcia, F. A. Frey and P. A. O'Brien (1987), Temporal helium isotopic variations within Hawaiian volcanoes: Basalts from Mauna Loa and Haleakala, *Geochimica et Cosmochimica Acta 51*, 2905-2914

Kurz, M. D. and D. J. Geist (1999), Dynamics of the Galapagos hotspot from helium

isotope geochemistry, *Geochimica et Cosmochimica Acta 63*, 4139-4156
Kurz, M. D. and D. P. Kammer (1991), Isotopic evolution of Mauna Loa volcano, *Earth and Planetary Science Letters 103*, 257-269
Kurz, M. D., T. C. Kenna, J. C. Lassiter and D. J. DePaolo (1996), Helium isotopic evolution of Mauna Kea volcano: First results from the 1-km drill core, *Journal of Geophysical Research 101*, 11,781-11,791
Lai, W. M., D. Rubin and E. Krempl (1993). Introduction to Continuum Mechanics. Woburn, MA, Butterworth-Heinemann.
Langmuir, C. H., E. M. Klein and T. Plank (1992), Petrological systematics of mid-ocean ridge basalts: Constraints on melt generation beneath ocean ridges, *Mantle flow and melt generation at mid-ocean ridges*, Geophysical Monograph 71, J. Phipps Morgan, D. K. Blackman and J. M. Sinton, 183-280, American Geophysical Union, Washington D.C., USA
Lassiter, J. C., D. J. DePaolo and M. Tatsumoto (1996), Isotopic evolution of Mauna Kea volcano: Results from the initial phase of the Hawaii Scientific Drilling Project, *Journal of Geophysical Research 101*, 11,769-11,780
Lipman, P. W., T. W. Sisson, M. L. Coombs, A. Clavert and J.-I. Kimura (2006), Piggyback tectonics: Long-term growth of Kilauea on the south flank of Mauna Loa, *Journal of Volcanology and Geothermal Research 151*, 73-108 doi:10.1016/j.jvolgeores.2005.07.032
Luais, B. (2004), Temporal changes in Nd isotopic composition of Piton de la Fournaise magmatism (Reunion Island, Indian Ocean), *Geochem. Geophys. Geosys. 5* doi:10.1029/2002GC000502
Macdonald, G. A. and T. Katsura (1964), Chemical composition of Hawaiian Lavas, *Journal of Petrology 5*, 82-133
Marske, J. P., A. J. Pietruszka, D. Weis, M. O. Garcia and J. M. Rhodes (2007), Rapid passage of small-scale mantle heterogeneity through melting regions of Kilauea and Mauna Loa Volcanoes, *Earth and Planetary Science Letters 259*, 34-50 doi:10.1016/j.epsl.2007.04.026
McKenzie, D. (2000), Constraints on melt generation and transport from U-series activity ratios, *Chemical Geology 162*, 81-94
Menke, W. (1999), Crustal isostasy indicates anomalous densities beneath Iceland, *Geophys. Res. Lett. 26*, 1215-1218
Mertz, D. F., C. W. Devey, W. Todt, P. Stoffers and A. W. Hofmann (1991), Sr-Nd-Pb isotope evidence against plume-asthenosphere mixing north of Iceland, *Earth and Planetary Science Letters 107*, 243-255
Mertz, D. F. and K. M. Haase (1997), The radiogenic isotope composition of the high-latitude North Atlantic mantle, *Geology 25*, 411-414S
Michael, P. (1995), Regionally distinctive sources of depleted MORB: Evidence from trace elements and H_2O, *Earth and Planetary Science Letters 131*, 301-320
Moresi, L. and M. Gurnis (1996), Constraints on the lateral strength of slabs from three-dimensional dynamic flow models, *Earth and Planetary Science Letters 138*, 15-28
Morgan, W. J. (1971), Convection plumes in the lower mantle, *Nature 230*, 42-43
Morgan, W. J. (1972), Deep mantle convection plumes and plate motions, *The Am. Ass.*

Pet. Geol. Bull. 56, 203-213
Müller, R. D., W. R. Roest, J.-Y. Royer, L. M. Gahagan and J. G. Sclater (1997), Digital isochrons of the world's ocean floor, *Journal of Geophysical Research 102*, 3211-3214
O'Nions, R. K. and K. Gronvold (1973), Petrogenetic relationships of acid and basic rocks in Iceland: St-isotopes and rare-earth element in late and postglacial volcanics, *Earth and Planetary Science Letters 19*, 397-409
O'Nions, R. K. and R. J. Parkhurst (1973), Secular variation in the Sr-isotope composition of Icelandic volcanic rocks, *Earth and Planetary Science Letters 21*, 12-21
O'Nions, R. K., R. J. Parkhurst, I. B. Frdleifsson and P. Jakobsson (1973), Strontium isotopes and rare earth elements in basalts from Heimay and Surstey volcanic eruptions, *Nature 243*, 213-214
Pertermann, M. and M. Hirschmann (2003), Partial melting experiments on a MORB-like pyroxenite between 2 and 3 GPa: Constraints on the presence of pyroxenite in basalt regions from solidus location and melting rate, *Journal of Geophysical Research 108*, 2125-2142 doi:10.1029/2000JB000118
Phipps Morgan, J. (2001), Thermodynamics of pressure release melting of a veined plum pudding mantle, *Geochem. Geophys. Geosys. 2* doi:10.1029/2000GC000049
Regelous, M., A. W. Hofmann, W. Abouchami and J. G. Galer (2003), Geochemistry of lavas from the Emperor seamounts, and the geochemical evolution of Hawaiian magmatism from 85 to 42 Ma, *Journal of Petrology 44*, 113-140
Ren, Z.-Y., S. Ingle, E. Takahashi, N. Hirano and T. Hirata (2005), The chemical structure of the Hawaiian mantle plume, *Nature 436* doi:10.1038/nature03907
Ribe, N. M. and U. R. Christensen (1999), The dynamical origin of Hawaiian volcanism, *Earth and Planetary Science Letters 171*, 517-531
Ribe, N. M., U. R. Christensen and J. Theissing (1995), The dynamics of plume-ridge interaction, 1: Ridge-centered plumes, *Earth and Planetary Science Letters 134*, 155-168
Robinson, J. E. and B. W. Eakins (2006), Calculated volumes of individual shield volcanoes at the young end of the Hawaiian ridge, *Journal of Volcanology and Geothermal Research 151*, 309-317 doi:10.1016/j.jvolgeores.2005.07.033
Roden, M. F., T. W. Trull, S. R. Hart and F. A. Frey (1994), New He, Nd, Pb, and Sr isotopic constraints on the constitution of the Hawaiian plume; Results from Koolau Volcano, Oahu, Hawaii, USA, *Geochem. Geophys. Geosys. 58*, 1431-1440
Rubin, K. H., I. van der Zander, M. C. Smith and E. C. Bergmanis (2005), Minimum speed limit for ocean ridge magmatism from ^{210}Pb-^{226}Ra-^{230}Th disequilibria, *Nature 437*, 534-538 doi:10.1038/nature03993
Salters, V. J. M., J. Blichert-Toft, Z. Fekiacova, A. Sachi-Kocher and M. Bizmis (2006), Isotope and trace element evidence for depleted lithosphere in the source of enriched Koolau basalts, *Contributions to Mineralogy and Petrology 151*, 297-312 doi:10.1007/s00410-005-0059-y
Schilling, J.-G. (1973), Iceland mantle plume: Geochemical study of Reykjanes Ridge, *Nature 242*, 565-571 doi:10.1038/242565a0

Schilling, J.-G. (1991), Fluxes and excess temperature of mantle plumes inferred from their interaction with migrating mid-ocean ridges, *Nature 352*, 397-403

Schilling, J.-G., R. Kingsley, D. Fontignie, R. Poreda and S. Xue (1999), Dispersion of the Jan Mayen and Iceland mantle plumes in the Arctic: A He-Pb-Nd-Sr isotope tracers study of basalts from the Kolbeinsey, Mohns, and Knipovich ridges. , *Journal of Geophysical Research 104*, 10,543-10,569

Schilling, J.-G., R. Kingsley, B. B. Hanan and B. McCully (1992), Nd-Sr-Pb isotopic variation along the Gulf of Aden: Evidence for Afar mantle plume-continental lithosphere interaction, *Journal of Geophysical Research 97*, 10,927-10,966

Skovgaard, A. C., M. Storey, J. Baker, J. Blutsztajn and S. R. Hart (2001), Osmium-Oxygen isotopic evidence for a recycled and strongly depleted component in the Icelandic mantle plume, *Earth and Planetary Science Letters 194*, 259-275

Sleep, N. H. (1990), Hotspots and mantle plumes: Some phenomenology, *Journal of Geophysical Research 95*, 6175-6736

Sobolev, A. V., A. W. Hofmann, D. V. Kuzmin, G. M. Yaxley, N. T. Arndt, S.-L. Chung, L. V. Danyushevsky, T. Elliott, F. A. Frey, M. O. Garcia, A. A. Gurenko, V. S. Kamenetsky, A. C. Kerr, N. A. Krivolutskaya, V. V. Matvienkov, I. K. Nikogosian, A. Rocholl, I. A. Sigurdsson, N. M. Sushchevskaya and M. Teklay (2007), The amount of recycled crust in sources of mantle-derived melts, *Science 316*, 412-417 doi:10.1126/science.1138113

Stracke, A., A. Zindler, V. Salters, D. McKenzie, J. Blichert-Toft, F. Albarède and K. Gronvold (2003), Theistareykir revisited, *Geochem. Geophys. Geosys. 4* doi:10.1029/2001GC000201

Sun, S.-S. and W. F. McDonough (1989), Chemical and isotopic systematics of oceanic basalts: implications for mantle composition and processes, *Magmatism in the Ocean Basins*, 42, A. Saunders and M. Norry, Geological Society of London.

Sun, S.-S., M. Tatsumoto and J.-G. Schilling (1975), Mantle plume mixing along the Reykjanes Ridge axis: Lead isotope evidence, *Science 190*, 143-147

Tatsumoto, M. (1978), Isotopic composition of lead in oceanic basalt and its implication to mantle evolution, *Earth and Planetary Science Letters 38*, 63-87 doi:10.1016/0012-821X(78)90126-7

Thirlwall, M. F., M. A. M. Gee, R. N. Taylor and B. J. Murton (2004), Mantle components in Iceland and adjacent ridges investigated using double-spike Pb isotope ratios, *Geochimica et Cosmochimica Acta 68*, 361-386

Thirlwall, M. F., B. Upton and C. Jenkins (1994), Interaction between continental lithosphere and the Iceland plume-Sr-Nd-Pb isotope geochemistry of Tertiary basalts, NE Greenland, *Journal of Petrology 35*, 839-879

van der Hilst, R. D., S. Widiyantoro and E. R. Engdahl (1997), Evidence for deep mantle circulation from global tomography, *Nature 386*, 578-584

van Hunen, J., S. Zhong, N. M. Shapiro and M. H. Ritzwoller (2005), New evidence for dislocation creep from 3-D geodynamic modeling of the Pacific upper mantle structure, *Earth and Planetary Science Letters 238*, 146-155 doi:10.1016/j.epsl.2005.07.006

van Keken, P. E. and C. J. Ballentine (1998), Whole-mantle versus layered mantle convection and the role of a high-viscosity lower mantle in terrestrial volatile

evolution, *Earth and Planetary Science Letters 156*, 19-32
Vine, F. J. and D. H. Matthews (1963), Magnetic anomalies over oceanic ridges, *Nature 199*, 947-949
Vine, F. J. and J. T. Wilson (1965), Magnetic anomalies over a young oceanic ridge off Vancouver Island, *Science 150*, 485-489
Vogt, P. R. (1971), Asthenosphere motion recorded by the ocean floor south of Iceland, *Earth and Planetary Science Letters 13*, 153-160 doi:10.1016/0012-821X(71)90118-X
Weir, N., R. S. White, B. Brandsdottir, P. Einarsson, H. Shimamura and H. Shiobara (2001), Crustal structure of the northern Reykjanes Ridge and Reykjanes Peninsula, south-west Iceland, *Journal of Geophysical Research 106*, 6347-6368
Wessel, P. (1993), A reexamination of the flexural deformation beneath the Hawaiian Islands, *Journal of Geophysical Research 98*, 12,177-12,190
White, R. S., D. McKenzie and R. K. O'Nions (1992), Oceanic crustal thickness from seismic measurements and rare earth element inversions, *Journal of Geophysical Research 97*, 19,683-19,715
White, W. M., A. R. McBirney and R. A. Duncan (1993), Petrology and geochemistry of the Galapagos Islands: Portrait of a pathological mantle plume, *Journal of Geophysical Research 98*, 19,533-19,563
Wilson, J. T. (1963), A possible origin of the Hawaiian Islands, *Canadian Journal of Physics 41*, 863-870
Wolfe, C., I. T. Bjarnason, J. C. VanDecar and S. C. Solomon (1997), Seismic structure of the Iceland mantle plume, *Nature 385*
Wood, D. A., J.-L. Joron, M. Treuil, M. Norry and J. Tarney (1979), Elemental and Sr isotope variations in basic lavas from Iceland and the surrounding ocean floor: The nature of mantle source inhomogeneities, *Contrib. Mineral. Petrol. 70*, 319-329
Workman, R. K. and S. R. Hart (2005), Major and trace element composition of the depleted MORB mantle (DMM), *Earth and Planetary Science Letters 231*, 53-72
Workman, R. K., S. R. Hart, M. Jackson, M. Regelous, K. A. Farley, B. J., M. D. Kurz and H. Staudigel (2004), Recycled metasomatized lithosphere as the origin of the Enriched Mantle II (EM2) end-member: Evidence from the Samoan Volcanic Chain, *Geochem. Geophys. Geosys. 5* doi:10.1029/2003GC000623
Xu, G., F. A. Frey, D. A. Clague, J. Blichert-Toft, B. Cousens and M. Weisler (2007), Geochemical characteristics of West Molokai shield- and postshield-stage lavas: Constraints on Hawaiian plume models, *Geochem. Geophys. Geosys. 8* doi:10:.1029/2006GC001554
Zhong, S. and A. B. Watts (2002), Constraints on the dynamics of mantle plumes from uplift of the Hawaiian Islands, *Earth and Planetary Science Letters 203*, 105-116
Zhong, S., M. T. Zuber, L. Moresi and M. Gurnis (2000), Role of temperature-dependent viscosity and surface plates in spherical shell models of mantle convection, *Journal of Geophysical Research 105*, 11,063-11,082
Zindler, A. and S. R. Hart (1986), Chemical geodynamics, *Ann. Rev. Earth Planet. Sci. 14*, 493-571
Zindler, A., S. R. Hart, F. A. Frey and S. P. Jakobsson (1979), Nd and Sr isotope rations

and rare earth element abundances in Reykjanes Peninsula basalts: Evidence for mantle heterogeneity beneath Iceland, *Earth and Planetary Science Letters 45*, 249-262